



**ANALYSIS OF HYBRID-ELECTRIC PROPULSION SYSTEM DESIGNS FOR  
SMALL UNMANNED AIRCRAFT SYSTEMS**

THESIS

Ryan M. Hiserote, BSE  
Captain, USAF

AFIT/GAE/ENY/10-M11

**DEPARTMENT OF THE AIR FORCE  
AIR UNIVERSITY**

**AIR FORCE INSTITUTE OF TECHNOLOGY**

**Wright-Patterson Air Force Base, Ohio**

APPROVED FOR PUBLIC RELEASE; DISTRIBUTION UNLIMITED

The views expressed in this thesis are those of the author and do not reflect the official policy or position of the United States Air Force, Department of Defense, or the U.S. Government. This material is declared a work of the U.S. Government and is not subject to copyright protection in the United States.

AFIT/GAE/ENY/10-M11

**ANALYSIS OF HYBRID-ELECTRIC PROPULSION SYSTEM DESIGNS FOR  
SMALL UNMANNED AIRCRAFT SYSTEMS**

THESIS

Presented to the Faculty

Department of Aeronautics and Astronautics

Graduate School of Engineering and Management

Air Force Institute of Technology

Air University

Air Education and Training Command

In Partial Fulfillment of the Requirements for the  
Degree of Master of Science in Aeronautical Engineering

Ryan M. Hiserote, BSE

Captain, USAF

March 2010

APPROVED FOR PUBLIC RELEASE; DISTRIBUTION UNLIMITED

**ANALYSIS OF HYBRID-ELECTRIC PROPULSION SYSTEM DESIGNS FOR  
SMALL UNMANNED AIRCRAFT SYSTEMS**

Ryan M. Hiserote, BSE

Captain, USAF

Approved:

*Frederick G. Harmon*

Frederick G. Harmon, Lt Col, USAF (Chairman)

*12 Mar 10*

Date

*Christopher M. Shearer*

Christopher M. Shearer, Lt Col, USAF (Member)

*12 Mar 10*

Date

*Mark F. Reeder*

Dr. Mark F. Reeder (Member)

*12 Mar 10*

Date

## **Abstract**

Currently fielded electric-powered small unmanned aircraft systems (UAS) lack the endurance desired by warfighters, while their internal combustion engine (ICE) driven counterparts generate mission compromising acoustic and thermal signatures. Parallel hybrid-electric propulsion systems would meet the military's needs by combining the advantages of hydrocarbon and electric power systems. Three distinct parallel hybrid-electric system designs, each with three unique battery discharging profiles, were analyzed and compared using a constrained static optimization formulation based upon traditional aircraft design equations. Each system combined an ICE sized for cruise speed with an electric motor sized for endurance speed. The nine hybrid variations were compared using a typical five hour intelligence, surveillance and reconnaissance mission profile for a UAS with a maximum gross takeoff weight of 13.6 kg (30.0 lbf). A detailed analysis determined that the most suitable design for the baseline mission used a clutch-start configuration and a charge sustaining battery discharging strategy. The hybrid design enabled a 1.225 kg (2.701 lbf) payload capacity while providing fuel savings of 30.5% compared to a similarly sized, conventional ICE powered aircraft.

## **Acknowledgments**

Above all, I would like to thank God for blessing me with this tremendous opportunity by enabling me to pursue this degree while serving my country in the United States Air Force. After undergraduate school, I never would have imagined that I would be here today, but He knows the plans He has for me (Jeremiah 29:11). Without the patience and understanding of my beautiful wife, I would also not be where I am today. Her support deserves more thanks and recognition than words may offer. I must also thank my adviser Lt Col Fred Harmon for his patience in dealing with frequent unscheduled visits and countless questions. In fact, my thesis is based upon his hard work, original code and design for a hybrid-electric system. Finally, I have to thank Matt Rippl for his help during the summer quarter, especially for the part he played in developing alternatives to the original hybrid design.

-Ryan Hiserote

## Table of Contents

	Page
Abstract.....	iv
Acknowledgments.....	v
Table of Contents.....	vi
List of Figures.....	viii
List of Tables.....	xi
List of Abbreviations.....	xiii
Nomenclature.....	xv
I. Introduction.....	1
1. Background.....	1
2. Motivation.....	3
3. Problem Statement.....	5
4. Research Objective.....	6
5. Research Scope.....	7
6. Methodology.....	8
7. Thesis Overview.....	8
II. Literature Review.....	9
1. Chapter Overview.....	9
2. Hybrid-Electric Propulsion Background.....	9
2.1. Configurations.....	9
2.2. Applications.....	12
3. Hybrid System Components.....	17
3.1. Internal Combustion Engines.....	17
3.2. Electric Motors.....	22
3.3. Rechargeable Batteries.....	24
3.4. Propellers.....	25
III. Methodology.....	29
1. Chapter Overview.....	29

2.	Hybrid Configurations.....	29
3.	Battery Discharging Profiles .....	33
4.	Aircraft Design Process.....	34
5.	Fundamental Aerodynamics.....	35
6.	Optimization.....	37
IV.	Analysis and Results .....	43
1.	Chapter Overview .....	43
2.	Input Data.....	43
3.	Baseline Mission Results .....	51
3.1.	Optimization and Aircraft Conceptual Design Results .....	51
3.2.	Charge Depletion Strategy.....	53
3.3.	Charge Sustaining Strategy .....	62
3.4.	Charge Sustaining with Segmented ISR Loiter Strategy.....	70
3.5.	Notional Designs for Baseline Mission.....	79
4.	Sensitivity Analysis.....	85
5.	Advanced Mission Analysis.....	87
V.	Conclusions and Recommendations.....	91
1.	Conclusions of Research .....	91
2.	Recommendations for Future Research .....	94
	Appendix A: MATLAB Code Equations .....	98
	Appendix B: Sample Data .....	103
	Appendix C: MATLAB Code.....	106
	Bibliography .....	123
	Vita .....	129

## List of Figures

	Page
Figure 1: Typical series hybrid system .....	10
Figure 2: Typical parallel hybrid system .....	11
Figure 3: Typical power-split configuration .....	12
Figure 4: Flight Design hybrid propulsion system .....	13
Figure 5: Four-stroke operating cycle.....	18
Figure 6: Two-stroke operating cycle.....	19
Figure 7: Typical four-stroke engine performance map .....	20
Figure 8: Equivalent circuit for a DC electric motor .....	23
Figure 9: Efficiency for Graupner 10"x8" propeller.....	27
Figure 10: Well-matched and poorly-matched motor and propeller pairs.....	28
Figure 11: Clutch-start parallel hybrid-electric configuration.....	30
Figure 12: Electric-start parallel hybrid configuration .....	31
Figure 13: Centerline-thrust hybrid configuration.....	32
Figure 14: Centerline-thrust hybrid-electric UAS conceptual design.....	32
Figure 15: UAS hybrid-electric propulsion design process.....	35
Figure 16: Power required curve.....	53
Figure 17: Charge depletion, clutch-start aircraft component weight fractions .....	54
Figure 18: Charge depletion, clutch-start propulsion component weight fractions.....	55
Figure 19: Charge depletion, clutch-start mission segment fuel weight fractions.....	55
Figure 20: Charge depletion, electric-start aircraft component weight fractions .....	56
Figure 21: Charge depletion, electric-start propulsion component weight fractions.....	57

Figure 22: Charge depletion, electric-start mission segment fuel weight fractions.....	57
Figure 23: Charge depletion, centerline-thrust aircraft component weight fractions .....	58
Figure 24: Charge depletion, centerline-thrust propulsion component weight fractions.	59
Figure 25: Charge depletion, centerline-thrust mission segment fuel weight fractions ..	59
Figure 26: Charge depletion aircraft component weight fraction comparison .....	61
Figure 27: Charge depletion propulsion component weight fraction comparison.....	61
Figure 28: Charge sustaining, clutch-start aircraft component weight fractions .....	63
Figure 29: Charge sustaining, clutch-start propulsion component weight fractions .....	63
Figure 30: Charge sustaining, clutch-start mission segment fuel weight fractions .....	64
Figure 31: Charge sustaining, electric-start aircraft component weight fractions .....	65
Figure 32: Charge sustaining, electric-start propulsion component weight fractions .....	65
Figure 33: Charge sustaining, electric-start mission segment fuel weight fractions .....	66
Figure 34: Charge sustaining, centerline-thrust aircraft component weight fractions.....	67
Figure 35: Charge sustaining, centerline-thrust propulsion component weight fractions	67
Figure 36: Charge sustaining, centerline-thrust mission segment fuel weight fractions .	68
Figure 37: Charge sustaining aircraft component weight fraction comparison.....	69
Figure 38: Charge sustaining propulsion component weight fraction comparison .....	70
Figure 39: Segmented loiter, clutch-start aircraft component weight fraction .....	72
Figure 40: Segmented loiter, clutch-start propulsion component weight fractions.....	72
Figure 41: Segmented loiter, clutch-start mission segment fuel weight fraction .....	73
Figure 42: Segmented loiter, electric-start aircraft component weight fractions.....	74
Figure 43: Segmented loiter, electric-start propulsion component weight fractions .....	74

Figure 44: Segmented loiter, electric-start mission segment fuel weight fractions .....	75
Figure 45: Segmented loiter, centerline-thrust aircraft component weight fractions .....	76
Figure 46: Segmented loiter, centerline-thrust propulsion component weight fractions.	76
Figure 47: Segmented loiter, centerline-thrust mission segment fuel weight fractions...	77
Figure 48: Segmented loiter aircraft component weight fraction comparison .....	78
Figure 49: Segmented loiter propulsion component weight fraction comparison.....	79

## List of Tables

Table 1: Comparison of common rechargeable batteries .....	25
Table 2: Baseline mission requirements .....	45
Table 3: Aircraft design parameters.....	46
Table 4: Propulsion component specifications .....	48
Table 5: Propeller efficiencies .....	50
Table 6: Optimization variable bounds.....	51
Table 7: Optimization and aircraft conceptual design results.....	52
Table 8: Power required results .....	53
Table 9: Propulsion system component specifications .....	60
Table 10: Propulsion system component specifications .....	69
Table 11: Propulsion system component specifications .....	78
Table 12: Loiter charging statistics.....	78
Table 13: Notional COTS components for charge depletion strategy.....	81
Table 14: Notional charge depletion, centerline-thrust component specifications.....	81
Table 15: Notional COTS components for charge sustaining strategy.....	82
Table 16: Notional charge sustaining, clutch-start component specifications.....	83
Table 17: Notional COTS components for segmented loiter strategy.....	84
Table 18: Notional segmented loiter, electric-start component specifications .....	84
Table 19: Payload mass sensitivity analysis .....	87
Table 20: Proposed segmented ISR mission profile .....	90
Table 21: Recommended mission summary .....	92

Table B-1: Market survey results for similar aircraft .....	103
Table B-2: Commercially available internal combustion engine data.....	103
Table B-3: Commercially available brushless electric motor data .....	104
Table B-4: Sample QPROP results .....	105

## List of Abbreviations

ACC	Air Combat Command
AFIT	Air Force Institute of Technology
AFRL	Air Force Research Laboratory
AFSOC	Air Force Special Operations Command
AGL	Above Ground Level
ATO	Air Tasking Order
AVL	Athena Vortex Lattice
COTS	Commercial Off-the-Shelf
DC	Direct Current
DoD	Department of Defense
EAA	Experimental Aircraft Association
EM	Electric Motor
ERAST	Environmental Research Aircraft and Sensor Technology
FAA	Federal Aviation Administration
GWOT	Global War on Terrorism
HALE	High Altitude Long Endurance
HEUAS	Hybrid-Electric Unmanned Aircraft System
JIEDDO	Joint Improvised Explosive Device Defeat Organization
ICE	Internal Combustion Engine
IED	Improvised Explosive Device
IR	Infrared
ISR	Intelligence, Surveillance, and Reconnaissance
Li-Ion	Lithium-Ion
Li-Po	Lithium-Polymer
Li-S	Lithium-Sulfur
MATLAB	Matrix Laboratory
MEP	Mean Effective Pressure
MSL	Mean Sea Level
NACA	National Advisory Committee for Aeronautics

NASA	National Aeronautics and Space Administration
NATO	North Atlantic Treaty Organization
Ni-Cd	Nickel Cadmium
NiMH	Nickel Metal Hydride
NOAA	National Oceanic and Atmospheric Administration
OSD	Office of the Secretary of Defense
R/C	Radio Control
RPM	Rotations per Minute
SAM	Surface-to-Air Missile
SFC	Specific Fuel Consumption
SI	International System of Units
T/O	Takeoff
UAS	Unmanned Aircraft System
US	United States
USAF	United States Air Force
USN	United States Navy

## Nomenclature

<u>Symbol</u>	<u>Description (Units)</u>
$A$	Area ( $\text{m}^2$ )
$AR$	Aspect ratio
$C$	Capacity (Wh)
$C$	Specific capacity (mAh/g)
$C_D$	Coefficient of drag
$C_L$	Coefficient of lift
$C_P$	Coefficient of power
$C_T$	Coefficient of thrust
$D$	Drag force (N)
$e$	Oswald span efficiency factor
$E_e$	Specific energy (Wh/kg)
$F$	Force (N)
$F/A$	Fuel-to-air ratio
$h$	Altitude (m)
$h_e$	Energy height (m)
$i$	Current (A)
$J$	Advance ratio
$J$	Static optimization cost function
$K$	Drag polar proportionality constant
$K_V$	Electric motor speed constant (rad/s/V)
$K_Q$	Electric motor torque constant (A/Nm)
$L$	Lift force (N)
$m$	Mass (kg)
$m$	Number of inequality constraints
$\dot{m}$	Mass flow rate (kg/s)
$MEP$	Mean effective pressure ( $\text{N/m}^2$ )
$n$	Number of variables
$n_R$	Number of crank revolutions per power stroke

$N$	Crankshaft rotational speed (rad/s)
$p$	Number of equality constraints
$P$	Power (W)
$q$	Dynamic pressure (N/m <sup>2</sup> )
$Q$	Sensitivity parameter
$Q_{HV}$	Heating value (J/kg)
$Q_{LHV}$	Lower heating value (J/kg)
$Q_m$	Electric motor shaft torque (Nm)
$r$	Range (m)
$R$	Resistance ( $\Omega$ )
$S$	Wing planform area (m <sup>2</sup> )
$SFC$	Specific fuel consumption (kg/Wh)
$t$	Time (s)
$T$	Temperature (K)
$T$	Thrust (N)
$T$	Torque (Nm)
$W$	Weight (N)
$W_x$	Weight fraction
$W/S$	Wing loading (N/m <sup>2</sup> )
$v$	Voltage (V)
$V$	Volume (m <sup>3</sup> )
$\eta_{EM}$	Electric motor efficiency
$\eta_f$	Fuel conversion efficiency
$\eta_{gen}$	Electric motor efficiency
$\eta_{mech}$	Mechanical efficiency
$\eta_{prop}$	Propeller efficiency
$\eta_v$	Volumetric efficiency
$\rho$	Density (kg/m <sup>3</sup> )
$\Omega$	Angular velocity (rad/s)

<u>Subscript</u>	<u>Description</u>
<i>0</i>	Zero lift, Initial/Takeoff
<i>a</i>	Ambient
<i>A</i>	Available
<i>act</i>	Actual
<i>batt</i>	Battery
<i>d</i>	Displacement
<i>EM</i>	Electric motor
<i>end</i>	Endurance
<i>f</i>	Fuel
<i>fcs</i>	Flight control system
<i>gen</i>	Generator
<i>i</i>	Initial
<i>ICE</i>	Internal combustion engine
<i>m</i>	Motor
<i>max</i>	Maximum
<i>o</i>	No load
<i>R</i>	Required
<i>ref</i>	Reference
<i>w</i>	Windmill
$\infty$	Freestream

# ANALYSIS OF HYBRID-ELECTRIC PROPULSION SYSTEM DESIGNS FOR SMALL UNMANNED AIRCRAFT SYSTEMS

## I. Introduction

### 1. Background

Unmanned aviation emerged in the nineteenth century as aviation pioneers modeled their ideas for a practical means of manned flight.<sup>1</sup> The first viable unmanned aircraft, including Charles Kettering's Liberty Eagle Aerial torpedo, were possible following the development of the first inertial guidance systems in 1909.<sup>2</sup> However, the primitive guidance technology continued to hamper unmanned aviation's effectiveness for several more decades. In the latter stages of World War II, radar guidance systems provided primitive attack drones a more capable means of navigation, but still did not provide the results sought by the military. In the mid 1950s during the Cold War, the United States (US) Army showed an interest in using unmanned aircraft for surveillance. After a successful test flight by the SD-1 drone, the US military finally witnessed the tremendous potential of unmanned aviation.<sup>1,2</sup>

Over the next 50 years, the use of unmanned aircraft would rise exponentially. The Vietnam Conflict saw the first widespread use of unmanned aircraft, which were used for surveillance and surface-to-air missile (SAM) detection. During Operations Desert Shield and Desert Storm, the Iraqi army learned to fear the sound of the small-unmanned aircraft as it preceded devastating attacks by the US Air Force (USAF) and Navy (USN).<sup>2</sup> Other US government agencies such as the Department of Homeland Security and the National Oceanic and Atmospheric Administration (NOAA) followed

suit with their own platforms. Even the civilian sector has adopted unmanned aircraft for precision agriculture, commercial fishing and surveillance for urban traffic and wildfires.

In the past several years, the advanced military capabilities afforded by Unmanned Aircraft Systems (UAS) have created a further explosion in their employment. Daily UAS combat air patrol missions have increased from 21 in 2007 to about 36 in 2009 with a goal of 54 by 2011.<sup>3</sup> The Air Force's most heavily used UAS, the MQ-1 Predator, reached 250,000 flight hours in June 2007 after 12 years of flying. Just over two years later in September 2009, the aircraft had already exceeded 600,000 hours.<sup>4</sup> Unmanned aircraft have rapidly become mission critical to current Global War on Terrorism (GWOT) operations in Iraq and Afghanistan.

Today's combatant commanders have an insatiable appetite for persistent intelligence, surveillance and reconnaissance (ISR) provided by UAS. In a recent survey, all levels of military command listed reconnaissance as the number one priority for all classes of unmanned systems.<sup>5</sup> Additionally, the 2006 Quadrennial Defense Review emphasized persistent surveillance as a key mission need. As UAS capabilities develop, combatant commanders are broadening the scope of their application.

The intrinsic characteristics of UAS are unmatched by their manned counterparts. "The attributes of persistence, efficiency, flexibility of mission, information collection and attack capability have repeatedly proven to be force multipliers across the spectrum of global Joint military operations."<sup>6</sup> In the asymmetric warfare of GWOT, the abilities of UAS have proven to be mission essential. The Air Force is currently posturing itself to develop and harness unmanned system capabilities to maximize current and future contributions to the Joint Force.

## **2. Motivation**

Since the fall of Saddam Hussein's regime in May 2003, the primary threat to the United States military has been the improvised explosive device (IED). As the nightly news and morning papers continually remind, the weapon dominates fighting in both the Iraq and Afghanistan theaters. While the Taliban and al Qaeda still fight with small arms, IEDs are clearly their weapon of choice. Over the past six years, US forces have become increasingly more adept at locating and destroying IEDs, but in recent months the Taliban in particular have been building simpler bombs from hard-to-detect nonmetallic materials.<sup>7</sup> Consequently, US forces need a better method of locating the insidious low-tech devices.

In February 2006, Department of Defense (DoD) Directive 2000.19E permanently established the Joint Improvised Explosive Device Defeat Organization (JIEDDO) to lead "all Department of Defense actions in support of Combatant Commanders and their respective Joint Task Forces efforts to defeat improvised explosive devices as weapons of strategic influence".<sup>8</sup> JIEDDO funds and develops the critical tools needed for counter IED operations. Several key JIEDDO programs provide warfighters increased situational awareness through persistent tactical ISR capabilities for counter IED operations.

Unmanned aircraft systems are daily becoming a more significant component of the counter IED effort and other ISR-related missions as they take over flying the "dull, dirty and dangerous" missions from human pilots.<sup>10</sup> According to US Army Lieutenant General Rick Lynch, there are immediate applications for unmanned vehicles for route clearance and surveillance. He added that, "We're going to be fighting this war on terror for the next 10 years and the enemy's weapon of choice is the IED. It is today and it will

be in the future.”<sup>9</sup> Unmanned systems can monitor IED hotspots for extended periods to detect insurgent activity or locate the IEDs themselves. Without the persistent stare capability afforded by UAS, our nation’s warfighters would be even more susceptible to IED attacks.

Small UAS are poised to provide a solution to the IED problem while bringing unique capabilities to all ISR missions. During peacetime, the majority of ISR missions use “stand-off” techniques to satisfy political sensitivities and mitigate risk of exposing high value platforms. The long endurance manned aircraft designed for these missions are limited in their ability to measure weak signals and record very high-resolution images. Small UAS could be deployed at much closer ranges for greater success in these areas. During “overflight” missions, small UAS are able to fly much lower than their manned counterparts to see “under the weather.” Finally, dangerous “denied access” missions are best suited to UAS. Manned aircraft, like the U-2, have a huge disadvantage due to high potential for aircrew loss and associated diplomatic tensions resulting from capture. Small stealthy UAS can provide “denied access” ISR with a low risk of detection. Both the 2003 Defense Science Board and the Air Force Scientific Advisory Boards observed that the DoD needs a UAS capable of unwarned collection.<sup>10</sup> “Being able to surveil hostile areas while maintaining a degree of covertness is highly desirable.”<sup>5</sup> The inherent risks of all three ISR mission categories lead towards small UAS being the best option in many cases to meet the military’s needs.

In order to fulfill the aforementioned ISR missions, an aircraft must be designed for both endurance and stealth. The practice of aircraft design can be a delicate balance between mission requirements. Building a small stealthy aircraft capable of long

endurance is counter to natural aerodynamic tendencies. To provide long endurance, an aircraft must possess a highly efficient aerodynamic shape and propulsion system. However, as the Reynolds number declines and the size of airfoils and power plants decrease, aerodynamic and thermodynamic efficiencies also drop. Combining this fact with the intricacies of stealth design leads to a highly complex optimization problem. Stealth attributes are easily achieved by reducing aircraft size, acoustic signatures and infrared (IR) signatures. The latter two can be accomplished with electric propulsion systems. Electric propulsion has many advantages, but brings an immense weight and endurance penalty to an aircraft due to the relatively poor specific energy of batteries. By combining the endurance capabilities of engine propulsion with the stealthy capabilities of electric power, a small, optimized UAS could meet the ISR mission objectives set forth by the DoD.

### **3. Problem Statement**

Unmanned aircraft have proven to be highly effective for traditional ISR and counter IED surveillance missions. However, currently fielded aircraft lack the endurance and/or the stealth attributes desired by warfighters. According to the *Unmanned Aircraft Systems Roadmap (2005-2030)*, the DoD must invest in improved propulsive efficiency through alternative propulsion power sources for endurance and unwarned ISR.<sup>10</sup> Internal combustion engine (ICE) driven aircraft possess adequate endurance for most ISR missions, but are loud enough to alert those being monitored. Electric propulsion systems are nearly silent and lack the strong thermal signatures associated with combustion. However, electric systems suffer from dismal endurance

times due to relatively low energy densities of current battery technology. Each system possesses desired mission attributes, but neither can meet the end goal.

At the dawn of the jet age, piston power supplemented turbine power just to get an aircraft off the ground. The cutting-edge jet engine designs could not meet the entire spectrum of the day's aircraft propulsion needs. Today, the same is true of electric power; battery power alone cannot fulfill an aircraft's power demands.<sup>11</sup> Hybrid-electric propulsion provides a promising solution to that problem. Theoretically, a hybrid-electric propulsion system could both decrease the fuel consumption and reduce the noise signature of an aircraft, as has been demonstrated in the automotive industry. By combining the advantages of carbon-based power and an electric power source, an advanced propulsion system could provide the endurance required for the counter IED mission, while possessing a potentially game-changing, near-silent covert capability.

The *Unmanned Systems Roadmap (2007-2032)* suggests that ISR missions with high endurance requirements “will require more sophisticated energy systems, such as fuel cells and hybrid systems.”<sup>5</sup> Additionally, the DoD is seeking to “develop and field reliable propulsion alternatives to gasoline-powered internal combustion engines” and “develop common, high-energy-density power sources... for unmanned systems that meet their challenging size, weight, and space requirements.”<sup>5</sup> These goals are met through hybrid-electric propulsion, by combining the high-energy-density power of hydrocarbon fuels with the reliability of electric power.

#### **4. Research Objective**

This research focused on three variations of a parallel hybrid-electric propulsion system design for a small UAS. Three distinct battery discharge strategies were proposed

for each hybrid configuration for a total of nine unique designs. The author developed a threefold objective to analyze that set of propulsion system designs. The initial goal was to validate and expand an existing UAS hybrid-electric propulsion system design code. Then using the updated design code, the nine unique hybrid-electric system designs would be optimized and compared to determine the most suitable design for a typical ISR mission. The author hypothesized that each of the designs possesses unique advantages that should be tailored to specific missions. The final objective of the effort was to determine which types of missions would be best suited for each design.

## **5. Research Scope**

The conceptual designs created by this effort are the result of a static optimization algorithm to size the components for various hybrid-electric propulsion system designs. In reality, aircraft design is a highly complex, multidisciplinary effort. Without a predetermined aircraft design, the effort assumed typical aerodynamic characteristics for similarly sized aircraft. In sizing the propulsive components, the aircraft's structural requirements such as strength, shape and volume were ignored. The design code assumed a traditional wing cross section with a rectangular planform area for certain calculations. Additionally, flight dynamics and control issues are not analyzed. The results of the process could be used as the basis for a new UAS design. The effort specifically focused on small UAS, but the underlying theory could be applied to larger systems.

## **6. Methodology**

The author implemented traditional aircraft performance and design equations in a constrained static optimization formulation to construct each hybrid-electric propulsion system design. By setting the endurance power as the cost function and allowing the design components to vary, the author was able to compare the effect of the hybrid propulsion design on the design of a “rubber” aircraft. The aircraft size was restricted to the Group 2 (small) UAS category as defined by the *United States Air Force UAS Flight Plan (2009-2047)*.<sup>6</sup> The UAS will be limited to maximum gross weight takeoff of 21-55 lbf and a normal operating altitude below 3,500 feet AGL. The category appropriately defines the aforementioned small UAS mission required by the US military.

## **7. Thesis Overview**

Chapter II of this thesis will review applicable theory from seminal and contemporary literature. Chapter III discusses specific propulsion system designs and optimization algorithms developed by this author. Chapter IV provides analysis and results of all testing performed throughout the research. Chapter V discusses the results and communicates conclusions and recommendations for future research.

## **II. Literature Review**

### **1. Chapter Overview**

Significant research and development by the automotive industry has led to hybrid propulsion technology, which drastically reduces fuel consumption and harmful emissions. The aviation community has begun to leverage the technology to capitalize on potential fuel savings and improved endurance. Military unmanned aircraft systems, in particular, could benefit from additional benefits of hybrid technology such as reduced acoustic and infrared signatures. However, significant research must be performed to optimize the technology for specific aircraft missions in order to benefit from the technology's inherent capabilities. This chapter begins by briefly outlining the background of hybrid-electric propulsion through its various configurations and current applications. The author will then analyze each component within a proposed set of hybrid configurations.

### **2. Hybrid-Electric Propulsion Background**

#### **2.1. Configurations**

Hybrid technology combines the advantages of two or more power sources to create a more efficient propulsion system for a vehicle. While many variants of hybrid systems are available today, most derive from three basic categories: series, parallel and power-split. While most systems utilize an internal combustion engine as the primary power source, others use fuel cells or turbine engines. Each system has unique advantages and disadvantages adaptable to the specific needs of a vehicle.

In a series hybrid configuration, the primary propulsion source is an electric motor (EM). Typically, an internal combustion engine drives a generator, which then provides power to the motor and an energy storage system. Because the ICE is not mechanically linked to the driveshaft, it is able to operate at its optimum torque and speed range independent of power demand. As seen in Fig. 1, excess energy from the generator may be stored in a battery, capacitor or flywheel for high demand operation.<sup>12</sup> While the system provides a higher wells-to-wheels efficiency than a conventional ICE propulsion system, the vehicle suffers from a lower mechanical efficiency and a large weight penalty since the motor must be sized for maximum power output. For the series configuration to be viable, the system must possess a high overall power efficiency to compensate for the relatively high weight. Accordingly, large vehicles, like buses and locomotives, are the most common use for the configuration.<sup>13</sup>

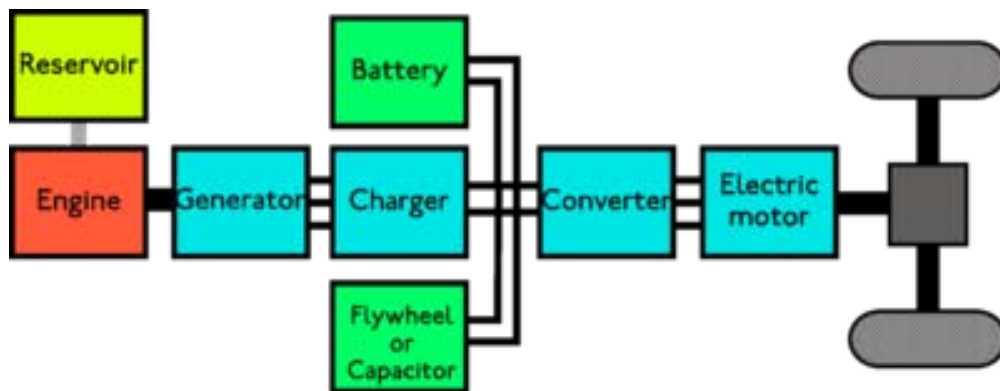


**Figure 1: Typical series hybrid system**

A parallel hybrid system combines two or more power sources through a mechanical linkage to provide power to a single shaft, as shown in Fig. 2.<sup>14</sup> Unlike its series counterpart, the parallel configuration allows the ICE and the EM to individually or jointly power a vehicle through a clutch. Parallel configurations are classified further

into mild, power assist and dual mode configurations. Mild parallel systems utilize a small EM to provide extra power during acceleration and recharge during deceleration through regenerative braking. Power assist systems are similar to mild systems, but use a larger EM for a higher degree of hybridization. The larger motor and associated battery pack enable a short duration of electric-only operation not possible with a mild system. Dual mode systems incorporate electric drive components having power fractions of greater than 30% of the total system power. The larger electric drive system enables an extended electric-only range as high as 60 miles on some automobiles.<sup>13</sup> The dual mode system has the greatest efficiency of the parallel configurations at the expense of system cost and complexity.

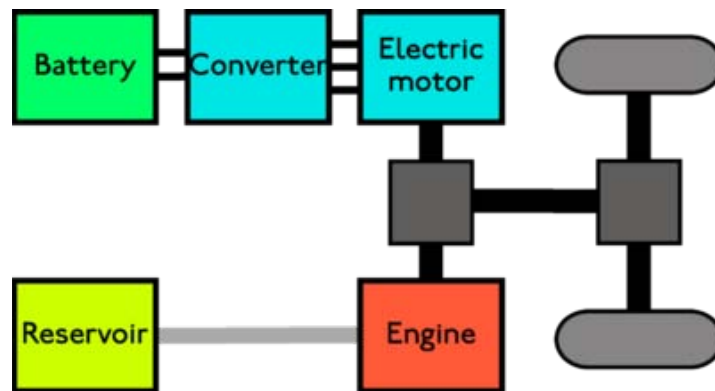


**Figure 2: Typical parallel hybrid system**

The third hybrid type is a combination of the former two. The power-split (or series-parallel) configuration lacks a driveline clutch, but uses a system of planetary (epicyclic) gears to transfer power from the ICE and the EM to the wheels, as shown in Fig. 3.<sup>15</sup> The engine delivers torque to the wheels for propulsion after splitting a portion to a generator for conversion to electricity. The electric power recombines with engine mechanical power at the planetary gear.<sup>12</sup> Since the ICE power and speed are decoupled

from the overall propulsive demand, the engine is able to run at or near optimal conditions. Many power-split applications can therefore use the more efficient Atkinson cycle rather than the more common, power dense Otto cycle engine. A controller ensures that the ICE operates within its efficiency island when needed for charging or propulsion. The power-split system weighs more than the parallel version and requires the most complex controller, but provides the most efficient hybrid platform.

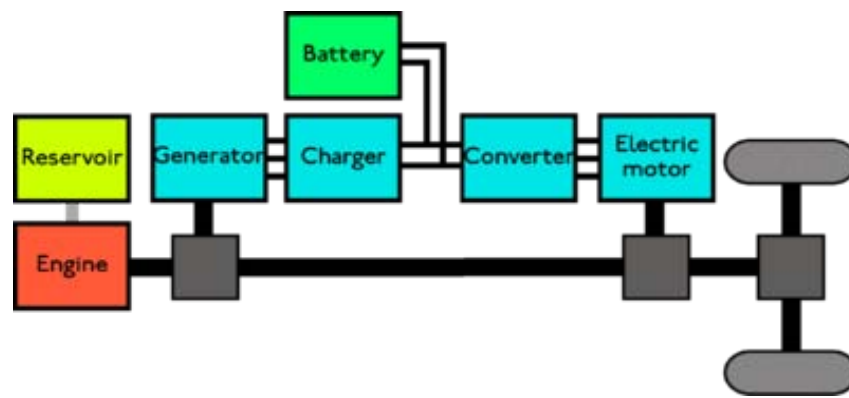


Figure 3: Typical power-split configuration

## 2.2. Applications

The automotive industry has clearly led the charge for hybrid propulsion technology. In late 1999, Honda introduced the United States to its first production gasoline-electric hybrid car, the *Insight*.<sup>16</sup> The *Insight* featured Honda's *Integrated Motor Assist* technology, which combined an EM with an ICE in a mild parallel configuration. Since the arrival of the *Insight*, nearly every major automotive manufacturer has released its own hybrid model. The Toyota *Prius*, released to the US in 2001, has dominated the hybrid marketplace with US sales topping 1,000,000 in March 2009.<sup>17</sup> The *Prius* features a power-split hybrid system enabling use of an Atkinson cycle gasoline engine and electric-only operation, unlike the *Insight*. While today's ICE

powered hybrids provide a substantial increase in fuel economy, the end goal of the auto industry is a fleet powered by fuel cells to improve overall efficiency and virtually eliminate environmentally harmful emissions.

While automotive hybrid-electric technology is rapidly maturing, the aircraft industry has begun to tap into its capabilities. At the 2009 EAA AirVenture Oshkosh, German aircraft builder Flight Design displayed a one-of-a-kind hybrid-electric motor for a light-sport aircraft. A battery-powered 40 hp electric motor provides approximately five minutes of boost power to a 115 hp Rotax 914 engine for takeoff and climbing (Fig. 4).<sup>18</sup> Like automotive hybrids, the aircraft utilizes a form of regenerative braking by charging its battery pack through propeller wind-milling as the aircraft descends. The hybrid system allowed the manufacturer to down-size the engine from a 160 hp model to a more efficient 115 hp engine.<sup>18</sup> This power-assist parallel hybrid configuration also allows the pilot to stretch a glide with electric power in the event of engine failure. While there are limited applications for hybridized manned aviation, the demand for persistent ISR has created tremendous opportunity for hybrid technology in unmanned aviation.



**Figure 4: Flight Design hybrid propulsion system**

Prominent aircraft and engine developers are currently pursuing a variety of radical hybrid designs. AeroVironment is combining a hydrogen-burning piston engine with an electric drive system to turn eight propellers on its high altitude long endurance (HALE) *Global Observer*, which is scheduled to fly in early 2010.<sup>11</sup> Aurora Flight Sciences is developing a concept that utilizes a small turbo-diesel engine with an electric generator between the exhaust-driven turbine and compressor in the turbocharger, allowing the turbine and compressor to run at different speeds. The concept would simplify designing small diesel engines, which are highly desired by the Pentagon and military logisticians.<sup>19</sup> Engine giant Rolls-Royce is exploring combinations of their proven turbine engines with various electric drive components for both HALE and Unmanned Combat Aerial Vehicle (UCAV) applications.<sup>20</sup> Startup company Bye Aerospace has a different approach for its HALE UAS. Bye's *Silent Sentinel* will use a turbofan for primary propulsion and use thin-film solar arrays and lithium-ion batteries to provide multi-day endurance loitering.<sup>11</sup> Each design pushes aviation propulsion technology, once dominated by hydrocarbon fueled rotating engines, towards a greater degree of electrification or hybridization.

As the technology advances, the aircraft industry is also leaning more towards utilizing fuel cells as a viable means of propulsion and eliminating the need for hydrocarbon fuels. Fuel cells can provide much higher propulsive efficiencies than internal combustion engines with negligible acoustic and infrared signatures and without harmful emissions. However, fuel cells lack the specific energy of ICEs, which greatly hampers their effectiveness for aviation propulsion. Great improvements have been made in recent years leading to pioneering efforts by the industry.

Perhaps the most promising adaptation is AeroVironment's *Puma*. Under a small business innovation research (SBIR) contract with AFRL, the battery-only *Puma* was modified with a fuel cell hybrid energy storage system, tripling its flight endurance time from three to nine hours.<sup>21</sup> The increased performance could expand the variety of missions that the *Puma* can perform. In April 2008, Boeing demonstrated straight and level manned flight using a hybrid system comprised of a fuel cell and lithium-ion batteries on a modified Diamond Aircraft *Dimona* motor glider.<sup>22</sup> While Boeing will not pursue the technology for manned applications, the defense industry giant intends to apply the collected data toward unmanned aircraft. In July 2009, the experimental *Antares DLR-H2* became the world's first manned vehicle to take-off under fuel cell power.<sup>23</sup> The *Helios Prototype*, developed under NASA's Environmental Research Aircraft and Sensor Technology (ERAST) project, demonstrated world record altitudes for a HALE UAS in 2001 with a hybrid system of solar cells and batteries. NASA plans to replace the batteries with a fuel cell to reduce weight and improve performance for the production vehicles.<sup>24</sup>

Fuel cell hybrid aircraft have shown promising results, but researchers at the Georgia Institute of Technology argue that hybridizing fuel cells with batteries may not always be advantageous.<sup>25</sup> The research team demonstrated that an optimized fuel cell alone would provide greater endurance than a fuel cell-battery combination in which the battery's state of charge was maintained. By instead allowing the battery to charge deplete and provide surge power when needed, the system may improve the overall performance of a hybridized fuel cell aircraft over a fuel cell only aircraft. Decoupling the fuel cell from more power demanding maneuvers like climbing enables the fuel cell

to be sized for the cruising power required. The smaller power requirement could significantly improve the overall endurance of an aircraft.

Various organizations have demonstrated non-hybridized fuel cell-driven UAS. In August 2006, Georgia Tech flew the largest (22 ft wingspan) UAS to fly on a proton exchange membrane (PEM) fuel cell.<sup>26</sup> The USN *Ion Tiger* uses a 500 W polymer fuel cell to fly nearly 24 hours.<sup>27</sup> Many other ICE powered UAS have been retrofitted and tested with fuel cells such as Insitu's *ScanEagle*. As fuel cell systems increase in specific energy, their practicable application to aircraft will expand.

The remainder of this paper will focus on internal combustion engine driven parallel hybrid-electric systems and will closely follow the conceptual design and simulation process for a small UAS developed by Harmon, et al, at the University of California-Davis.<sup>28</sup> This author's goal is to design a hybrid system with commercial-off-the-shelf (COTS) products that are readily available and supportable in the US military theater of operations. Fuel cells are possibly the way of the future; however, in current operations diesel fuel and gasoline are much more accessible than fuel cell reactants such as hydrogen and oxygen. Other researchers at AFIT are developing conceptual design tools for fuel cell-based systems.<sup>29</sup> Research by Harmats and Weihs concluded that series configurations were not effective for UAS due to large power losses.<sup>30</sup> Therefore, series hybrid configurations were not examined within the framework of this study due to their large associated weight penalties. Parallel and power-split configurations require much more complex controllers, but are more suitable to small aircraft.

### 3. Hybrid System Components

The proposed parallel hybrid-electric propulsion systems consist of an internal combustion engine, an electric motor, a rechargeable battery pack and a propeller. Various combinations of the components will be simulated and compared. Each component must be analyzed in detail to determine the appropriate individual specifications and overall hybrid system design to formulate a feasible static optimization problem.

#### 3.1. Internal Combustion Engines

An internal combustion engine converts chemical energy into mechanical energy through fluid expansion by combusting fuel with an oxidizer. The effectiveness of this process is called the fuel conversion efficiency ( $\eta_f$ ) shown in Eq. 1.<sup>31</sup> The efficiency of an engine is related to the heating value of the fuel and the specific fuel consumption. The heating value ( $Q_{HV}$ ) of a fuel is the amount of thermal energy released by the fuel during combustion. Typically, the lower heating value ( $Q_{LHV}$ ) of a fuel is used in the equation, indicating all water products remain as vapor.<sup>32</sup> The specific fuel consumption ( $SFC$ ), a measure of how efficiently an engine uses fuel to produce work, is the fuel flow rate ( $\dot{m}_f$ ) per unit power output ( $P$ ), as seen in Eq. 2.

$$\eta_f = \frac{1}{SFC \cdot Q_{HV}} \quad (1)$$

$$SFC = \frac{\dot{m}_f}{P} \quad (2)$$

Reciprocating ICEs convert fluid pressure on a piston into rotating mechanical power on a driveshaft. Most reciprocating engines operate on a four-stroke (Otto) cycle. As the name implies, the cycle consists of four strokes of a piston: an intake stroke, a

compression stroke, a power stroke and an exhaust stroke. As shown in Fig. 5, the four-stroke engine requires two complete crankshaft revolutions for each power stroke.<sup>31</sup> The two-stroke engine was developed to obtain a higher power-to-weight ratio (Fig. 6).<sup>31</sup> By also using the piston as the inlet and exhaust valve, a two-cycle engine only needs one crankshaft revolution for each power stroke. By using this simplified fluid control method, the weight of the engine is reduced creating high power in a lightweight package. While the two-stroke is superior to the four-stroke in power-to-weight ratio, the four-stroke compensates with greater fuel conversion efficiency and emission control.

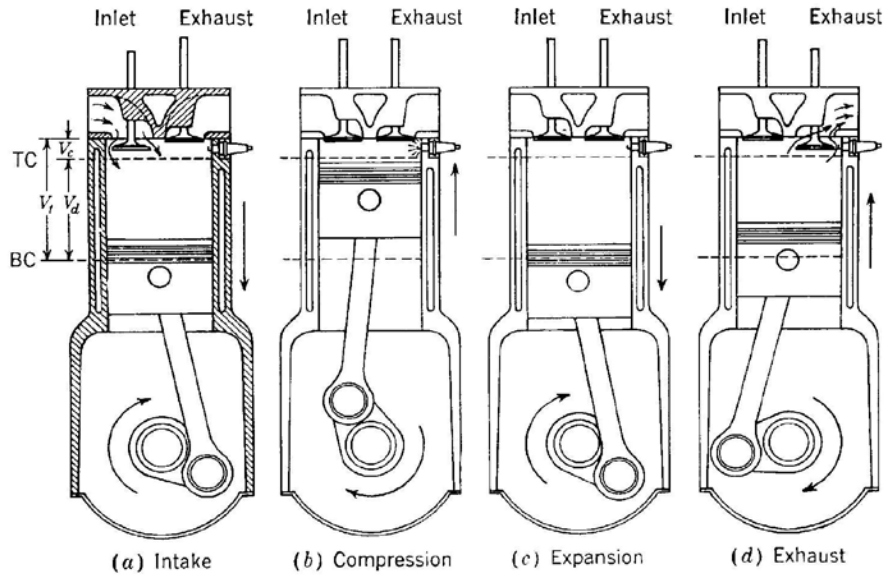


**Figure 5: Four-stroke operating cycle**

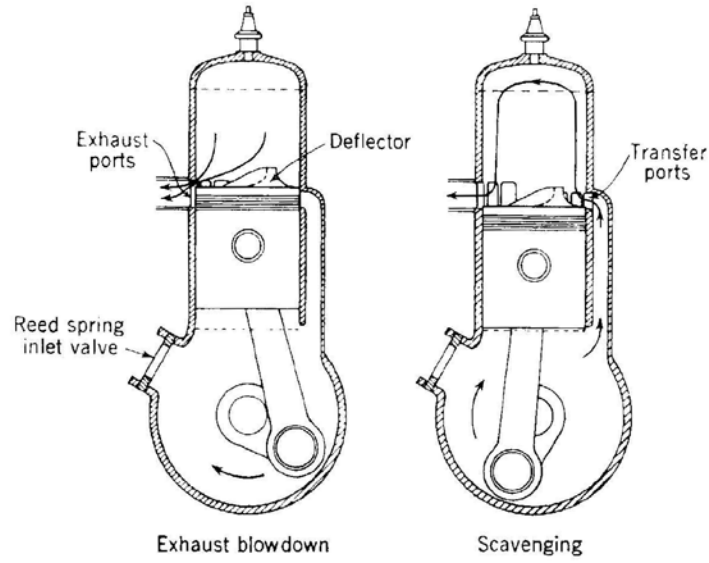


**Figure 6: Two-stroke operating cycle**

Power ( $P$ ) and torque ( $T$ ) are the most common descriptors of engine performance. These specifications are very useful, but are dependent on engine size. A useful relative performance measure is mean effective pressure (MEP), which is the work per cycle divided by the volume displaced per cycle.<sup>31</sup> Equation 3 also shows MEP in terms of the fuel conversion and volumetric efficiencies ( $\eta_v$ ), the fuel heating value, the ambient air density ( $\rho_\infty$ ) and the fuel-to-air ratio ( $F/A$ ). Equations 4 and 5 show torque and power respectively in terms of MEP, the displacement volume ( $V_d$ ), number of crank revolutions per power stroke ( $n_R$ ) and the crankshaft rotational speed ( $N$ ).

$$MEP = \frac{P n_R}{V_d N} = \eta_f \eta_v Q_{HV} \rho_\infty (F/A) \quad (3)$$

$$T = \frac{MEP \cdot V_d}{\pi n_R} \quad (4)$$

$$P = \frac{MEP \cdot N \cdot V_d}{2\pi n_R} \quad (5)$$

In order for an engine to be effective within a hybrid propulsion system, it must operate at or near its peak efficiency. To optimize fuel efficiency, an engine should run

at its minimum SFC. By plotting MEP against engine speed (RPM), a “performance map” is created showing lines of constant SFC. As shown in Fig. 7, the minimum SFC occurs at a partial throttle load.<sup>31</sup> The upper limit of the map demonstrates the full-throttle performance curve. The goal of a hybrid system should be to maintain engine operation within the “efficiency island” created by the minimum SFC contour line. During periods of high engine demand, a controller must calculate the maximum SFC gradient between the desired and current states. The controller will then ramp up the engine and/or motor throttle input to provide the required power in the most efficient manner.

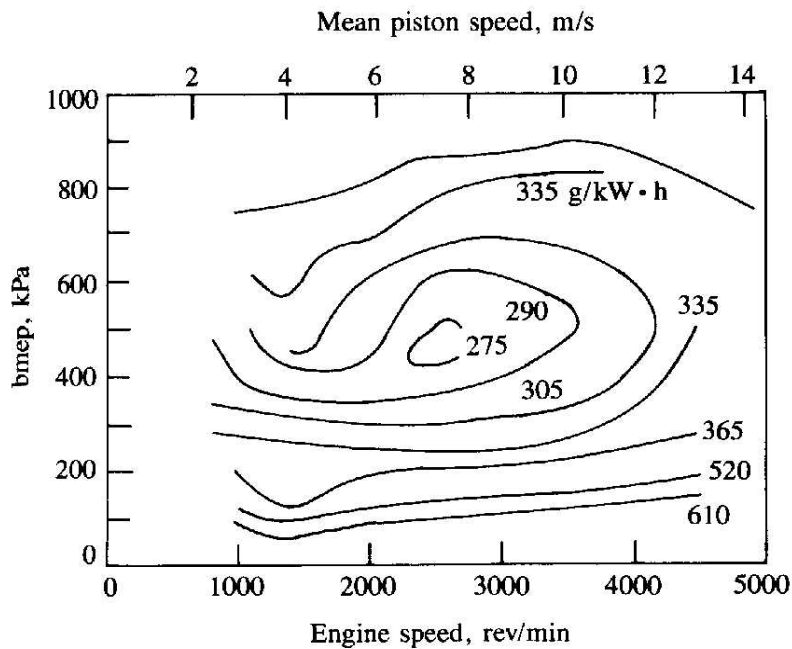


**Figure 7: Typical four-stroke engine performance map**

Currently, most small unmanned aircraft use two-stroke gasoline engines. The engines provide significant capability per dollar, but tend to have low endurance from high SFCs. Four-stroke gasoline engines provide lower SFCs at the expense of power-to-

weight. Theoretically, small diesel cycle engines could double the endurance of an aircraft with a two-stroke engine.<sup>10</sup> Significant advances must be made, however, for diesel engines to approach the power-to-weight ratios of gasoline engines. The high cylinder pressures and compression ratios required for the diesel cycle require materials not presently found in small ICEs. Weight reductions in ancillary components like turbochargers and cooling systems must also be achieved for use in aviation.

Since small UAS typically fly at low speeds and altitudes, several simplifying assumptions about engines are made. Power is reasonably constant with freestream air velocity due to negligible ram pressure at low airspeeds. For the same reason, SFC is also reasonably constant with freestream air velocity. SFC is also relatively insensitive to altitude changes associated with small ICE powered UAS.<sup>33</sup> Power, on the other hand, is directly affected by altitude change. As altitude increases, the shaft power output of an ICE decreases based on the approximation shown below, where  $P_0$  and  $\rho_0$  are sea level shaft output power and density respectively.<sup>33</sup>

$$\frac{P}{P_0} = 1.132 \frac{\rho}{\rho_0} - 0.132 \quad (6)$$

Despite the technological challenges, DoD is aggressively pursuing heavy fuels like diesel and JP-8 for all military engines. DoD Directive 4140.25 and NATO Standard Agreements (STANAGs) require using JP-8 (also known as F-34) as the common battlefield fuel.<sup>34</sup> Automotive and aviation gasoline are logistically difficult and expensive to support. Gasoline has a lower flashpoint than heavy fuels, which makes it more susceptible to explosion. Since most military vehicles use JP-8, the logistical cost of supporting a secondary and more dangerous fuel are very high. AFRL and other military laboratories are researching cycle conversion technologies. By converting small

ICEs to run on heavy fuels, the engines will be more logistically supportable even though the SFCs may not improve. The author has chosen to investigate both commercially available heavy fuel and gasoline engines for the hybrid design. Heavy fuel engines are the ultimate goal for the DoD, but may not be presently viable.

### **3.2. Electric Motors**

Electric motors produce mechanical energy through the interaction of magnetic fields and current carrying conductors. In a brushed direct current (DC) motor, brushes contact a commutator on a rotor to form a circuit between the electrical source and the motor's armature coil windings. In a brushless DC motor, the electromagnets are permanent and do not rotate. Instead of a brush-commutator system, brushless motors employ a controller to distribute power with a solid-state circuit. With fewer moving parts, brushless motors are more efficient and reliable. Brushless motors are typically more expensive to build and more difficult to control. Most electric motors may also be used as generators. For this case, a torque will be applied to the motor's shaft which will rotate the internal casing and generate electricity.

The physical configurations of the coil and magnets within brushless motors may take several forms. For the inrunner configuration, permanent magnets are mounted directly on the spinning rotor and are surrounded by the stator windings. The outrunner configuration uses the stator coils as the center of the motor, while the permanent magnets spin on a rotor that surrounds the coil center. Inrunner motors provide extraordinary rotational speed, but lack torque. In order to be viable for a propeller system, the inrunner motor must be geared down to reduce speed and increase torque. Outrunner motors spin much slower than inrunners and provide tremendous torque for

their size. Many radio control (R/C) aircraft use outrunner motors as direct drive motors to eliminate the need for a gearbox.

As demonstrated by Drela, the equivalent circuit shown in Fig. 8 provides a first-order model of a DC electric motor.<sup>35,36</sup> The motor's shaft torque ( $Q_m$ ) is proportional to the supplied current over the motor's torque constant ( $K_Q$ ) (Eq. 7). The shaft's rotational speed ( $\Omega$ ) is simply the product of the motor's internal back-EMF voltage ( $v_m$ ) and the speed constant ( $K_V$ ) (Eq. 8). Shaft power ( $P_m$ ) is the torque times rotational speed (Eq. 9). The efficiency of the motor ( $\eta_m$ ) is the ratio of the output shaft power to the input electrical power ( $P_e$ ) (Eq. 10). For the case of a generator, the efficiency ( $\eta_g$ ) will be the inverse of the motor efficiency proportionality (Eq. 11).

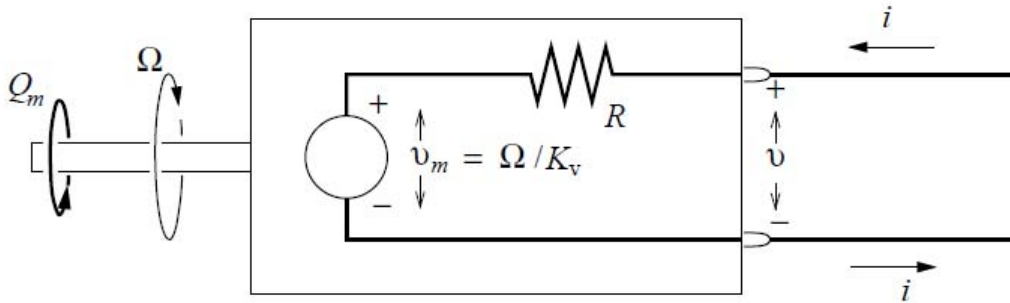


**Figure 8: Equivalent circuit for a DC electric motor**

$$Q_m = \frac{i - i_o}{K_Q} \quad (7)$$

$$\Omega = v_m \cdot K_v = (v - iR) \cdot K_v \quad (8)$$

$$P_m = \Omega \cdot Q_m = (i - i_o)(v - iR) \quad (9)$$

$$\eta_m = \frac{P_m}{P_e} = \frac{P_m}{i \cdot v} = (1 - i_o/i)(1 - iR/v) \quad (10)$$

$$\eta_{gen} = \frac{P_e}{P_m} \quad (11)$$

### 3.3. Rechargeable Batteries

Rechargeable batteries are electrochemical devices that convert chemical energy from stored inactive materials into electrical energy. The energy output of a battery is expressed by power integrated over time, where power is current times voltage, as shown by Eqs. 12 and 13. The theoretical specific capacity of a battery is solely dependent on the chemical composition of the material. Equation 14 shows the dependence of specific capacity on the number of electrons stored per mole of material ( $n$ ), the molecular weight ( $MW$ ) and the Faraday constant ( $F$ ) (96,485 C/mol).<sup>37</sup> A common descriptor of battery performance is specific energy ( $E_e$ ), which is the ratio of energy to mass (Eq. 15). The actual specific capacity ( $C$ ) and energy of a battery must also include the mass of electrolyte, binders and packaging, which do not contribute energy. Therefore, the actual performance of a battery is drastically lower than the theoretical capacity, particularly for small applications.

$$E = \int P(t)dt \quad (12)$$

$$P = IV \quad (13)$$

$$C = \frac{n}{3.6MW} F \quad (14)$$

$$E_e = CV = P/m \quad (15)$$

Table 1 compares specifications for common rechargeable batteries.<sup>38,39</sup>

Arguably, the most important battery characteristic for aviation purposes is a high specific energy. Correspondingly, most electric UAS use lithium-ion (Li-Ion) or lithium-polymer (Li-Po) batteries. Older battery technologies, like nickel cadmium (Ni-Cd) and nickel-metal-hydride (NiMH), have excellent stability characteristics, but have relatively poor specific energies and suffer from high self-discharge rates. A highly promising

battery chemistry, lithium-sulfur (Li-S), has a tremendous specific energy, but suffers from poor cycle durability.

**Table 1: Comparison of common rechargeable batteries**

	Ni-Cd	NiMH	Li-Ion	Li-Po	Li-S
Specific Energy (Wh/kg)	45-80	60-120	90-200	130-240	250-600
Cycle Durability	1500	300-500	300-1000	500-1000	100
Nominal Voltage (V)	1.25	1.25	3.3-3.8	3.7	2.1

Unlike some older battery technologies, lithium-based battery chemistries have a very specific charging profile. The charging time will not accelerate by supplying extra current. The charge (or discharge) current of a battery is defined by the “C-rate.” A battery specified to hold 500 mAh of energy would provide 500 mA of current for 1 hour at a 1C rate or 1 A for 30 minutes at a 2C rate. Typically, lithium batteries must charge at a 1C rate for about three hours for a full charge. A 70% state of charge may be reached after about one hour of charging. The charging and discharging characteristics of the lithium cells play a significant role in the design of a propulsion system’s battery pack.

### 3.4. Propellers

Propellers are essentially airfoils oriented vertically to the longitudinal axis of an airplane. Like any airfoil, propellers create friction, form, induced and wave drag. The drag on a propeller causes an efficiency loss on the propulsion system of an aircraft. The net power available ( $P_A$ ) to the freestream air from propeller is the product of the power supplied by the driveshaft ( $P$ ) and the efficiency of the propeller ( $\eta_p$ ) (Eq. 16).<sup>33</sup> The efficiency is a function of a dimensionless quantity, the advance ratio ( $J$ ), which is the

ratio of freestream velocity ( $V_\infty$ ) to the number of propeller revolutions per second ( $N$ ) and propeller diameter ( $D$ ) (Eq. 17).<sup>33</sup>

$$P_A = \eta_p P \quad (16)$$

$$J = \frac{V_\infty}{N \cdot D} \quad (17)$$

The coefficients of thrust ( $C_T$ ) and power ( $C_P$ ) are two other significant propeller parameters shown in Eqs. 18 and 19.<sup>40,41</sup> The power coefficient determines the amount of power that a propeller may impart to the freestream air for propulsion ( $P$ ) or absorb from as a windmill ( $P_w$ ) by Eqs. 19 and 20 respectively. The non-dimensional parameters are typically used to compare experimental data of geometrically similar propellers. The propeller efficiency may also be expressed in terms of the thrust and power coefficients and advance ratio (Eq. 21). Figure 9 demonstrates the relationship between efficiency and advance ratio with data collected by AFRL and NASA at the Basic Aerodynamics Research Tunnel (BART) for a Graupner 10"x8" (diameter x pitch) propeller.<sup>42</sup> The results show that the highest efficiency for this small propeller is only about 80%. Clearly, the performance of an aircraft propulsion system is largely dependent on the efficiency of its propeller.

$$C_T = \frac{T}{\rho \cdot N^2 \cdot D^4} \quad (18)$$

$$C_P = \frac{P}{\rho \cdot N^3 \cdot D^5} \quad (19)$$

$$P_w = \frac{1}{2} \rho A C_P V_\infty^3 \quad (20)$$

$$\eta = \frac{J \cdot C_T}{C_P} \quad (21)$$

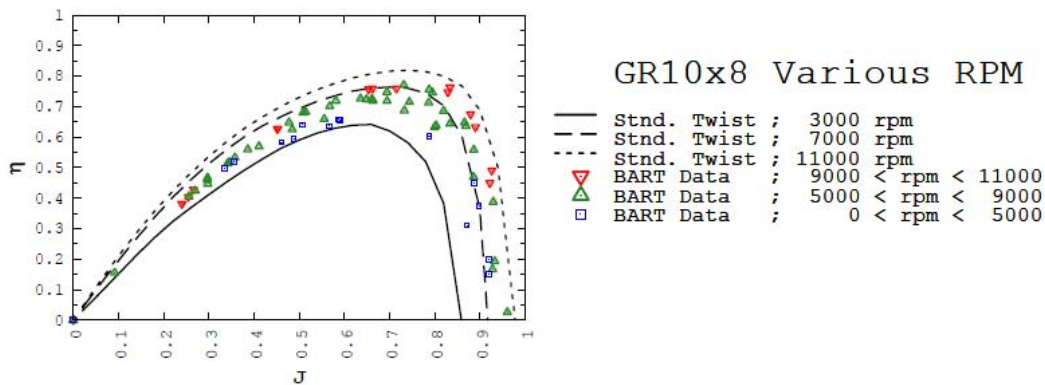


**Figure 9: Efficiency for Graupner 10''x8'' propeller**

In order to optimize a propeller driven system, the propeller and its power supply most both operate at or near their peak efficiencies. Since many electric motors operate most efficiently at higher RPMs than propellers, gearing is commonly used to reduce the shaft speed to better line up with the propeller's demand. Gearing adds more weight to an aircraft so a better approach may be to search for a different motor-propeller combination. As with any design procedure, the optimization is a careful tradeoff process.

Drela demonstrates the tradeoff between a well-matched and a poorly-matched motor-propeller pair in Fig. 10.<sup>36</sup> The well-matched pair operates within a small degree of the peak efficiency for each component. The poorly-matched system, on the other hand, wastes an exorbitant amount of power to provide the same thrust as the well-matched system. Drela's program QPROP provides a method of predicting the performance of a propeller-motor combination to ensure a well-matched system.<sup>43</sup>

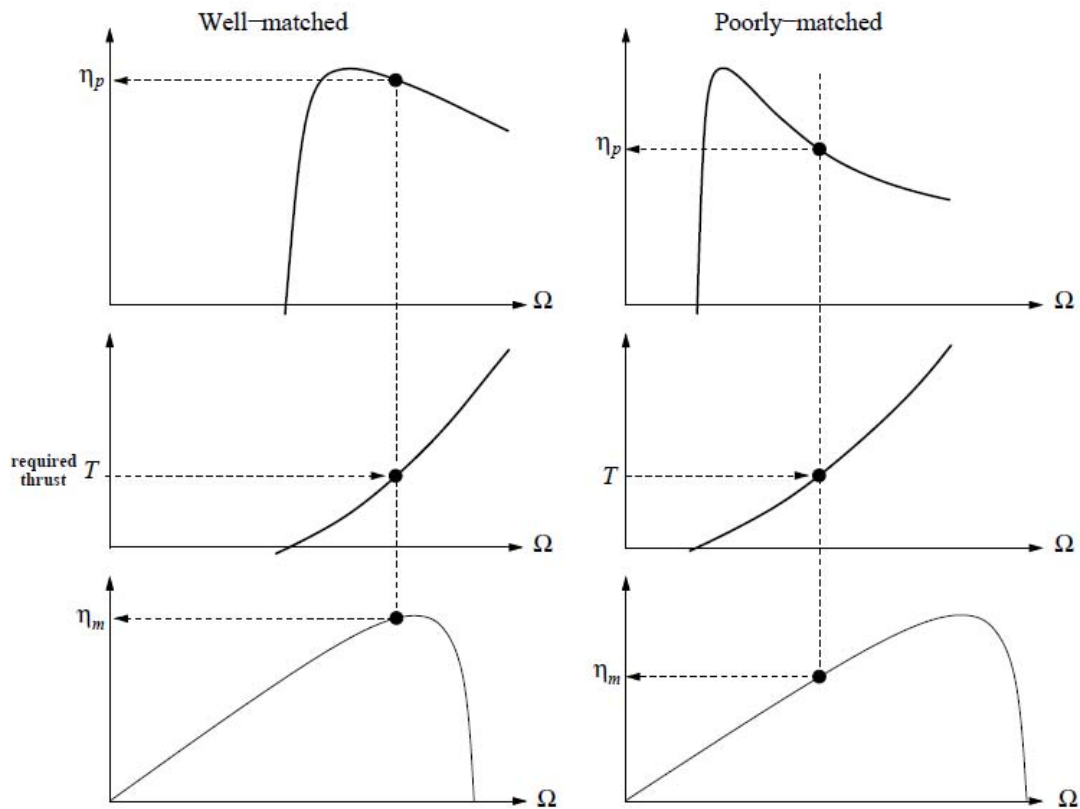


**Figure 10: Well-matched and poorly-matched motor and propeller pairs**

The preceding figure reveals why a hybrid-electric system designer must take great care when selecting the individual components. Without a robust selection process based on the underlying theory, a poor hybrid system design may combine the disadvantages of each component rather than the desired advantages. The subsequent chapter will outline one such process to select well-matched components for an optimized hybrid-electric propulsion system for an unmanned aircraft system.

### **III. Methodology**

#### **1. Chapter Overview**

Like all engineering disciplines, aircraft design is a highly iterative process. By incorporating a hybrid propulsion system, the complexity level increases further. Chapter 3 outlines the methodology used by the author to develop a conceptual design for a small hybrid-electric unmanned aircraft system. The chapter begins by outlining three different parallel hybrid configurations and three unique battery discharging strategies. The chapter closes with a discussion of the basic aerodynamic equations and optimization sequence utilized for each of the nine variations.

#### **2. Hybrid Configurations**

As previously mentioned, three distinct parallel hybrid-electric propulsion configurations are proposed. Each configuration consists of an internal combustion engine, an electric motor, a rechargeable battery pack and at least one propeller. The differences in the systems lie with the mechanical energy transfer mechanisms utilized by each design. Despite the mechanical variations, each system is based on the following regimes of operation as outlined by Harmon:<sup>44</sup>

- Take-off power provided by the ICE or the ICE and EM.
- Climbing power provided by the ICE or the ICE and EM.
- Maximum speed (dash) power provided by the ICE and EM.
- Cruise power provided by the ICE. A margin is needed to recharge the batteries during charge-sustaining operation.
- Endurance power provided by the EM for near-silent operation.

- Missed approaches and emergency power provided by the ICE and EM.

The first configuration, originally proposed by Harmon, is shown in Fig. 11.<sup>28, 44</sup>

This system uses an electromagnetic clutch to transfer power from the ICE to the propeller drive shaft. During endurance operation, a controller shuts down the ICE while the clutch allows the drive shaft to spin freely without turning the ICE. To restart the ICE for recharging or the return cruise, the controller activates the clutch, which causes the EM powered driveshaft to turn and start the ICE. Since the ICE and EM are aligned on the same shaft, the EM rotor will spin during all modes of operation. Rather than wasting the inertial and friction forces placed on the ICE by a freely rotating shaft, the EM is utilized as a generator to power the avionics, flight control systems and sensors. During this phase of operation, the propulsion system mirrors typical ICE powered UAS or automotive drive-trains where an alternator powers all electronics. Battery-power is only used by the hybrid system when additional propulsion power is required or during endurance operation. This configuration is the lightest option, but possesses the greatest mechanical inefficiency of the proposed options. The remaining options incorporate escalating weight penalties to decrease the associated mechanical losses.

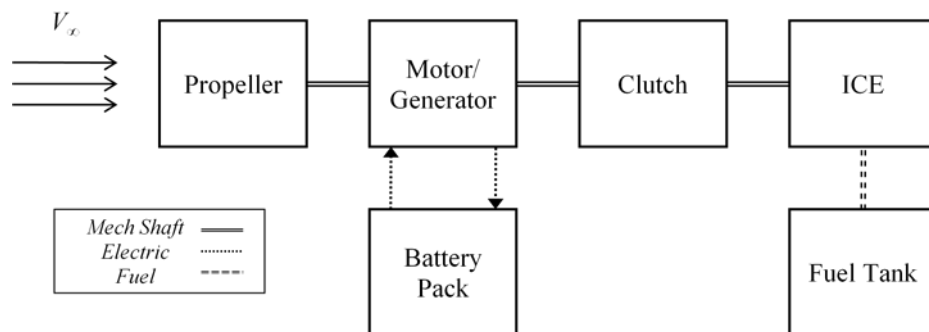


**Figure 11: Clutch-start parallel hybrid-electric configuration**

By adding a small electric starter, the second configuration of Fig. 12 provides a mechanically simpler option. Rather than relying on a clutch and matching the EM and ICE torques for starting purposes, a small, lightweight starter is attached to the ICE and powered by the main battery pack. Like the previous configuration, the electric-start configuration links the ICE and the EM to a single propeller driveshaft. Therefore, the avionics, flight control system and sensors are powered by the generator during cruise flight. Again, the battery pack is only used to provide excess propulsion power and endurance operation. By eliminating the clutch, this configuration provides a more reliable and efficient option for a small weight penalty.

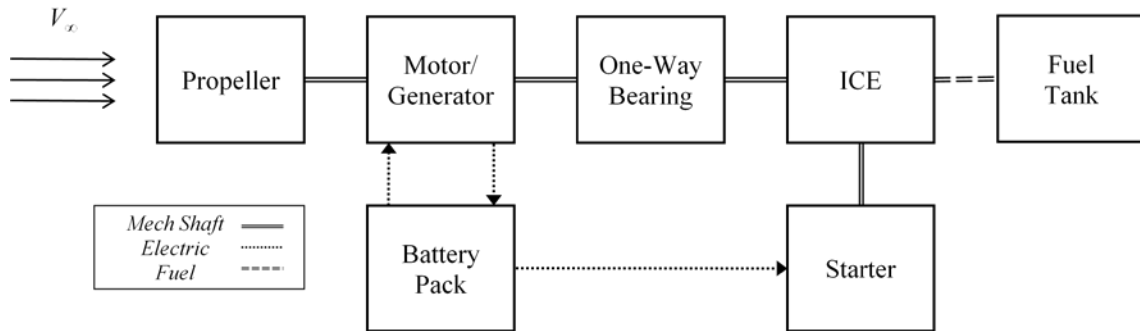


**Figure 12: Electric-start parallel hybrid configuration**

The final option uses an innovative dual-propeller propulsion system in a centerline-thrust configuration as shown in Figs. 13 and 14.<sup>45</sup> The relatively heavy ICE powers the front propeller to ensure adequate cooling and aircraft stability, while the EM and battery pack power the rear propeller through a second driveshaft. Since the power sources are decoupled, the propeller utilizes the freestream air like a windmill to turn the generator. The ICE is sized such that it is able to provide sufficient power for cruising, while overcoming the drag induced by the wind-milling rear propeller. Each propeller is able to fold rearward to minimize drag during different mission segments. When the

rear-propeller is folded to reduce drag, the battery pack must provide power to the avionics, flight control system and ISR sensors. Like the previous configuration, the centerline-thrust model also utilizes a small electric starter. By decoupling the ICE and EM, the aircraft possesses an advanced survivability through redundant power sources. This configuration is potentially the heaviest and least efficient, but provides innovative capabilities not seen in the previous options or existing aircraft. The configuration is expected to be the best option for missions that utilize a charge-depletion strategy.

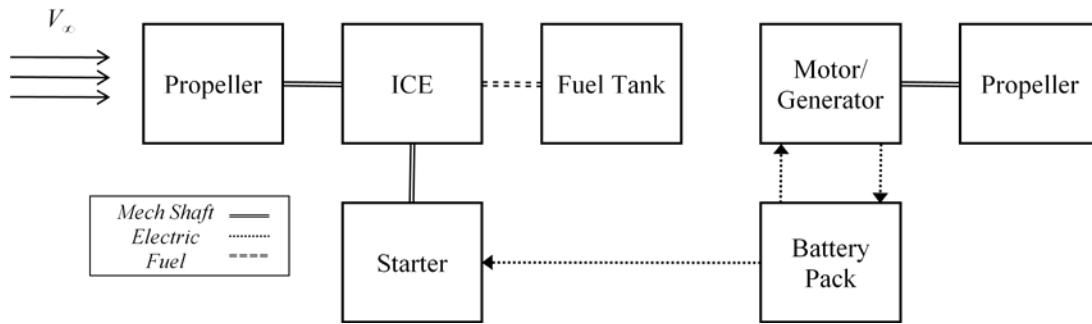


**Figure 13: Centerline-thrust hybrid configuration**



**Figure 14: Centerline-thrust hybrid-electric UAS conceptual design**

### **3. Battery Discharging Profiles**

In addition to the three hybrid propulsion configurations, three different battery discharging profiles are simulated. Each strategy possesses unique advantages and disadvantages adaptable to specific mission needs. The strategies begin simplistically and escalate in complexity to provide differing capabilities.

The first and simplest profile utilizes a charge depletion strategy in which battery recharging does not occur. This strategy allows the aircraft to use a smaller ICE since the engine size is optimized for the cruise flight power required only. The aircraft may use the battery pack to assist with climbing or dashes above cruising velocity, but will not recharge to full capacity and thus will reduce the endurance phase. The batteries are sized to provide the power necessary for steady-level flight, the flight control system and the payload during the specified endurance phase. The charge depletion strategy provides the option to use primary batteries, which can possess higher energy densities than secondary (rechargeable) batteries despite an increased logistics footprint.

By enabling the propulsion system to charge the battery pack, the charge sustaining strategy ensures the battery pack will be at or near a 100% state of charge to begin endurance operation. This second strategy sustains the battery pack at or near full capacity to maximize the energy available for electric-only loitering. The engine for the second strategy is optimized to power cruise flight, the flight control system, the ISR sensor payload and a specified margin for battery charging. The aircraft could feasibly be launched below full battery capacity and recharge on the way to the target area.

The final battery discharging strategy copies the optimization strategy of the previous method, but modifies the mission profile. Rather than providing a continuous

loitering period, the endurance flight is segmented to allow time to recharge the batteries. Since carbon-based fuels are approximately 75 times more energy dense than rechargeable lithium batteries, the strategy trades fuel mass for battery mass to increase the overall energy capacity of the propulsion system. The aircraft provides the same overall time for all-electric operation, but will add a specified number of recharging cycles. This methodology also allows the aircraft to provide geographically discontinuous surveillance. The UAS can provide ISR coverage in one area then recharge while traveling to another. Clearly, the segmented charge sustaining method requires the most complex controller, but significantly reduces the required battery pack mass. The segmented ISR strategy may not be sufficient for all mission types, but could provide dramatically increased performance on specialized missions with multiple ISR target locations.

#### **4. Aircraft Design Process**

The aircraft design process has been well defined by authors like Anderson and Raymer.<sup>33,46</sup> The highly iterative design method set forth by these authors is adapted and solved using the process described in Fig. 15. User specified mission and performance requirements, battery discharge strategy and hybrid configuration type are gathered and passed to the subsequent phase. The inputs are utilized by a series of functions in MATLAB to optimize the power required by the aircraft and perform various sizing calculations. The user is able to validate performance parameters such as propeller and motor efficiencies for the resultant component data using QPROP. Efficiency discrepancies are manually passed back to the optimization block until the resultant motor sizes, efficiencies and QPROP models match. The final output of the program

may not suit the mission needs of the user. For example, the output may indicate that the payload of the conceptual design is less than required for the ISR sensor platform. At this time, the user must iteratively adjust mission or performance requirements until the output matches the requirement and an acceptable design is reached.

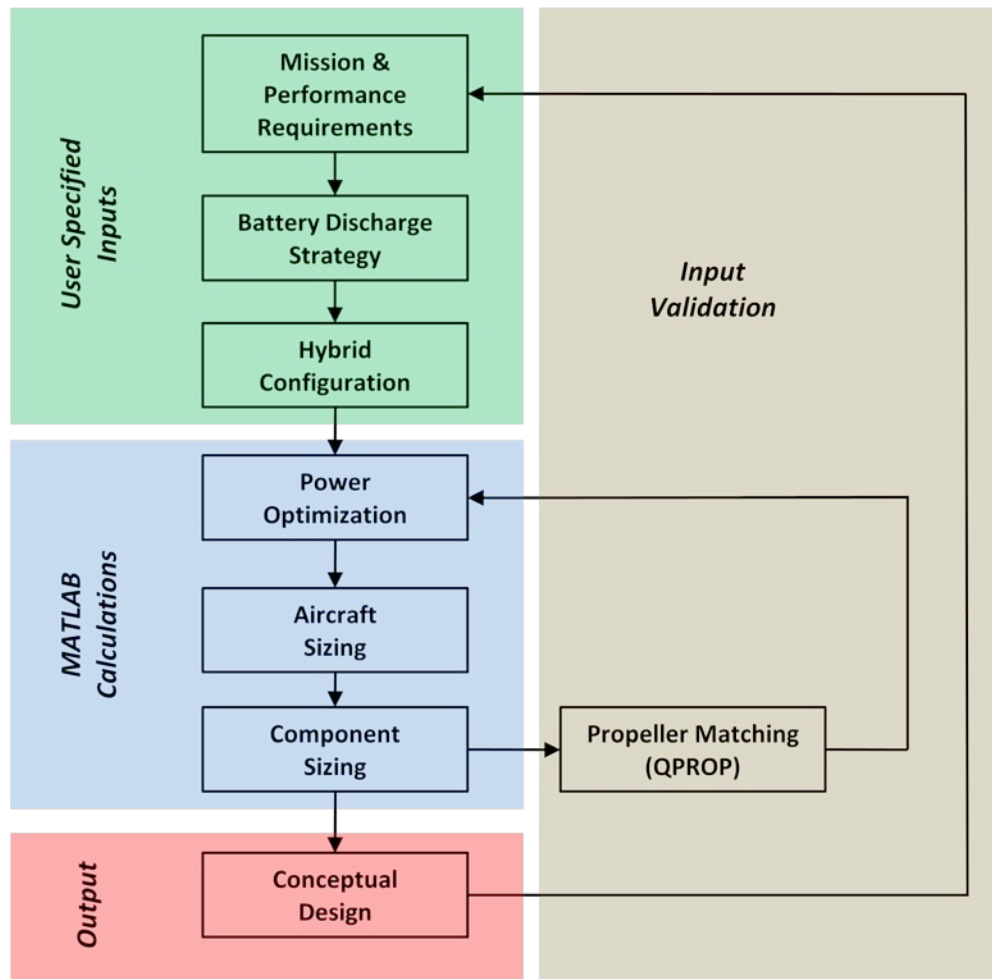


**Figure 15: UAS hybrid-electric propulsion design process**

## 5. Fundamental Aerodynamics

Fundamental aerodynamic equations form the foundation for all of the calculations performed within this research effort. By maintaining a simplistic approach,

the resulting code is easily adaptable to a wide variety of scenarios. The subsequent equation set may be found in any introductory aerodynamics text; however, the form will closely follow the syntax employed by Anderson.<sup>33</sup>

The source of aerodynamic lift and drag on a body are the pressure and shear stress distributions integrated over the body. The fundamental nature of the aerodynamic forces leads to dimensionless coefficients that describe the components of lift and drag. For example, the lift coefficient ( $C_L$ ) is simply the ratio of the lifting force ( $L$ ) to the dynamic pressure ( $q_\infty$ ) and the wing planform area ( $S$ ) as shown in Eqs. 22 and 23. The coefficient of drag ( $C_D$ ) is most commonly described by the drag polar equation (Eq. 24), where drag is related to the sum of the drag at zero-lift ( $C_{D,0}$ ) and the induced drag ( $C_{D,i}$ ) for subsonic flight. The zero-lift drag coefficient results from the parasitic effects of friction and flow separation over the aircraft's body. As shown by Eqs. 25 and 26, the induced drag is related to lift squared and a proportionality constant ( $K$ ), where  $e$  is the Oswald span efficiency factor and  $AR$  is the aspect ratio of a wing.<sup>33</sup>

$$C_L = \frac{L}{q_\infty S} \quad (22)$$

$$q_\infty = \frac{1}{2} \rho V_\infty^2 \quad (23)$$

$$C_D = C_{D,0} + C_{D,i} \quad (24)$$

$$C_{D,i} = K C_L^2 \quad (25)$$

$$K = \frac{1}{\pi e AR} \quad (26)$$

Several key assumptions help to simplify the process further. First, all situations assume steady, level flight, thereby neglecting dynamic flight conditions. Second, thrust is aligned with the freestream direction, meaning thrust equals drag ( $T=D$ ) and lift equals

weight ( $L=W$ ). Finally, only flight regimes associated with small UAS are considered. Therefore, the aircraft will experience both low Reynolds and Mach numbers thus eliminating compressibility effects. Additionally, the UAS will experience relatively small changes in altitude.

Since the ultimate goal of the project is to size a propulsion system, the power required from each component must be determined. The power required ( $P_R$ ) for an aircraft to maintain steady, level flight is shown in Eq. (27).<sup>33</sup> By determining the lift and drag coefficients for a specific flight condition, such as endurance, the power required to maintain that condition is easily calculated. The power required from each propulsive component shall be determined from the power required at various flight conditions.

$$P_R = \sqrt{\frac{2W^3 C_D^2}{\rho_\infty S C_L^3}} \quad (27)$$

## 6. Optimization

In order to maximize the endurance of any aircraft, the power required for flight is minimized to allow the optimal usage of its propulsive energy source. For the proposed hybrid-electric UAS, the most critical mission segment is the all-electric ISR loiter.

Therefore, the cost function for the UAS propulsion optimization is the power required at the endurance speed.<sup>28,44</sup> The minimized endurance power ensures the minimum battery pack mass when allowing for an ISR sensor payload and a specified maximum takeoff weight. The cost function ( $J_{end}$ ) is shown in Eq. 28 as the power required at endurance speed ( $P_{R,end}$ ). Propeller driven aircraft minimize the power required when the aircraft is flying such that the ratio  $\frac{C_L^{3/2}}{C_D}$  is maximized.<sup>33</sup> The ratio, also known as the endurance

parameter (Eq. 29), is applied to the cost function and rearranged by Harmon as shown in Eq. 30.<sup>28,44</sup>

$$J_{end} = P_{R,end} = \sqrt{\frac{2W^3 C_D^2}{\rho_\infty S C_L^3}} = W \left( \frac{C_D}{C_L^{3/2}} \right) \sqrt{\frac{2W}{\rho_\infty S}} \quad (28)$$

$$\left( \frac{C_L^{3/2}}{C_D} \right)_{max} = \frac{1}{4} \left( \frac{3}{K C_{D,0}^{1/3}} \right)^{3/4} \quad (29)$$

Rearranging, the cost function is:

$$J_{end} = P_{R,end} = W \sqrt{\frac{2W}{\rho_\infty S}} \frac{4C_{D,0}}{(3\pi e AR)^{3/4}} \quad (30)$$

The cost function must be constrained to ensure that the optimization process converges on a minimum value.<sup>47</sup> The four necessary constraint equations are borrowed from Harmon's derivations.<sup>28,44</sup> Based on a "rubber" aircraft approach six variables for the cost function and constraint equations were selected as follows: wing loading ( $W/S$ ), aspect ratio ( $AR$ ), maximum lift coefficient ( $C_{L,max}$ ), stall velocity ( $V_{stall}$ ), endurance velocity ( $V_{end}$ ), and ICE power ( $P_{ICE}$ ).<sup>28,44</sup> Equation 30 defines the power required for cruising by combining Eqs. 16, 24 and 27. The equation, as originally derived by Harmon, included a scale factor of 125% to provide a margin for avionics, payload and charging power.<sup>28,44</sup> Rather than scaling the cruise power, the power required from the generator ( $P_{gen}$ ) is incorporated as an additive term when calculating the ICE power shown in Eq. 32. The propeller efficiency ( $\eta_{prop, x}$ ) applied to the power generation ( $P_{gen}$ ) varies depending on the configuration. For single propeller designs, the term equals 1.0 meaning no efficiency loss. For the dual propeller design, the term is equal to the product of the cruise speed efficiencies of both propellers. The cruise power required term is divided by the propeller efficiency ( $\eta_{prop, 1}$ ) to reflect the ICE shaft power required to

reach cruise speed. The equation also includes a term ( $P_w$ ) for the power required to overcome the drag associated with the wind-milling propeller for power generation in the center-line thrust configuration. Equation 33 shows the power required for generation as the sum of the power for the flight control system and avionics ( $P_{FCS}$ ), the ISR sensor payload ( $P_{pay}$ ) and battery charging ( $P_{charge}$ ) divided by the efficiency of the generator ( $\eta_{gen}$ ). By applying Eqs. 31 and 33 to Eq. 32, the first constraint equation (Eq. 34) shows the ICE power required for cruising flight and electric power generation. The next constraint (Eq. 35) rearranges Anderson's equation for the velocity at the optimal endurance condition to demonstrate the effect of variable aspect ratio ( $AR$ ). Next, Eq. 36 solves Eq. 21 for the wing loading ( $W/S$ ) variable at stall conditions. Finally, Eq. 37 places a fixed margin on the difference between the stall and theoretical endurance velocities. Based on preliminary research, it was determined that the theoretical endurance velocity calculated by the process would never exceed the stall velocity. Equation 37 specifies the margin between the two to prevent the optimization process from forcing the endurance velocity towards zero. During real world operations, the actual velocity flown by the aircraft must be an additional margin above the stall speed to maintain safety of flight. The safety factor will be set to 5 knots above stall speed for the purposes of this project.

$$P_{R,cruise} = \frac{1}{2} \rho V_{cruise}^3 W C_{D,0} \frac{1}{W/S} + \frac{2W^2/S}{\rho V_{cruise} \pi e AR} \quad (31)$$

$$P_{ICE} = \frac{P_{R,cruise}/\eta_{prop,1} + P_w + P_{gen}/\eta_{prop,x}}{\eta_{mech}} \quad (32)$$

$$P_{gen} = \frac{1}{\eta_{gen}} (P_{fcs} + P_{pay} + P_{charge}) \quad (33)$$

Constraint Equations:

$$P_{ICE} = \frac{1}{\eta_{mech}} \left[ \frac{1}{\eta_{prop,1}} \left( \frac{1}{2} \rho V_{cruise}^3 W C_{D,0} \frac{1}{W/S} + \frac{2W^2/S}{\rho V_{cruise} \pi e AR} + P_w \right) + \frac{(P_{fcs} + P_{pay} + P_{charge})}{\eta_{prop,x} \eta_{gen}} \right] \quad (34)$$

$$\sqrt{AR} = \frac{2}{\rho_\infty} \sqrt{\frac{1}{3\pi e C_{D,0}}} \left( \frac{W}{S} \right) \frac{1}{V_{end}^2} \quad (35)$$

$$\frac{W}{S} = \frac{\rho V_{stall}^2 C_{Lmax}}{2} \quad (36)$$

$$V_{end} \leq V_{stall} - margin \quad (37)$$

The system of equations is solved using MATLAB's optimization function *fmincon*. The function utilizes the sequential quadratic programming (SQP), quasi-Newton method. The SQP method approximates second-order derivative information using first-order information. By including an approximation of the cost functions curvature, the search direction determination's accuracy improves, which in turn improves the convergence rate of the algorithm.<sup>47</sup> The gradient of the Lagrange function at two points provides an approximation update to the Hessian (second-order) of the Lagrange function. This approximation provides the information necessary to update the search direction. Once *fmincon* converges upon a solution, the minimized cost function and six variables are returned.

The resultant data are employed to determine the physical size of the aircraft's propulsion system. The mass of the ICE is determined based on typical power to weight ratios and component efficiencies. For charge depletion and sustaining profiles, the electric motor is simply sized for the shaft power required for the actual endurance speed. For the segmented ISR profile, the EM is sized to maximize its power generation capability. For single propeller designs, the electric motor power output is determined by Eq. 38, which is the sum of the power required to charge the battery for a specified time

( $t_{charge}$ ) and the power for the payload and avionics. The power required to charge the battery is the ratio of the battery's capacity ( $C_{batt}$ ) in Watt-hours and the charging time. The EM for the dual propeller configuration is sized to provide power sufficient for the maximum of either the power required to sustain endurance flight or the windmill power generation during cruise speed (Eq. 20). By selecting the maximum, the EM will be able to meet each requirement.

$$P_{EM} = (C_{batt}/t_{charge} + P_{payload} + P_{fcs}) \quad (38)$$

Equation 39 shows the gross takeoff weight ( $W_0$ ) as a function of weight fractions. The fuel weight fraction ( $W_f/W_0$ ) is determined by calculating the weight fraction for each mission segment ( $W_x/W_0$ ) and adding a conservative 6% margin for reserve and trapped fuel, as shown by Eq. 40.<sup>46</sup> Equation 40 shows the cruise segment fraction from the Breguet range equation for propeller driven aircraft, where  $r$  signifies the segment range. The next equation (Eq. 41) shows the derived weight fraction for a climb using the change in energy height ( $\Delta h_e$ ).<sup>48</sup> Previously, the code used Raymer's historical climb fuel fraction of 0.985, which may not be applicable to small aircraft performing at relatively low altitudes.<sup>46</sup> Since the aircraft is not burning fuel during the endurance segment, the corresponding weight fraction is 1.

$$W_0 = \frac{W_{payload}}{1 - (W_f/W_0) - (W_e/W_0)} \quad (39)$$

$$\frac{W_f}{W_0} = 1.06 \left( 1 - \frac{W_x}{W_0} \right) \quad (40)$$

$$W_{cruise} = \exp \frac{-r \cdot SFC}{\eta_{prop}(L/D)} \quad (41)$$

$$W_{climb} = \exp \frac{-SFC \cdot \Delta h_e}{1 - D/T} = \exp \frac{-SFC \cdot \Delta h_e}{1 - 0.5 \rho V^2 S \frac{C_{D,0} + K C_{L,max}^2}{P_{R,climb}/V}} \quad (42)$$

The final piece of the propulsion system, the battery pack, is sized using typical specific energy values for commercially available products. As shown in Eq. 43, the battery pack mass is a function of the power required, the time required, and the specific energy. For the nine hybrid variations there are two possible battery sizing equations. The first and simplest equation (Eq. 44) calculates the battery mass during charge sustaining missions whether or not they are segmented. If the endurance loiter is segmented, the endurance time ( $t_{endure}$ ) in the Eq. 44 represents the time for the first segment. The duration of the remaining  $n$  segments is based on the charging rate of the battery pack. The final equation (Eq. 45) sizes the battery pack for charge depletion missions. The charge depletion battery must also provide payload and avionics power during the cruise segment and provide boost power as necessary for climbing ( $P_{climb}$ ).

$$m_{battery} = \frac{P_R t}{E_e} \quad (43)$$

$$m_{battery} = \frac{(P_{EM}/\eta_{EM} + P_{pay} + P_{FCS})t_{endure}}{E_e} \quad (44)$$

$$m_{battery} = \frac{(P_{EM}/\eta_{EM})t_{endure} + (P_{pay} + P_{FCS})(t_{endure} + 2t_{cruise}) + P_{climb}t_{climb}}{E_e} \quad (45)$$

The weight fractions for each mission segment and propulsion component are critical to the comparison of the nine propulsion system designs. Since the weight fractions for each design are normalized by the same maximum gross takeoff weight, the results provide a simple, direct means of comparison. The results, shown in the subsequent chapter, demonstrate the merits of each design, particularly through battery weight, fuel consumption and payload capacity. A comprehensive listing of the equations utilized in the MATLAB file is shown in Appendix A.

## **IV. Analysis and Results**

### **1. Chapter Overview**

The chapter begins by disclosing the input data used in the code and a justification for their selection. The results of the MATLAB optimization code are then displayed in nine sets of data for three unique hybrid configurations each having three different battery discharging strategies. After analyzing and comparing the results, the chapter closes with recommended mission profiles for each design.

### **2. Input Data**

A great level of effort was required to determine the appropriate input parameters. Like any modeling and simulation project, the outcome was dependent on the specific inputs. Slight deviations could potentially cause dramatically different results. In order to provide a level means of comparison, each of the nine designs began with the same set of input data. Since the data were selected from a wide variety of sources, both the English and SI measurement systems were used initially. The input parameters are displayed in both systems in this section, but the MATLAB code exclusively uses the SI system for simplicity. The remainder of this section elaborates on the justification behind the selection of each parameter.

The first step in aircraft design should always be to define a mission need. The size, shape and performance characteristics of the vehicle are ultimately driven by this first step. After conversations with the US Army's Maneuver Center of Excellence, the mission need was defined as providing stealthy ISR coverage for three hours starting

within one hour after a cruise distance of at least 40 nautical miles. The Army's current all-electric UAS platforms are only able to fly for a fraction of this defined ISR coverage need.

Ideally, the Army or Air Force would provide an initial capabilities document (ICD) to outline the specific requirements sought by the end users. Without further war-fighter guidance, the author further defined more specific mission and performance requirements as found in Table 2. Preliminary simulation results indicated that a three hour endurance time may not be feasible for all test cases due to the weight of the batteries. The requirement was held at three hours to determine which designs, if any, could meet the Army's need. The cruise velocity, maximum velocity and rate of climb requirements were chosen to compete with those advertised for similar fielded aircraft such as Insitu's *ScanEagle* and AAI's *Aerosonde Mark 4.4*, as displayed in Table B-1 in the Appendix.

The altitudes were selected based on current USAF operations. The elevation of Bagram Airfield, Afghanistan is 1492 meters (MSL), whereas the elevation of Joint Base Balad, Iraq is only 49 meters (MSL).<sup>49</sup> By setting the takeoff altitude to a worst case scenario of 1500 meters (MSL) and the mission altitude to 300 meters (AGL), the UAS should be able to perform out of nearly any USAF forward operating location. The baseline mission requirements may not be the ideal solution for any of the designs, but provide a level means to compare the nine hybrid design variations.

**Table 2: Baseline mission requirements**

<i>Description</i>	<i>MATLAB Variable</i>	<i>English</i>		<i>SI</i>	
		<i>Value</i>	<i>Units</i>	<i>Value</i>	<i>Units</i>
Endurance time ( $t_{endure}$ )	perf_tendure	3	hr	3	hr
One-way cruise time ( $t_{cruise}$ )	perf_tcruise	1	hr	1	hr
Cruise velocity ( $V_{cruise}$ )	perf_Vcruise	40	kts	20.5	m/s
Max velocity ( $V_{max}$ )	perf_Vmax	60	kts	30.9	m/s
Rate of climb ( $ROC$ )	perf_ROC	400	ft/min	2.03	m/s
Takeoff altitude MSL ( $h_{TO}$ )	h_TO	4921	ft	1500	m
Mission altitude AGL ( $h$ )	h_AGL	984	ft	300	m

The detailed aircraft design parameters are spelled out in Table 3. The initial set of parameters was taken directly from Harmon and updated to better reflect current technology.<sup>28, 44</sup> The maximum takeoff weight of 30 lbf remains unchanged from Harmon’s optimum design. The data for the ISR sensor payload are conservatively based upon the *Alticam 400 Series* camera used by the *ScanEagle*, which requires only 6 W and weighs only 1.38 lbf.<sup>50</sup> The value for the flight control system power is a conservative figure based upon the *Kestrel Autopilot*, which requires less than 5 W with a negligible weight (0.017 kg).<sup>51</sup> The wing area and aspect ratios are also directly from Harmon’s design, but are only used on a comparison basis within the MATLAB results display. The final wing area and aspect ratios of the UAS are calculated by the optimization formulation. The empty weight fraction was originally selected by Harmon to closely approximate existing aircraft (Table B-1); the value is used to compare the hybrid-electric design to an ICE-powered UAS. The actual empty weight fraction of the hybrid-electric UAS is calculated by the program. The original values for the zero-lift drag coefficient and span efficiency factors were 0.036 and 0.85 based on the form factor method and existing aircraft data. Finally, the fuel weight fractions for warm-up/takeoff and landing

were set to 0.999 and 0.9975, respectfully. The aircraft design assumed a catapult launch so the corresponding fuel requirement is very low. The value for landing was originally approximated by Raymer’s historical value of 0.995. However, the low altitudes and the gliding capability of the UAS would require substantially less fuel for an approach and landing.

**Table 3: Aircraft design parameters**

<i>Description</i>	<i>MATLAB Variable</i>	<i>English</i>		<i>SI</i>	
		<i>Value</i>	<i>Units</i>	<i>Value</i>	<i>Units</i>
Max gross takeoff weight/mass	des_uas_m	30	lbf	13.6	kg
Payload weight/mass	des_pay_m	5	lbf	2.27	kg
Payload power ( $P_{pay}$ )	des_pay_P	0.034	hp	25	W
Avionics/flight control system power ( $P_{FCS}$ )	des_fcs_P	0.013	hp	10	W
Original Wing area ( $S$ )	des_uas_S	15.9	ft <sup>2</sup>	1.48	m <sup>2</sup>
Original Aspect ratio ( $AR$ )	des_uas_AR	14.6		14.6	
Original empty weight fraction ( $W_e$ )	WF_empty	0.63		0.63	
Zero-lift drag coefficient ( $C_{D,o}$ )	uas_Cdo	0.036		0.036	
Oswald span efficiency factor ( $e$ )	uas_e	0.85		0.85	
Warm-up and Takeoff Weight Fraction	WF_TO	0.999		0.999	
Landing Weight Fraction	WF_landing	0.9975		0.9975	

The next set of input parameters describes the propulsion system components. Table 4 shows the results of a market survey for R/C aircraft components. The details for ICE’s and EM’s are shown in Table B-2 and Table B-3 in Appendix B. The EM efficiency value of 85% is a conservative estimate based on values claimed by manufacturers for outrunner motors. After discussions with several manufacturers, the generator efficiency was set to 75%. Each manufacturer claimed their outrunner motors were able to function as generators, but did not have efficiency testing data. Additionally, the motors would require a custom controller. The EM power-to-weight

ratio and EM over-torque factor were conservatively based on market averages. The efficiency for each hybrid configuration was notionally based on their mechanical complexity.

Small engine manufacturers are notorious for overinflating their advertised power and fuel consumption data. Therefore, the author took an overly conservative approach when analyzing ICE specifications. Ultimately, the power-to-weight ratio was chosen to be 0.75 hp/lbf, which is roughly 33% less than commercially advertised. Additionally, the author recognizes that the engine's most efficient point will not be at its peak power setting. The engine must be rated higher than the required cruise power to run efficiently during that condition. Since reliable specific fuel consumption data was not advertised for any of the engines, the author borrowed testing data on the *OS-91* engine from the AFRL Propulsion Directorate.<sup>52</sup> Alternatively, given an engine efficiency value and fuel type, the code was designed to calculate specific fuel consumption. This feature will not be utilized for this project since SFC was provided.

The masses for the clutch, electric starter and propeller were all selected from commercially available items. The electromagnetic clutch, rated at 1 Nm dynamic and 1.5 Nm static torque, was from RM Hoffman. The *FEMA On-Board Starter* from Hobby Lobby, Inc. was designed for R/C engines larger than 0.40 cc.<sup>53</sup> The propeller mass was found to be typical for the 20x8 size. Since R/C motor controllers typically weigh 50 grams or less and all other figures are overly conservative, the controller mass was ignored.

Table 1 in Chapter 3 shows typical specific energy ranges for COTS batteries. Like the other components, a market survey was performed to refine the ranges down to a

realistic value. Manufacturers of lithium chemistry batteries, such as LG Chem and Amit Industries, advertised specific energy values as high as 230 Wh/kg for their lithium-ion polymer cells. Ultimately, a more conservative value of 175 Wh/kg was used for lithium-ion polymer (Li-Po) batteries. Producers of the cutting edge lithium-sulfur (Li-S) batteries were much more difficult to find. Sion Power claimed 350 Wh/kg, but a more conservative 300 Wh/kg was used.<sup>39, 54</sup> Sion’s Li-S batteries have not yet reached mass production levels, but should be available in the foreseeable future. Since one goal of the design was to use current COTS products, the baseline mission used the Li-Po battery value. The dramatic performance gain associated with Li-S technology will be demonstrated in later sections.

**Table 4: Propulsion component specifications**

<i>Description</i>	<i>MATLAB Variable</i>	<i>English</i>		<i>SI</i>	
		<i>Value</i>	<i>Units</i>	<i>Value</i>	<i>Units</i>
EM efficiency ( $\eta_{EM}$ )	EM_eff	0.85		0.85	
EM generator efficiency ( $\eta_{GEN}$ )	EM_eff_gen	0.75		0.75	
EM over-torque factor	EM_overtrq	1.75		1.75	
Mech efficiency for clutch-start ( $\eta_{mech}$ )	mech_eff	0.95		0.95	
Mech efficiency for electric-start ( $\eta_{mech}$ )	mech_eff	0.98		0.98	
Mech efficiency for centerline-thrust ( $\eta_{mech}$ )	mech_eff	0.995		0.995	
EM power-to-weight ratio	EM_PW_ratio	2	hp/lbf	3288	W/kg
ICE power-to-weight ratio	ICE_PW_ratio	0.75	hp/lbf	1233	W/kg
Cruise specific fuel consumption ( <i>SFC</i> )	SFC_cruise	1.0	lbf/hp/hr	1.66E-06	N/Ws
Endurance specific fuel consumption ( <i>SFC</i> )	SFC_endure	1.5	lbf/hp/hr	2.49E-06	N/Ws
Clutch mass ( $m_{clutch}$ )	start_m	0.33	lbf	0.15	kg
Electric starter mass ( $m_{starter}$ )	start_m	0.66	lbf	0.30	kg
Propeller mass ( $m_{prop}$ )	prop_m	0.37	lbf	0.17	kg
Li-Po Battery Specific Energy ( <i>E</i> )	bat_ED	271	Btu/lbf	175	Wh/kg
Li-S Battery Specific Energy ( <i>E</i> )	bat_ED	464	Btu/lbf	300	Wh/kg

The original propeller efficiency value implemented by Harmon was a constant 75% for all flight conditions. Based upon further research and preliminary simulations with QPROP, the efficiency value was split into flight regime categories: climb, cruise and endurance. The QPROP results, shown in Table B-4, demonstrated propeller efficiencies for both cruise and endurance speeds approaching 80% for the tested motor-propeller combinations. In most test cases, the cruise efficiency exceeded the endurance efficiency. Theoretically, by reducing the pitch of the propeller, the efficiency at lower speeds should improve while diminishing the efficiencies at higher speeds. While not all tested reduced pitch propeller-motor arrangements verified this premise, those with an 8x6 propeller did show the trend. The author postulated that a reduced pitch, longer diameter blade, such as 20x8 or 16x6, matched to an appropriately sized EM would provide the propeller efficiencies shown in Table 5. Unfortunately, geometry files for these propeller sizes were not available to model in QPROP. In the end, the clutch-start, electric-start and the second (rear) centerline-thrust propeller are sized for optimal efficiency (80%) during endurance speed. The front propeller for the centerline-thrust configuration is sized for cruising speed since it is mated to the ICE. In all cases, the climbing efficiency is assumed to be relatively poor at 60%.

**Table 5: Propeller efficiencies**

<i>Configuration</i>	<i>Condition</i>	<i>Efficiency</i>
Clutch-Start	Climb	0.60
	Cruise	0.78
	Endurance	0.80
Electric-Start	Climb	0.60
	Cruise	0.78
	Endurance	0.80
Centerline-Thrust Prop #1	Climb	0.60
	Cruise	0.80
	Endurance	0.78
Centerline-Thrust Prop #2	Climb	0.60
	Cruise	0.78
	Endurance	0.80

The final inputs, shown in Table 6, are the upper and lower bound limits placed upon the optimization variables. As before, the bounds were chosen based on a survey of existing aircraft and preliminary simulation results. Logically, by creating a highly aerodynamically efficient aircraft the cost function (endurance power required) will be minimized. Therefore, the optimization routine should tend toward a glider-like design. Consequently, the wing loading constraint is expected to be active on the lower limit. The lower limit was carefully selected to reflect a practical structural design and closely approximate the wing loading of the glider-like battery-powered *Pointer* UAS. The maximum lift coefficient bounds were selected from a survey of traditional wing cross section data and assumed high-lift devices like flaps would not be used. The upper bound on  $C_{L,max}$  should act as an active constraint on the system allowing the aircraft to fly at the slowest possible speed. The remaining variables ( $AR$ ,  $V_{stall}$ ,  $V_{endure}$ , and  $P_{ICE}$ ) are bounded

by typical ranges for small UAS. The final optimized values for the four variables are not expected to be limited by these bounds.

**Table 6: Optimization variable bounds**

<i>Optimization Variable</i>	<i>Lower Bound</i>	<i>Upper Bound</i>	<i>SI Units</i>
Wing loading ( $W/S$ )	90	200	N/m <sup>2</sup>
Aspect ratio ( $AR$ )	8	20	
Max lift coefficient ( $C_{L,max}$ )	1	1.25	
Stall velocity ( $V_{stall}$ )	5	20	m/s
Endurance velocity ( $V_{endure}$ )	5	30	m/s
ICE power ( $P_{ICE}$ )	300	3000	W

### 3. Baseline Mission Results

#### 3.1. Optimization and Aircraft Conceptual Design Results

The results from the optimization routine are listed in Table 7 for the aforementioned baseline mission profile. This set of results applies to each of the nine hybrid variations. As expected, the wing loading was the lowest permitted value and the aspect ratio indicates a glider-like aircraft design. The wing loading result was used along with the calculated aspect ratio and specified takeoff weight to define the geometry for a rectangular wing. The cross-section for the wing can be chosen from any typical design (i.e. NACA, Selig, Eppler, or MH) meeting the calculated maximum lift coefficient requirement of 1.25. The theoretical endurance, stall and actual endurance speeds were also determined and are later used to size the electric motor.

**Table 7: Optimization and aircraft conceptual design results**

<i>Parameter</i>	<i>Value</i>	<i>Units</i>
Wing loading ( $W/S$ )	90.00	N/m <sup>2</sup>
Aspect ratio ( $AR$ )	14.42	-
Max lift coefficient ( $C_{L,max}$ )	1.25	-
Stall velocity ( $V_{stall}$ )	11.84	m/s
Theoretical endurance velocity ( $V_{endure, theo}$ )	9.27	m/s
Actual endurance velocity ( $V_{endure, act}$ )	14.41	m/s
Wing planform area ( $S$ )	1.48	m <sup>2</sup>
Wing span ( $b$ )	4.62	m
Wing chord ( $c$ )	0.321	m

As previously stated, preliminary simulations indicated that the theoretical endurance speed would occur below the stall speed of the aircraft. The predictions were realized as shown by Table 8 and Fig. 16. The power required curve shows the theoretical endurance speed as the minimum required power. The actual endurance speed was set to 5 kts above stall and was a modest increase in power (37 W) above the theoretical endurance speed. The climb power required was calculated based on the power required to maintain endurance speed relative to the ground while providing the required rate of climb. The cruise and maximum velocities are simply calculated with the respective speed requirements. The power requirements shown reflect only the aerodynamic power required from the propeller to maintain the indicated speed. At this point, the payload, flight control system and charging power requirements and energy losses are not incorporated. These issues varied between each of the nine designs and will be evidenced in the following section.

**Table 8: Power required results**

<i>Mission Segment</i>	$P_R$ (W)	$V$ (kts)
Theoretical Endurance	87.4	18.0
Stall	96.8	23.0
Actual Endurance	124.2	28.0
Climb	367.9	28.0
Cruise	265.7	40.0
Max Velocity	828.1	60.0

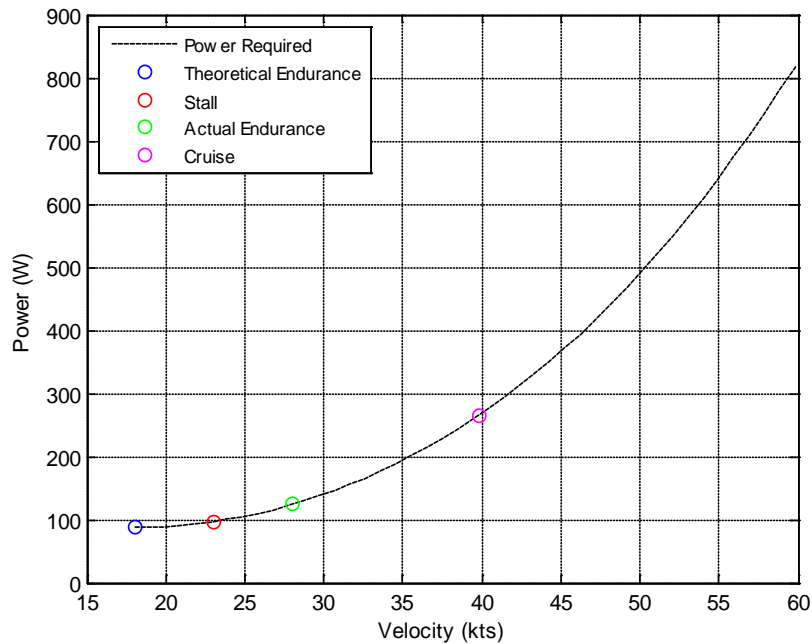


**Figure 16: Power required curve**

### **3.2. Charge Depletion Strategy**

The charge depletion strategy traded power generation capability for weight savings. By reducing the size of both the engine and motor/generator, the aircraft was able to carry a greater proportion of batteries. The results of the three individual hybrid variations are analyzed and compared below.

### 3.2.1. Clutch-Start Configuration

The first three figures portray the results for the charge depletion clutch-start configuration alongside the “original” or ICE-only powered aircraft with the same aerodynamic parameters. While the original empty aircraft weighed only 63% of the maximum takeoff value, the hybrid empty weight accounted for just over 89% despite nearly halving the fuel requirement. The all-electric endurance loiter enabled fuel savings of 0.428 kg. Each aircraft consumed the same amount of fuel for the remaining mission segments. The batteries comprised approximately 31% of the aircraft’s weight leaving only 7% or 0.960 kg for the payload capacity, which does not meet the requirement of 2.27 kg (5 lbf).

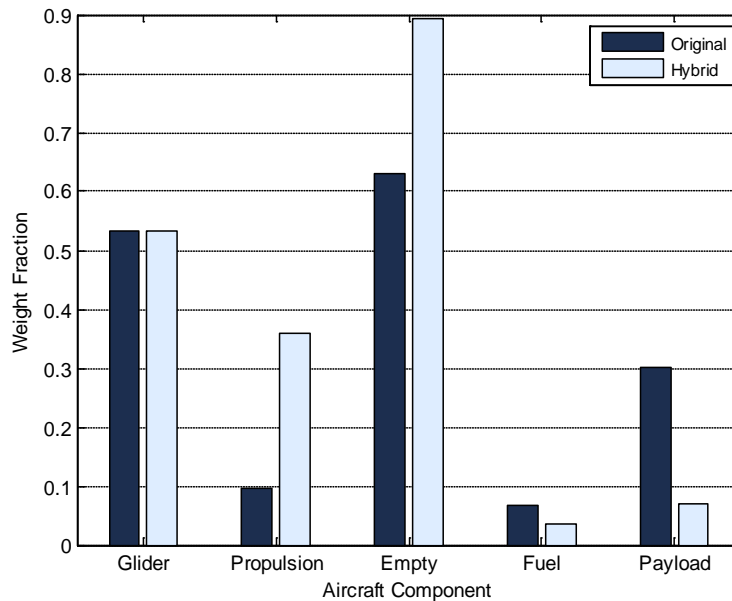


**Figure 17: Charge depletion, clutch-start aircraft component weight fractions**

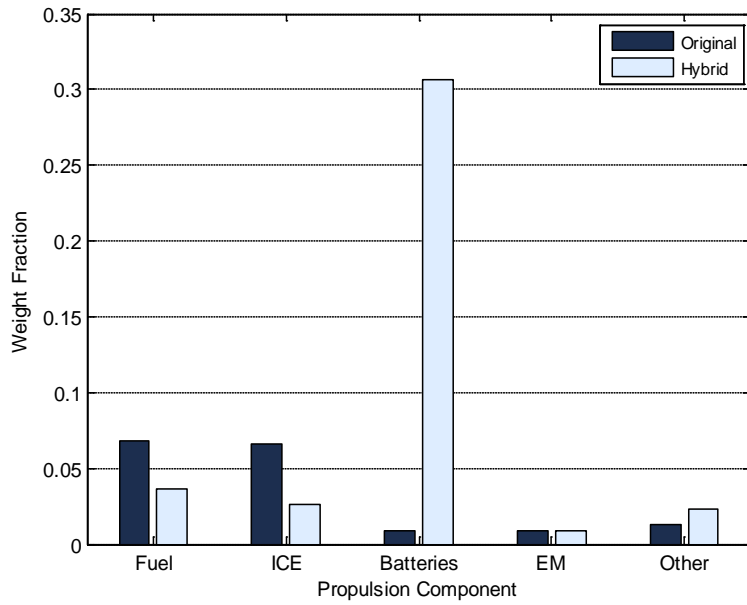


**Figure 18: Charge depletion, clutch-start propulsion component weight fractions**

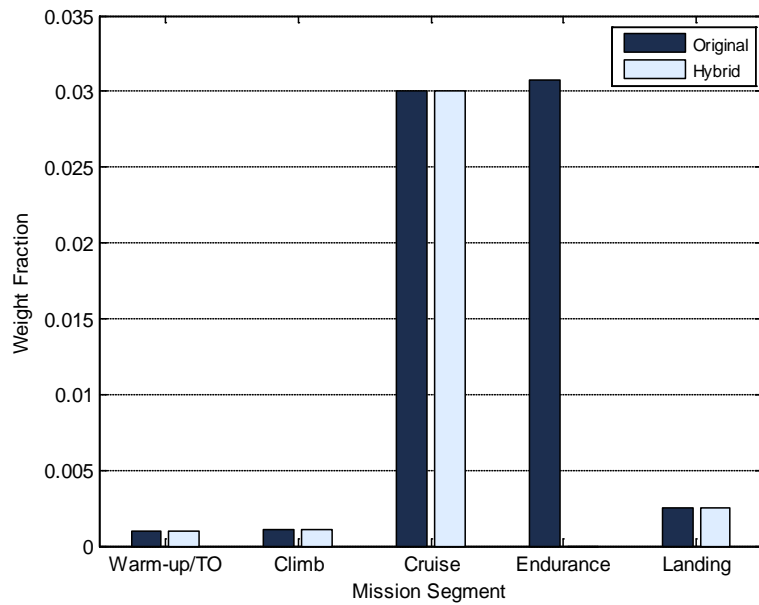


**Figure 19: Charge depletion, clutch-start mission segment fuel weight fractions**

### 3.2.2. Electric-Start Configuration

Figures 20 through 22 for the electric-start configuration describe very similar results to the previous hybrid design. In this case, the hybrid empty weight accounted for just over 90%. The reduced mechanical efficiency afforded by eliminating the clutch was not enough to overcome the increased weight of the electric starter. Again, the endurance phase allowed the aircraft to substantially reduce the fuel consumed over the entire mission. Due to the batteries comprising 31% of the aircraft's weight and the additional starter weight, only 6% or 0.816 kg remained for the payload. The charge depleting electric-start configuration also did not meet the payload requirement.

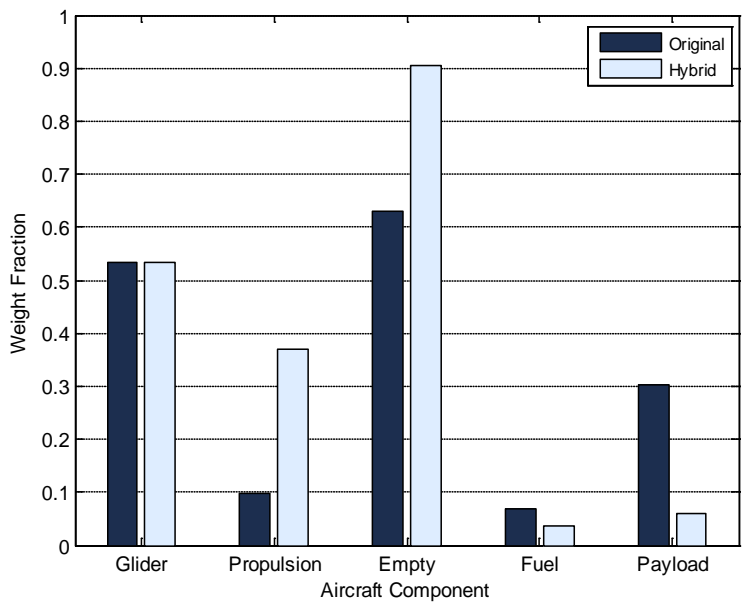


**Figure 20: Charge depletion, electric-start aircraft component weight fractions**

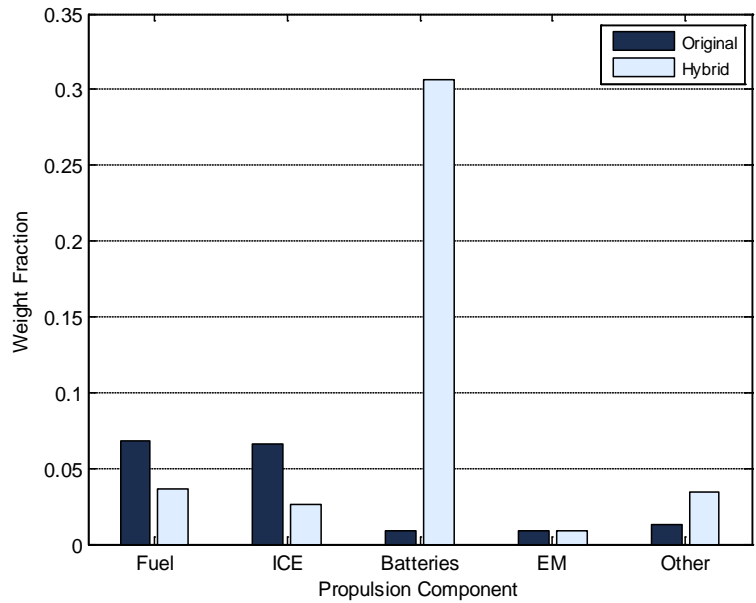


**Figure 21: Charge depletion, electric-start propulsion component weight fractions**

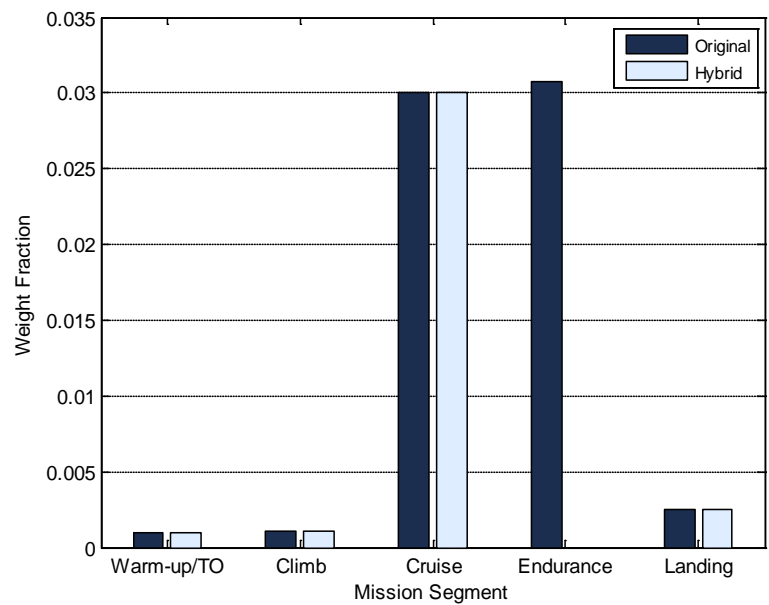


**Figure 22: Charge depletion, electric-start mission segment fuel weight fractions**

### 3.2.3. Centerline-Thrust Configuration

The centerline-thrust configuration provided the most energy efficient aircraft design for a charge depleting strategy. The mechanical inefficiencies of a clutch and the motor and engine sharing a single shaft were all removed and the propeller efficiency during cruise was improved. The greater propeller efficiency and battery-powered loiter led to fuel savings of 0.439 kg. The added weight of the second propeller and the electric-starter caused a relatively high empty weight fraction of 92%. The payload capacity of only 0.648 kg provided only 29% of the requirement.

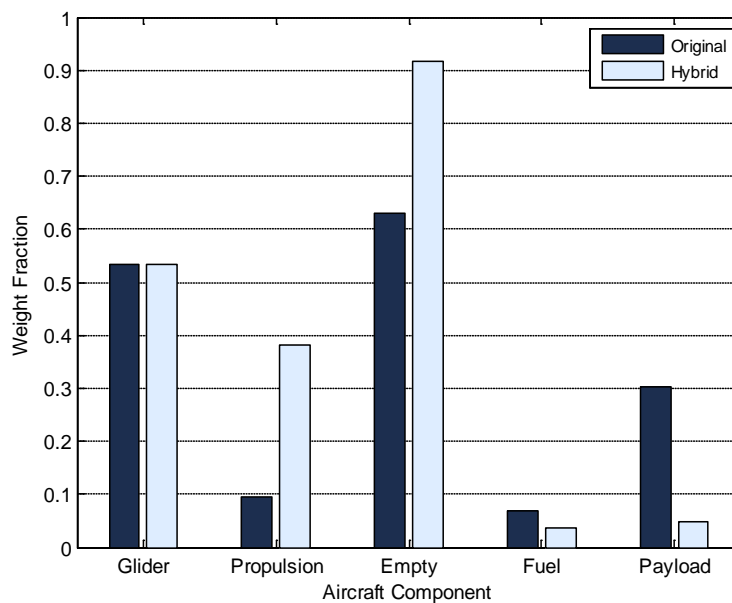


**Figure 23: Charge depletion, centerline-thrust aircraft component weight fractions**

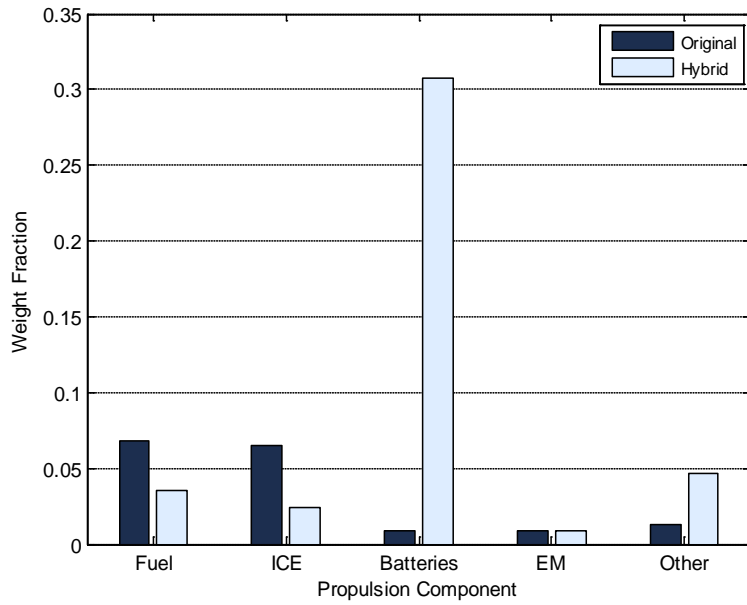


**Figure 24: Charge depletion, centerline-thrust propulsion component weight fractions**

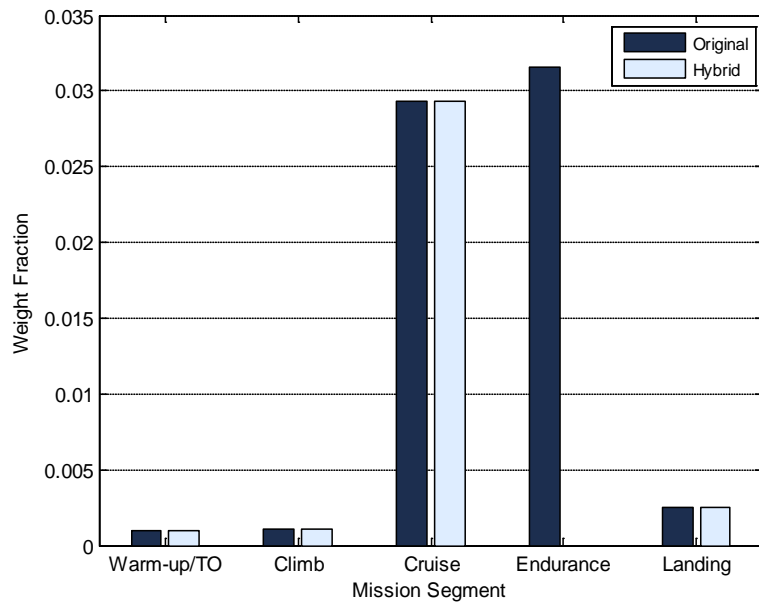


**Figure 25: Charge depletion, centerline-thrust mission segment fuel weight fractions**

### 3.2.4. Comparison

The performance results obtained for the three hybrid variations for charge depleting were very similar as shown in Figs. 26 and 27. Since the aircraft lacked any power generation capability, the electric motor was sized for the power required for the endurance flight only, which was equivalent in each case. The ICE's were sized for the cruise power required, which differed slightly due to varying mechanical and propeller efficiencies. The dual propeller design required the smallest engine and burned the least fuel thanks to its more efficient design. The lack of power generation required that the battery packs be sufficiently large to power the three hour endurance segment, the payload and avionics throughout the entire mission, and any boost power needed for climbing. The relatively small engines required additional power from the motors to climb at the specified rate. Since the engine sizes varied slightly, the boost power required for climbing also varied slightly. Consequently, the resulting battery storage capacities varied in proportion to the engine sizes. In the end, none of the designs met the payload requirement of 2.27 kg. The closest design to the requirement was the clutch-start design due to the lowest propulsion system weight. The dual propeller design was the most fuel-efficient but provided the smallest payload capacity resulting from its heavier propulsion system.

**Table 9: Propulsion system component specifications**

**Charge Depletion:**

<i>Hybrid Type</i>	$P_{ICE}$ (W)	$P_{EM}$ (W)	$C_{BATTERY}$ (Wh)	$m_{ICE}$ (kg)	$m_{EM}$ (kg)	$m_{BATTERY}$ (kg)	$m_{PAY}$ (kg)	$m_{FUEL}$ (kg)	$m_{EMPTY}$ (kg)	$W_e$
Clutch-Start	438.9	155.2	730.0	0.356	0.047	4.171	0.960	0.496	12.14	0.89
Electric-Start	429.9	155.2	730.3	0.349	0.047	4.173	0.816	0.496	12.29	0.90
Centerline-Thrust	406.5	155.2	731.3	0.330	0.047	4.179	0.648	0.485	12.47	0.92

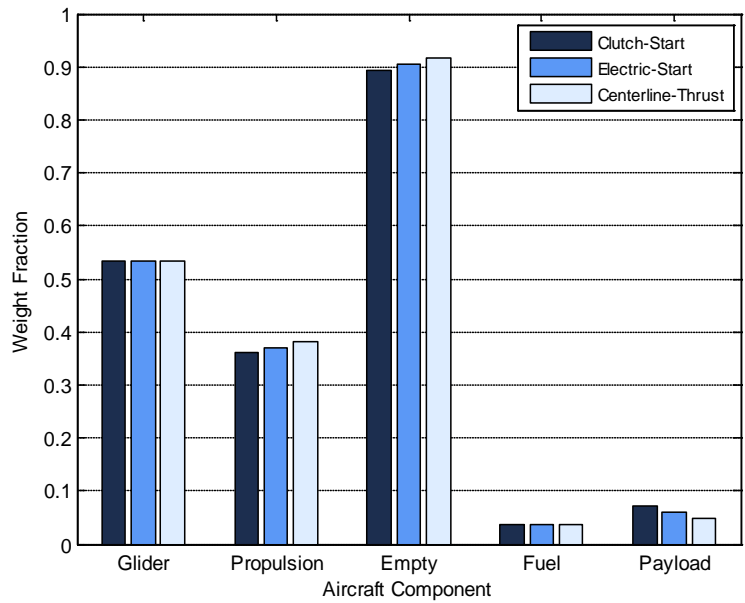


**Figure 26: Charge depletion aircraft component weight fraction comparison**

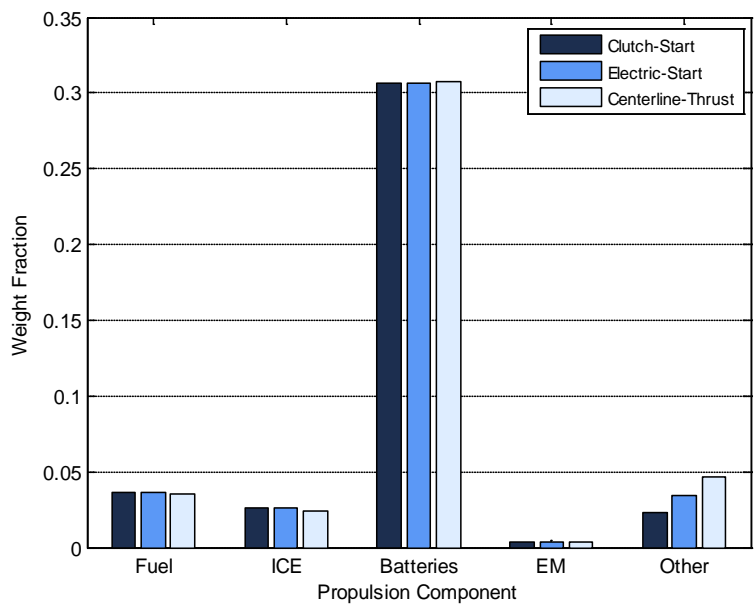


**Figure 27: Charge depletion propulsion component weight fraction comparison**

### **3.3. Charge Sustaining Strategy**

The previous strategy accepted a larger battery pack for smaller propulsion components by ignoring power generation. The charge sustaining strategy utilized the power generation capability of the ICE-EM combination to decrease the demand on the battery pack. The results for this strategy are described below.

#### **3.3.1. Clutch-Start Configuration**

Figures 28 through 30 depict the results for the charge sustaining clutch-start configuration alongside an ICE-only powered aircraft. In this case, the hybrid empty weight accounted for about 87% of the takeoff weight, a slight improvement over the charge depletion model. The original UAS required the ICE to be sized for both climbing and maximum speed. Since the hybrid required only that the ICE provide power for cruising and the generator, the engine sized decreased by 47% over the original. The all-electric endurance loiter enabled fuel savings of 0.370 kg or 30.5% compared to the original UAS. The batteries comprised 27% of the aircraft's weight leaving only 9% or 1.225 kg for the payload, which does not meet the requirement of 2.27 kg (5 lbf). The power generation capability increased the payload capacity by 0.265 kg over the charge depletion version, but required slightly more fuel (58 grams).

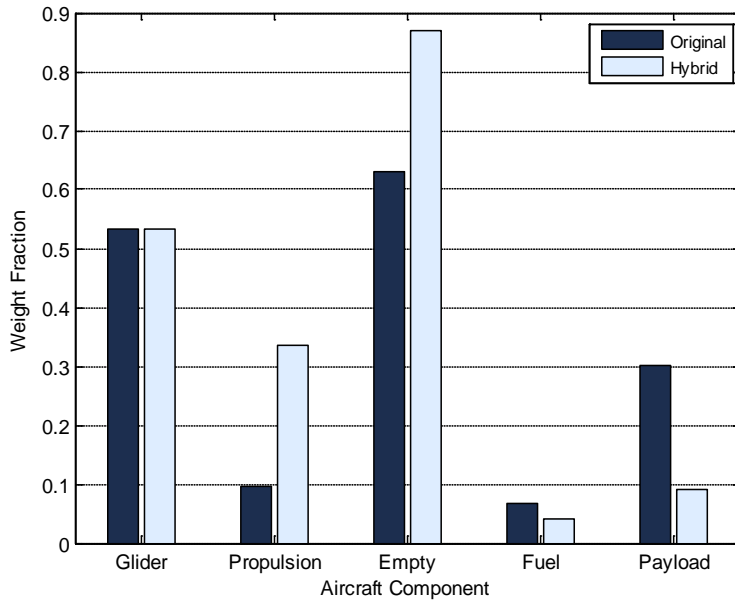


**Figure 28: Charge sustaining, clutch-start aircraft component weight fractions**

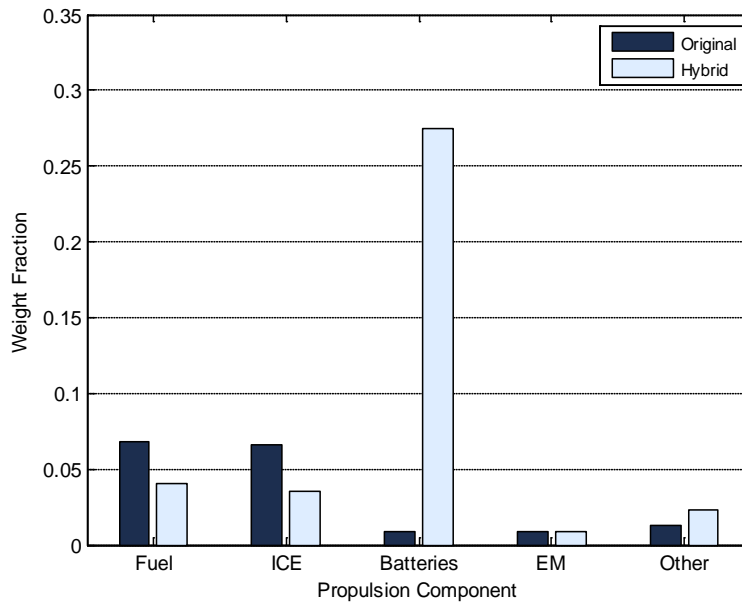


**Figure 29: Charge sustaining, clutch-start propulsion component weight fractions**

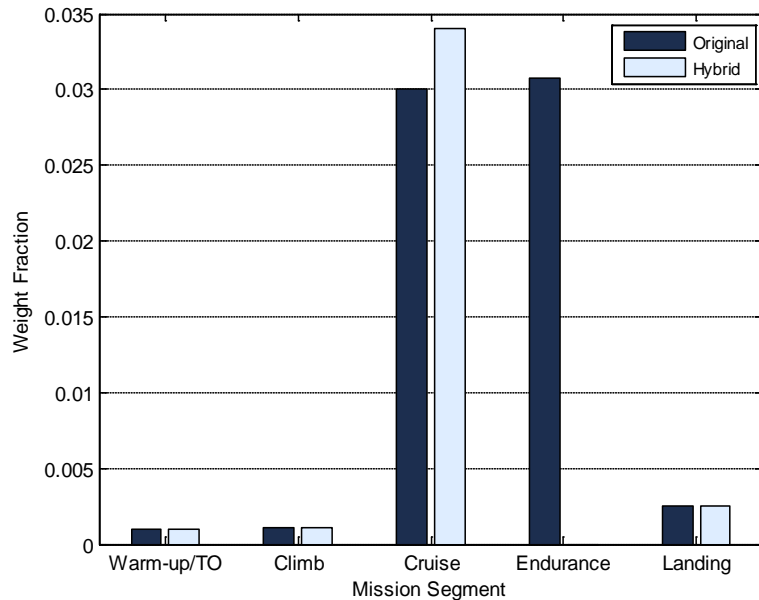


**Figure 30: Charge sustaining, clutch-start mission segment fuel weight fractions**

### 3.3.2 Electric-Start Configuration

Results for the charge sustaining electric-start configuration follow in Figs. 31 through 33. The electric starter in the propulsion system increased the empty weight fraction to 88%, which is slightly larger than the clutch-start version. The engine size decreased 48% from the original. The mechanical advantage achieved by eliminating the clutch allowed a slightly smaller ICE than the clutch-start variation. The design provided the same fuel savings of 0.370 kg as the previous variation when compared to the original. The batteries also comprised 27% of the aircraft's weight, but the greater overall propulsion system weight left only 1.085 kg for the payload.

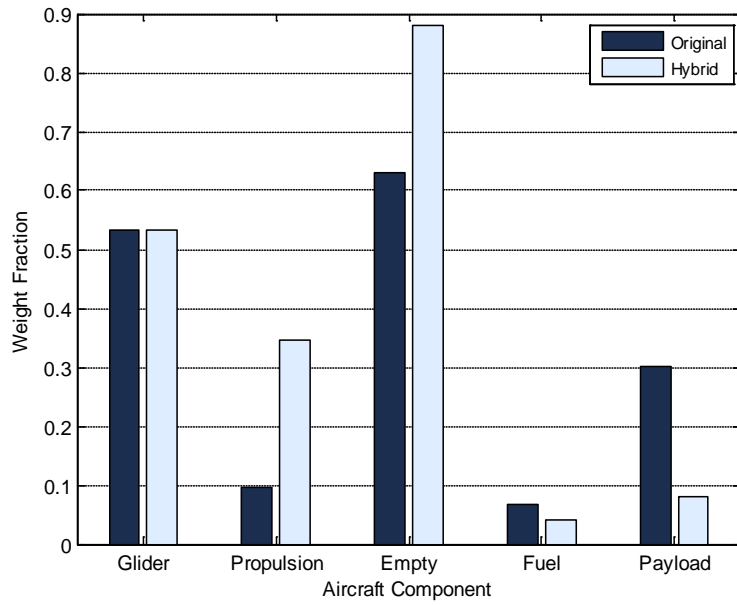


**Figure 31: Charge sustaining, electric-start aircraft component weight fractions**

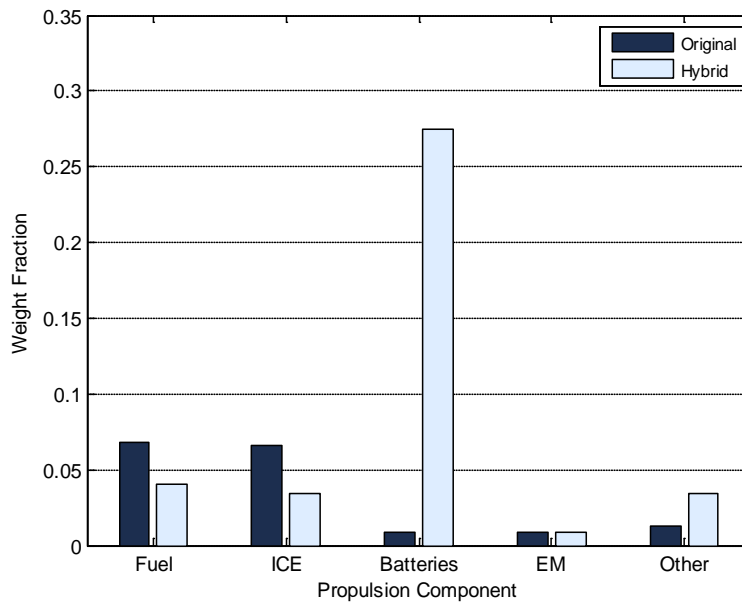


**Figure 32: Charge sustaining, electric-start propulsion component weight fractions**

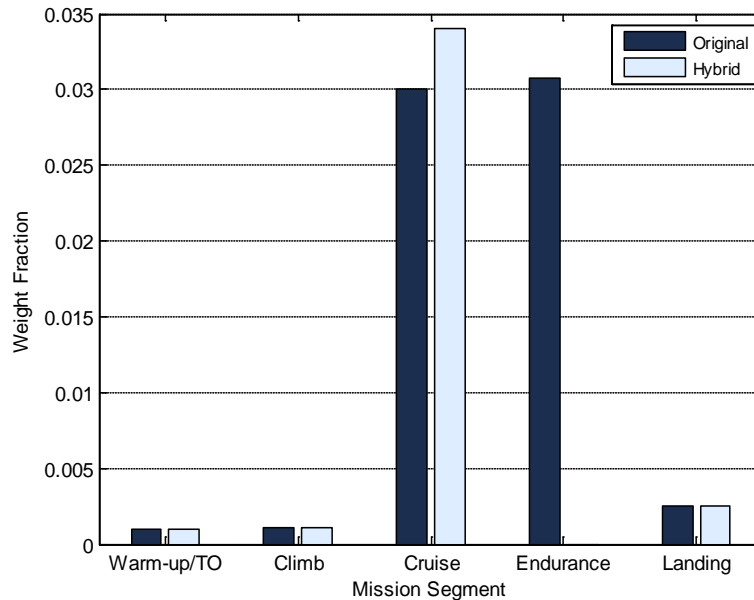


**Figure 33: Charge sustaining, electric-start mission segment fuel weight fractions**

### 3.3.3 Centerline-Thrust Configuration

The results for the centerline-thrust configuration showcase its remarkably poor charging ability. Since the generator is decoupled from the ICE and connected to a second propeller, the ICE output does not directly relate to electric power generation. Instead, the power generation is determined by the amount of power absorbed by the wind-milling propeller. As a result, the engine must be substantially larger than the single propeller designs to provide sufficient charging capability. The ICE size still managed to decrease 25% compared to the original, but was 33% larger than either competing design. The larger engine caused the empty weight to balloon to 91%. Since the wind-milling propeller provided power for the payload and avionics during ICE operation, the fuel requirement during cruise dramatically increased. The overall fuel requirement only decreased 95 grams compared to the original UAS, despite three hours of battery powered flight. The payload was a meager 0.407 kg.

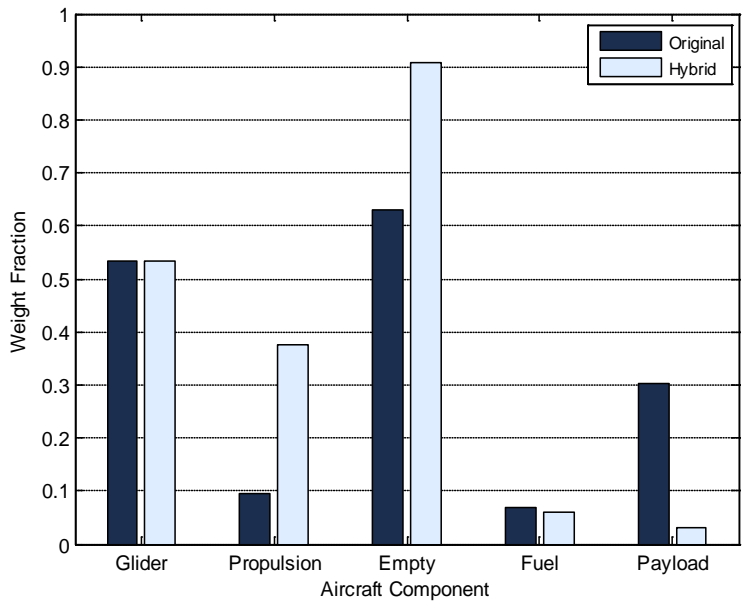


**Figure 34: Charge sustaining, centerline-thrust aircraft component weight fractions**

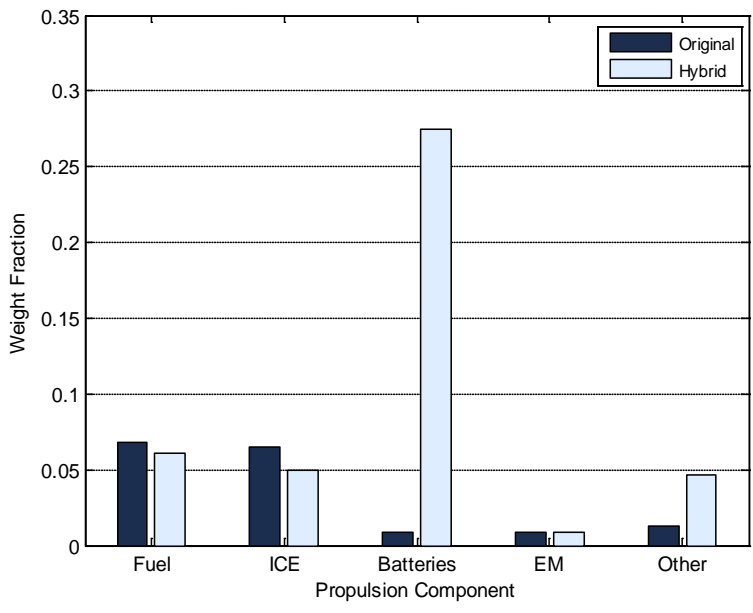


**Figure 35: Charge sustaining, centerline-thrust propulsion component weight fractions**

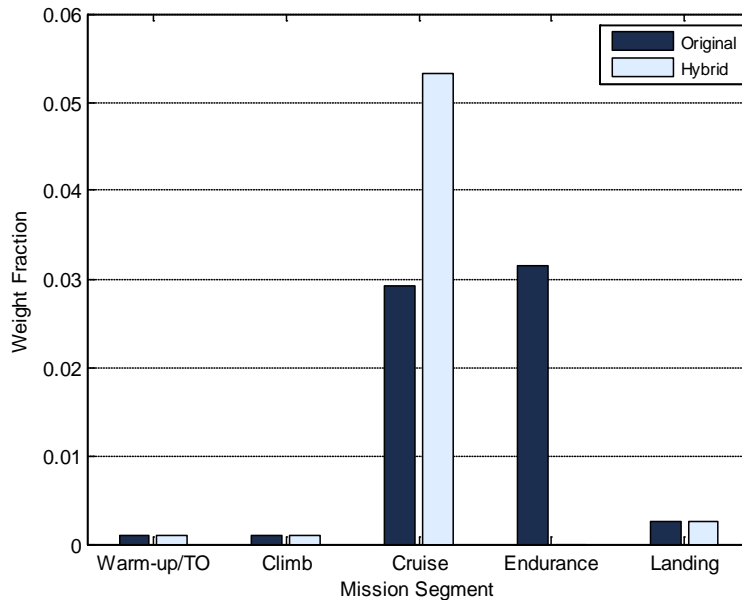


**Figure 36: Charge sustaining, centerline-thrust mission segment fuel weight fractions**

### 3.3.4 Comparison

The first two sets of results for the charge sustaining battery discharge strategy were very similar. The slight disparity in starting mechanism weight and mechanical efficiency led to small differences in engine power and payload capacity. The electric-start model had a smaller ICE, but a larger overall propulsion system weight due to its relatively heavy starter. The fuel and battery requirements for the two single propeller designs were identical. The centerline-thrust configuration deviated from the other designs when power generation was required. The inefficiency of sending power through a second propeller and the drag induced by that same action caused a dramatic increase in ICE size and corresponding fuel consumption. The advantage of improved propeller and mechanical efficiencies were completely overcome by the inefficiency of the power generation process. The dual propeller design provided the worst fuel consumption while allowing the smallest payload (0.407 kg). In fact, none of the designs met the required

payload of 2.27 kg. The clutch-start model provided the best alternative with a payload of 1.225 kg. By reducing the empty weight fraction from 87% to 79%, the payload requirement could be met. Sections 4 and 5 of this chapter disclose potential methods to meet this goal.

**Table 10: Propulsion system component specifications**

**Charge Sustaining:**

<i>Hybrid Type</i>	$P_{ICE}$ (W)	$P_{EM}$ (W)	$C_{BATTERY}$ (Wh)	$m_{ICE}$ (kg)	$m_{EM}$ (kg)	$m_{BATTERY}$ (kg)	$m_{PAY}$ (kg)	$m_{FUEL}$ (kg)	$m_{EMPTY}$ (kg)	$W_e$
Clutch-Start	584.9	155.2	652.8	0.474	0.047	3.730	1.225	0.554	11.82	0.87
Electric-Start	572.9	155.2	652.8	0.465	0.047	3.730	1.084	0.554	11.96	0.88
Centerline-Thrust	832.0	155.2	652.8	0.675	0.047	3.730	0.407	0.830	12.36	0.91

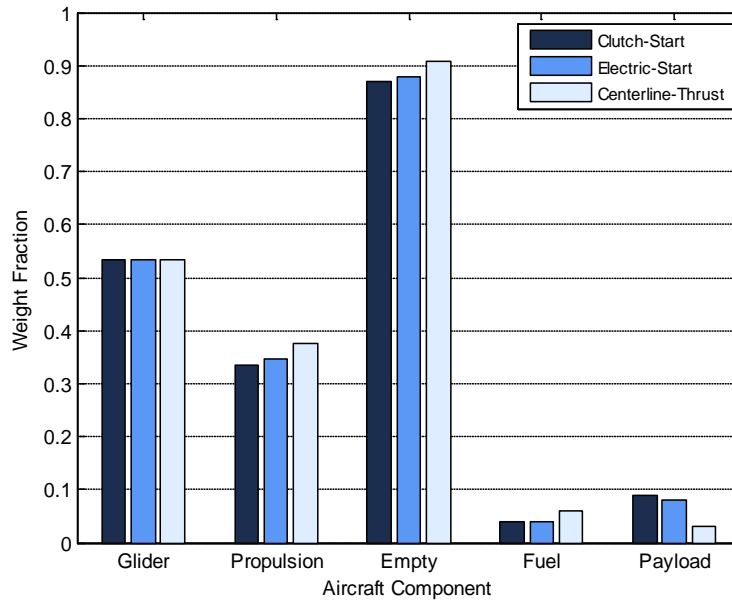


**Figure 37: Charge sustaining aircraft component weight fraction comparison**

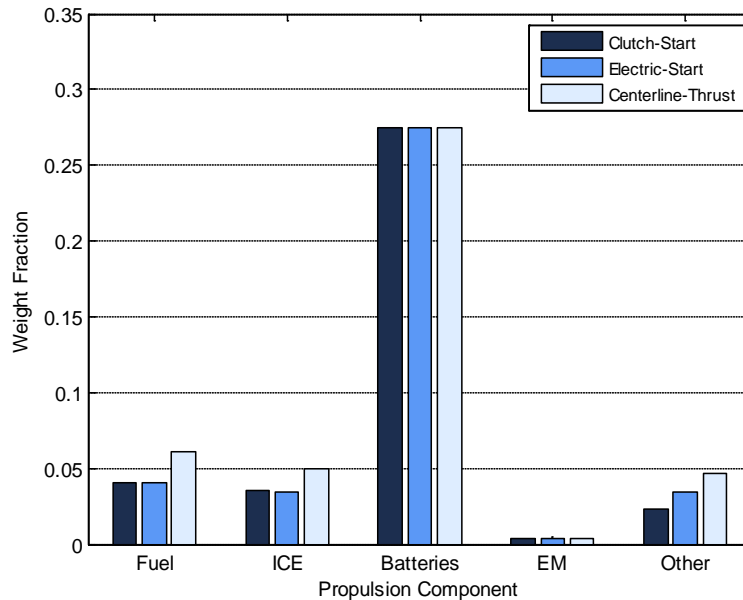


**Figure 38: Charge sustaining propulsion component weight fraction comparison**

### 3.4. Charge Sustaining with Segmented ISR Loiter Strategy

The charge sustaining model enabled the aircraft to carry a greater payload than the charge depletion model by reducing the battery weight fraction. By segmenting the required three hour ISR loiter time into smaller pieces and allowing a recharging cycle in between those segments, the battery pack weight would be reduced dramatically further. The goal of this strategy is to achieve the established payload requirements through a reduced battery pack weight and providing the same stealthy ISR mission length, albeit in a discontinuous fashion. Each of the three designs added two recharging cycles to the required mission profile, which created three separate loiter periods.

### **3.4.1 Clutch-Start Configuration**

The following three figures (Figs. 39 through 41) present the weight fraction results for the clutch-start configuration with the charge sustaining, segmented ISR loiter approach. The shortened battery-power only time tremendously diminished the empty weight fraction of the aircraft to 71% compared to 87% during the non-segmented mission. This hybrid design was the only one of nine within single digit percentage points of the original aircraft's empty weight fraction. The battery weight fraction decreased from 27% to 11% by segmenting the endurance time. For the first time, the hybrid design met the payload requirement by carrying 2.655 kg.

The overall mission length extended from five to seven hours due to two one hour long recharging cycles. As a result of the extra ICE power for battery charging, the fuel burn increased for the first time above that required by the original UAS. As shown by Fig. 41, the segmented mission caused the aircraft to burn fuel during the endurance phase while the previous strategies did not. While the aircraft could feasibly be traveling to separate locations during recharging, the fuel burned during this phase was included with the endurance segment. The aircraft flew at the endurance speed rather than the cruise speed while recharging to maximize the charging power available from the ICE to transfer to the generator.

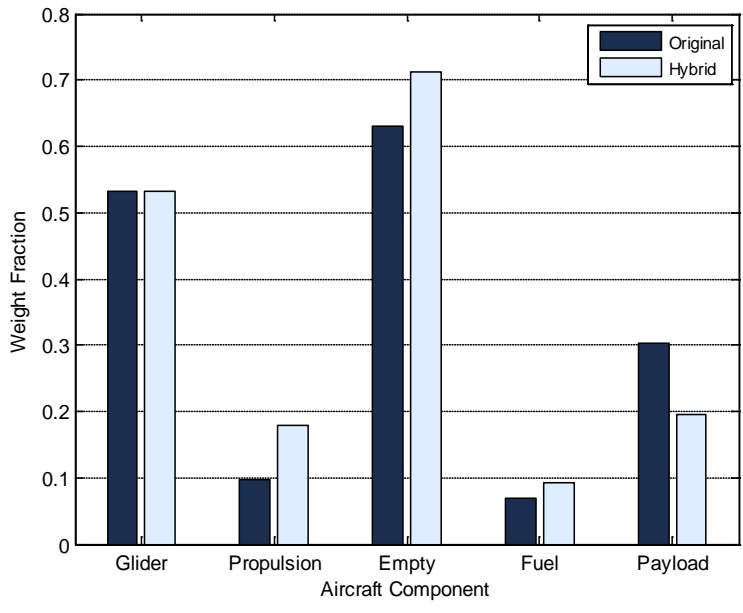


**Figure 39: Segmented loiter, clutch-start aircraft component weight fraction**

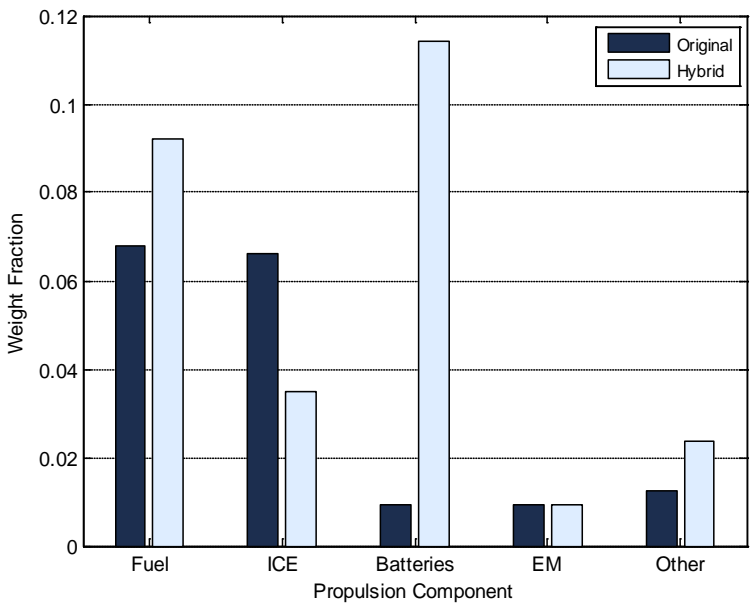


**Figure 40: Segmented loiter, clutch-start propulsion component weight fractions**

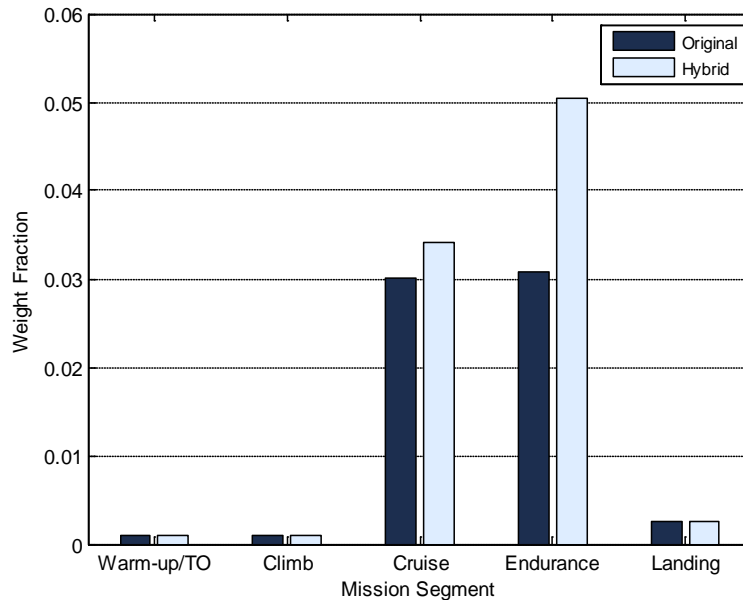


**Figure 41: Segmented loiter, clutch-start mission segment fuel weight fraction**

### 3.4.2 Electric-Start Configuration

Figures 42 through 44 show that the results for the electric-start configuration were once again similar to the clutch-start configuration. The empty weight fraction decreased to 72% from 88% thanks to a 58% reduction in battery weight. Like the previous design, the hybrid design met the payload requirement by carrying 2.514 kg. The overall mission length was also extended from five to seven hours due to two one hour long recharging cycles. The fuel burn increased 36% (0.330 kg) above that used by the original UAS and 121% (0.687 kg) above the non-segmented charge sustaining strategy.

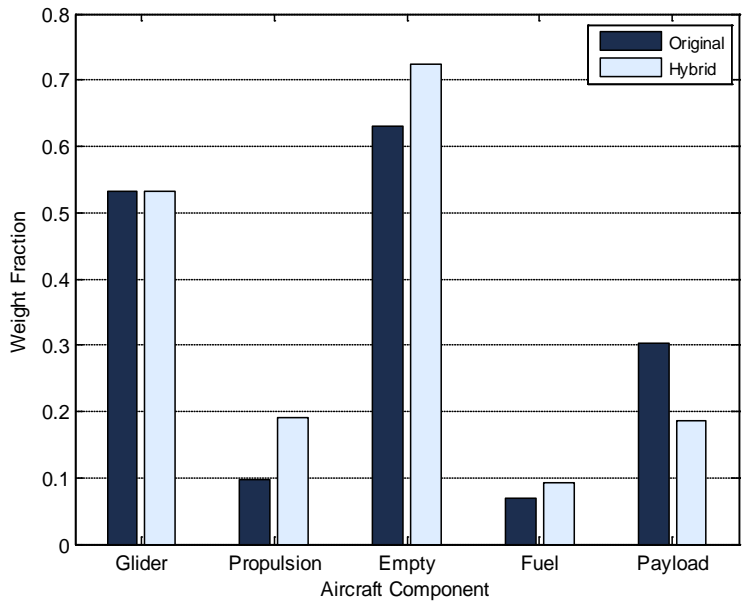


**Figure 42: Segmented loiter, electric-start aircraft component weight fractions**

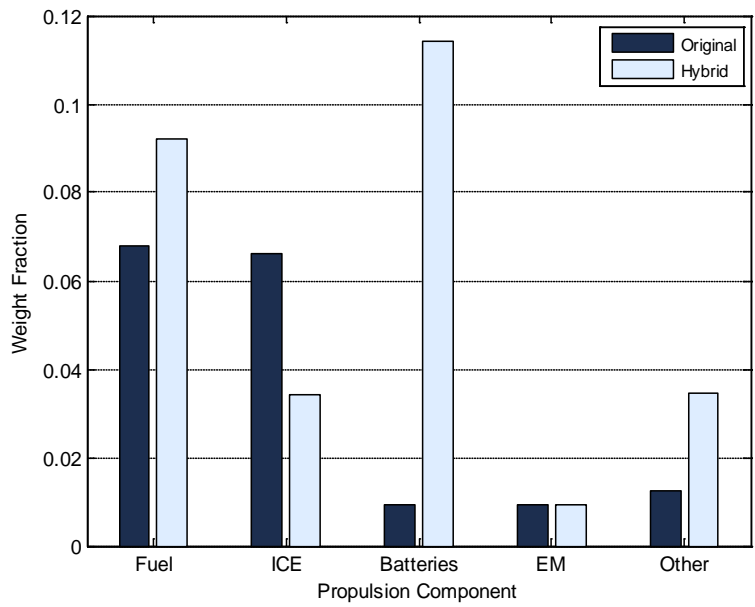


**Figure 43: Segmented loiter, electric-start propulsion component weight fractions**

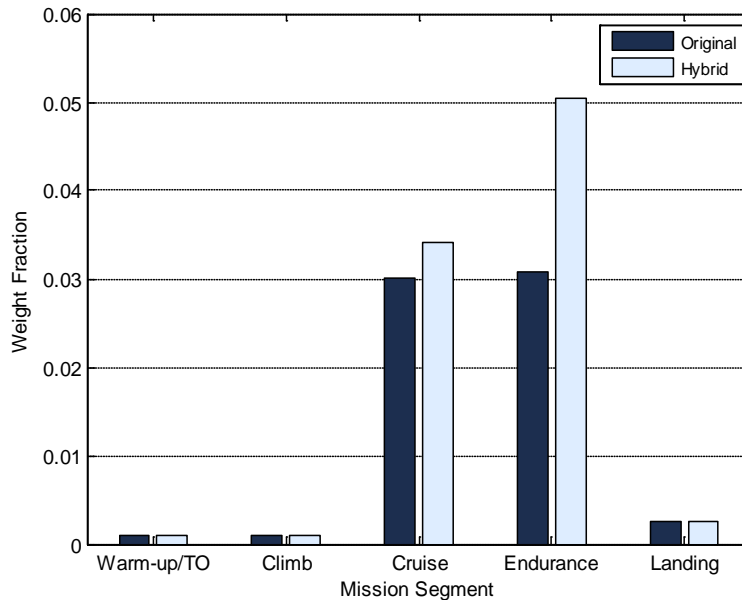


**Figure 44: Segmented loiter, electric-start mission segment fuel weight fractions**

### 3.4.2 Centerline-Thrust Configuration

As with the charge sustaining strategy, the results shown in Figs. 45 through 47 for the centerline-thrust configuration reinforce its stigma of poor charging performance. The segmented loiter concept was able to reduce the aircraft's battery pack weight, but with a relatively enormous fuel consumption. This configuration was the only one of the nine to possess a fuel weight in excess of its battery weight. The inefficient charging methodology also caused the recharging time to last 128 minutes for a total mission time of 9 hours and 16 minutes. The payload was improved over the non-segmented charge sustaining hybrid, but still did not meet the requirement.

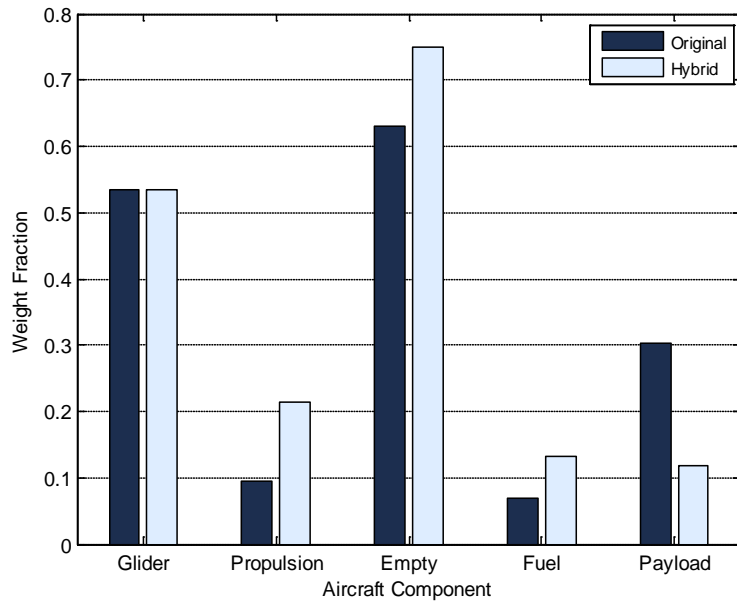


**Figure 45: Segmented loiter, centerline-thrust aircraft component weight fractions**

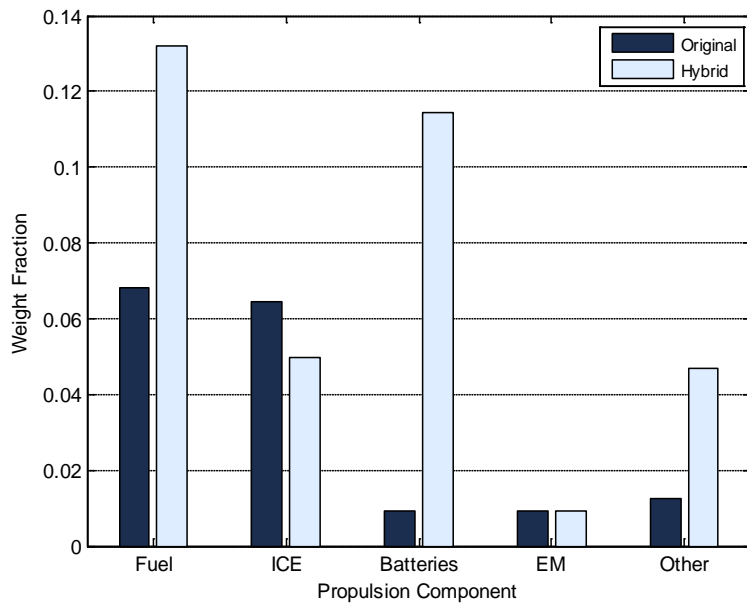


**Figure 46: Segmented loiter, centerline-thrust propulsion component weight fractions**

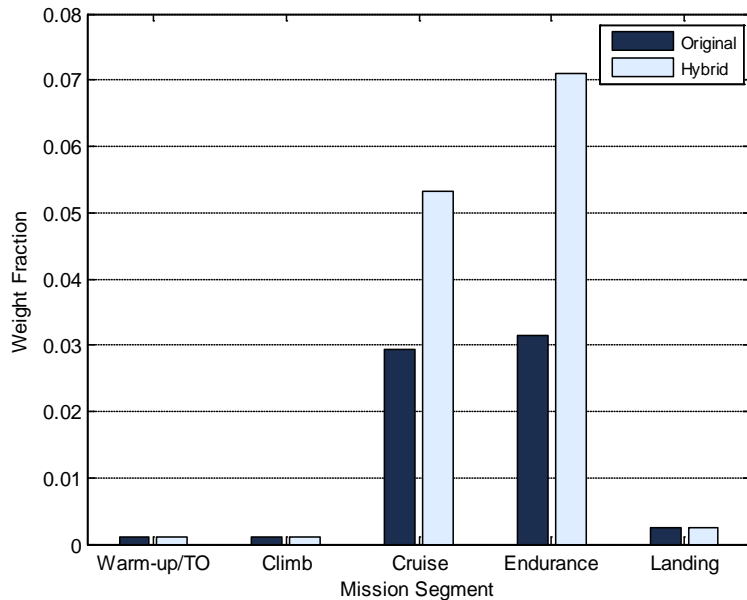


**Figure 47: Segmented loiter, centerline-thrust mission segment fuel weight fractions**

### 3.4.2 Comparison

As previously stated, the weight fraction results of the clutch and electric-start configurations were very similar as shown by Tables 11 and 12 and Figs. 48 and 49. The differences in mechanical properties led to the clutch-start design having the superior payload capacity for the same fuel expenditure. Each of the two models far exceeded the performance of the centerline-thrust model. The centerline-thrust design was the only of the three that failed to meet the required payload capacity and burned 0.539 kg more fuel. The EM for the centerline-thrust configuration was the smallest since it was sized for the maximum charging capacity of the aircraft. The wind milling propeller caused the ICE to provide an additional 278 W just to maintain cruise speed; only a fraction of that power was transferred to the batteries through the generator.

**Table 11: Propulsion system component specifications**

**Charge Sustaining with Segmented ISR Loiter:**

<i>Hybrid Type</i>	$P_{ICE}$ (W)	$P_{EM}$ (W)	$C_{BATTERY}$ (Wh)	$m_{ICE}$ (kg)	$m_{EM}$ (kg)	$m_{BATTERY}$ (kg)	$m_{PAY}$ (kg)	$m_{FUEL}$ (kg)	$m_{EMPTY}$ (kg)	$W_e$
Clutch-Start	584.9	307.0	272.0	0.474	0.093	1.554	2.655	1.254	9.69	0.71
Electric-Start	572.9	307.0	272.0	0.465	0.093	1.554	2.514	1.254	9.83	0.72
Centerline-Thrust	832.0	162.7	272.0	0.675	0.049	1.554	1.617	1.793	10.19	0.75

**Table 12: Loiter charging statistics**

<i>Hybrid Type</i>	<i>Recharging Cycles</i>	<i>Recharge Time (min)</i>	<i>Primary Loiter Time (min)</i>	<i>Secondary Loiter Time (min)</i>	<i>Total Mission Length (hr)</i>	<i>Fuel Increase (kg)</i>	<i>Battery Reduction (kg)</i>
Clutch-Start	2	60.0	75.0	52.5	7.00	0.687	2.18
Electric-Start	2	60.0	75.0	52.5	7.00	0.687	2.18
Centerline-Thrust	2	127.8	75.0	52.5	9.26	0.965	2.18

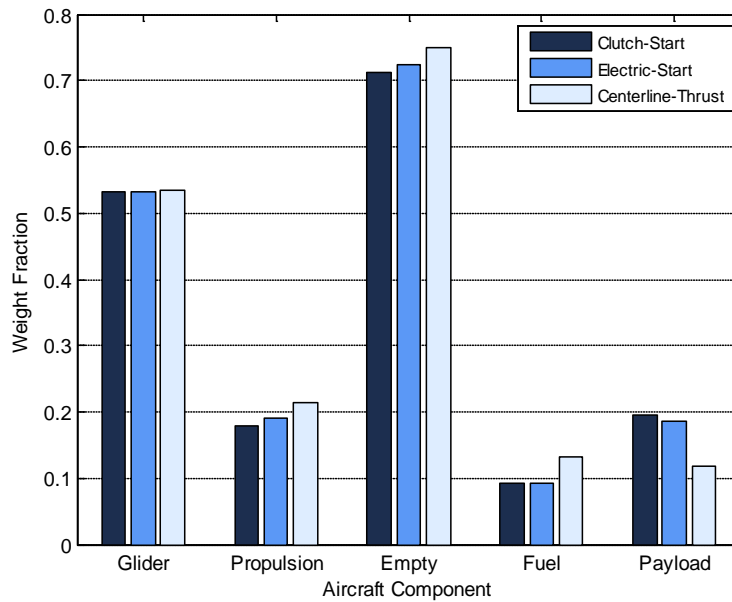


**Figure 48: Segmented loiter aircraft component weight fraction comparison**

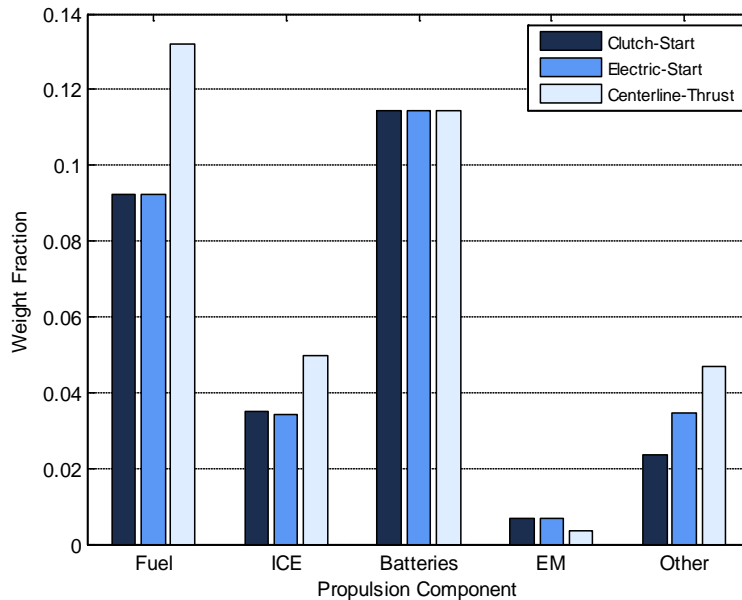


**Figure 49: Segmented loiter propulsion component weight fraction comparison**

### 3.5. Notional Designs for Baseline Mission

The previous sections showed that the clutch-start hybrid configuration outperformed the competition for each charging strategy during the MATLAB simulations. This section outlines three notional propulsion systems using commercial-off-the-shelf (COTS) products for the preceding results. Rather than producing three very similar clutch-start designs, the author chose to incorporate each of the three configurations to highlight their unique or intangible attributes that may not have been highlighted by the mathematical models within the simulation.

#### 3.5.1 Charge Depletion Strategy

The centerline-thrust model performed poorly in both charging strategies and displayed the lowest payload capacity during the charge depletion strategy where

charging was eliminated. Despite performance failures of the design during the simulations, the centerline-thrust configuration possesses unprecedented qualities like survivability that were not necessarily captured by the mathematical models. Therefore, the centerline-thrust configuration was chosen as the hybrid design of choice for the charge depletion strategy, avoiding its severe electric power generation handicap.

The COTS products chosen for the design are listed in Table 13. The first component, Enya's 0.7 hp *41-4CD* diesel engine, was selected to meet the DoD's heavy fuel requirement while meeting the calculated power required (Table 14).<sup>62</sup> Next, the NEU *1240-975* outrunner motor rated at 300 W continuous and 550 W surge power was mated to nine *Amicell* 23,000 mAh lithium-ion polymer batteries manufactured by Amit Industries Ltd.<sup>69, 70</sup> The cells would be aligned in a 3x3 series-parallel configuration to provide 69 Ah at 11.1 V. AeroNaut folding, carbon fiber propellers of the 14x7 and 14x9 inch variety were matched to the motor and engine based on recommended sizes by the ICE and EM manufacturers and to optimize for endurance and cruise speeds respectively. Finally, the electric-start design utilizes a *FEMA On-Board Starter* to provide the desired "air-start" capability.<sup>53</sup>

The manufacturers' advertised specifications are compared to those calculated within MATLAB in Table 14. Each component was oversized based on the calculations to compensate for manufacturers' tendencies to inflate their advertised numbers. The payload weight of the UAS increased 0.766 kg to 1.414 kg because the *Amicell* specific energy was much higher than the conservative estimate used in the simulation. The battery weight reduction enabled the empty weight of the aircraft to improve from 92% to 86% of the maximum takeoff weight.

**Table 13: Notional COTS components for charge depletion strategy**

<i>Component</i>	<i>Manufacturer</i>	<i>Model</i>	<i>Features</i>
Engine	Enya	41-4CD	0.7 hp, .40 in <sup>3</sup> , diesel
Motor	NEU	1240-975	300W cont, 550W surge
Battery	Amicell	Li-Po 23,000 mAh	3.7 V, 230 Wh/kg, 9 cells
Propellers	AeroNaut	14x7,14x9	folding, carbon fiber
Starter	FEMA	On-Board Starter	0.40 in <sup>3</sup> engines or larger

**Table 14: Notional charge depletion, centerline-thrust component specifications**

<i>Specification</i>	<i>Calculated Spec</i>	<i>COTS Solution</i>	<i>Advertised Spec</i>
$P_{ICE} (W)$	406.5	Enya Diesel 41-4CD	522.0
$m_{ICE} (kg)$	0.330		0.420
$P_{EM} (W)$	155.2	NEU 1240-975	300.0
$m_{EM} (kg)$	0.047		0.040
$C_{BATTERY} (Wh)$	731.3	AmiCell 23,000mAh (x9)	279.7
$m_{BATTERY} (kg)$	4.179		3.330
$m_{PAY} (kg)$	0.648		1.414
$m_{EMPTY} (kg)$	12.47		11.70
$W_e$	0.92		0.86

### 3.5.2 Charge Sustaining Strategy

The clutch-start configuration was selected for the charge sustaining strategy to best represent the ideal solution to the mission requirements. The clutch-start design was the top performer in each category and the charge sustaining strategy was the closest to meeting the requirements without segmenting the required endurance time. By improving the propulsive technologies or the aerodynamic design, the clutch-start, charge sustaining combination could one day meet the payload requirements. The notional COTS components based upon the simulation results follow in Tables 15 and 16.

The engine selected was greatly oversized for the calculated ICE power requirement. Competition R/C gas engine manufacturer BME has converted a 0.60 in<sup>3</sup> SuperTigre glow fuel engine to a pump-carbureted gasoline powered engine with electronic ignition. The engine supposedly maintains the SuperTigre’s 2.5 hp power rating with a negligible increase in weight.<sup>65,71</sup> The NEU motor used for charge depletion was selected again for the charge sustaining strategy. Nine 20,000 mAh Amicell Li-Po cells were chosen for a 3x3 series-parallel connection to provide 60 Ah at 11.1 V. The propeller was a Graupner CAM 14x6 inch rigid model. Finally, the clutch was chosen as a 1.0 Nm dynamic, 1.5 Nm static electro-magnetic device from RM Hoffman.

The weight savings of the *Amicell* batteries more than compensates for the additional weight of the oversized engine. The payload capacity increased to 1.804 kg, which does not meet the required 2.27 kg, but would be able to carry the *Alticam 400 Series* camera used by the *ScanEagle* and the *Kestrel Autopilot*. Ultimately, the design is close to the requirements and reduced the calculated empty weight fraction to 83%.

**Table 15: Notional COTS components for charge sustaining strategy**

<i>Component</i>	<i>Manufacturer</i>	<i>Model</i>	<i>Features</i>
Engine	BME/SuperTigre	0.90ci	2.5 hp, 0.60 in <sup>3</sup> , gas conversion
Motor	NEU	1240-975	300 W cont, 550 W surge
Battery	Amicell	Li-Po 20,000 mAh	3.7 V, 228 Wh/kg, 9 cells
Propeller	Graupner	CAM 14x6	rigid
Clutch	RM Hoffman	-	1.0 Nm Dynamic, 1.5 Nm Static

**Table 16: Notional charge sustaining, clutch-start component specifications**

<i>Specification</i>	<i>Calculated Spec</i>	<i>COTS Solution</i>	<i>Advertised Spec</i>
$P_{ICE} (W)$	584.9	BME 0.90ci	1864.0
$m_{ICE} (kg)$	0.474		0.737
$P_{EM} (W)$	155.2	NEU 1240-975	300.0
$m_{EM} (kg)$	0.047		0.040
$C_{BATTERY} (Wh)$	652.8	AmiCell 20,000mAh (x9)	666.0
$m_{BATTERY} (kg)$	3.730		2.925
$m_{PAY} (kg)$	1.225		1.804
$m_{EMPTY} (kg)$	11.82		11.27
$W_e$	0.87		0.83

### 3.5.3 Charge Sustaining with Segmented ISR Loiter Strategy

Arguably, the clutch-start configuration should be used regardless of the battery discharging strategy. However, the electric-start configuration model was chosen for the segmented ISR loiter strategy based upon the theory that an electric starter could be more reliable than a clutch as it would be decoupled from the driveshaft. A more reliable starting solution would be preferable since it would have to be utilized more often in this strategy. Additionally, both the clutch and electric-start designs easily met the payload requirements under this strategy so either design would be acceptable.

The BME 0.90ci engine was also used for the segmented charge sustaining strategy. The larger power generation requirement called for a different electric motor. The Hacker *A30-10XL* was chosen for its advertised 650W peak capacity and estimated continuous power of 373 W. Over-sizing the motor could potentially improve the charging time of the batteries while providing additional thrust capability. Six 12,600 mAh *Amicell* Li-Po batteries were selected for a 3x2 series-parallel combination. The

battery pack combination would provide 25.2 Ah at 11.1 V. The systems would use the FEMA starter and Graupner CAM 14x6 propeller used on the previous design.

The selected components were able to meet the payload requirement while providing a substantial increase in power. The payload capacity slightly decreased by 64 grams, but the power rating of the engine tripled while the peak power of the motor doubled. The excess power could enable the aircraft to fly above the specified 13.6 kg takeoff weight and/or fly at greater speeds.

**Table 17: Notional COTS components for segmented loiter strategy**

<i>Component</i>	<i>Manufacturer</i>	<i>Model</i>	<i>Features</i>
Engine	BME/SuperTigre	0.90ci	2.5 hp, .60 in <sup>3</sup> , gas conversion
Motor	Hacker	A30-10XL	650 W peak, 900 k/V
Battery	Amicell	Li-Po 12,600 mAh	3.7 V, 222 Wh/kg, 6 cells
Propeller	Graupner	CAM 14x6	rigid
Starter	FEMA	On-Board Starter	0.40 in <sup>3</sup> engines or larger

**Table 18: Notional segmented loiter, electric-start component specifications**

<i>Specification</i>	<i>Calculated Spec</i>	<i>COTS Solution</i>	<i>Advertised Spec</i>
$P_{ICE} (W)$	572.9	BME 0.90ci	1864.0
$m_{ICE} (kg)$	0.465		0.737
$P_{EM} (W)$	307.0	Hacker A30-10XL	373 (est)
$m_{EM} (kg)$	0.093		0.179
$C_{BATTERY} (Wh)$	272.0	AmiCell 12,600mAh (x6)	279.7
$m_{BATTERY} (kg)$	1.554		1.260
$m_{PAY} (kg)$	2.514		2.450
$m_{EMPTY} (kg)$	9.83		9.89
$We$	0.72		0.73

The preceding six tables outlined potential propulsion system designs for the baseline mission and original set of input variables. In order to proceed to advanced designs based on alternative missions, an analysis must be performed on the data to determine the best forward course of action. The next section outlines one method of breaking down the impact of changing an individual variable.

#### **4. Sensitivity Analysis**

The overwhelming number of input variables required some method to determine which inputs were the most critical to the final performance of the aircraft. In this case, the performance criterion was selected to be the payload mass of the hybrid-electric UAS design. Previously, the cost function was set to minimize power required during endurance, which in turn minimized the mass of the battery pack. Since the payload mass was the limiting factor during the baseline mission, a sensitivity analysis provides a method to systematically increase the payload capacity. Additionally, the payload is susceptible to a broader range of variables than the battery mass. Simple logic and a quick analysis of the underlying equations easily identifies how certain input values could be changed to improve payload capacity. However, nonlinear effects require a detailed sensitivity analysis to determine the degree to which each input could change the final outcome.

The method utilized for this analysis was adapted from Mattingly, et al.<sup>48</sup> By slightly changing any of the input variables, a designer may determine which of the inputs has the greatest influence on the final solution ( $m_{payload}$ ). The parameter,  $Q$ , which generates the largest absolute slope from Eq. 46 would therefore be the most sensitive. By only slightly (<3%) adjusting each parameter, the sensitivity analysis should avoid

second order effects and point towards a local minimum. A larger change could feasibly include higher order effects such as a rapid increase or decrease in slope.

$$\frac{(m_1 - m_2)/m_2}{(Q_2 - Q_1)/Q_1} = \frac{\delta m}{\delta Q} \quad (46)$$

The results of the sensitivity analysis are shown in Table 19 for the clutch-start hybrid configuration with a charge sustaining battery discharge strategy. The data are specific to this design but are reflective of all nine variations. The table depicts the relative sensitivity of each variable in descending order based upon the absolute value of the slope. A positive slope indicates that increasing the variable value would improve the payload capacity; just as decreasing a variable with a negative slope would also improve the payload.

By this logic, the most sensitive variable was the maximum lift coefficient. By finding wing cross-sections with greater lift coefficients or adding high lift devices like flaps, the payload capacity could be dramatically improved. Obviously, decreasing the endurance time would also boost the payload by reducing the battery mass. Clearly, other variables like zero lift drag, EM efficiency and propeller efficiency have a strong effect. However, these three variables are likely already near their peak performance potential. Perhaps the most practical means of enhancing the payload capability would be to further investigate advanced battery technologies like lithium-sulfur.

The negative values for ICE power to weight ratio ( $P/W_{ICE}$ ) and cruise speed propeller efficiency ( $\eta_{prop,cruise}$ ) are counter to logical expectations. Upon further examination, it was determined that the values are correct for the system of equations used to calculate the payload. In reality, increasing each value would provide improved payload capacity. The magnitude of the slope would remain the same, but the direction

would be reversed (positive slope). The findings from this simple study facilitated the additional designs portrayed in the subsequent section.

**Table 19: Payload mass sensitivity analysis**

Initial Payload Mass (kg) = 1.2247

<i>Parameter</i>	<i>Units</i>	<i>Initial</i>	<i>New</i>	$\Delta$	<i>Normalized</i> $\Delta$	$m_{payload}$ (kg)	$\Delta W_f$	<i>Slope</i>
$C_{L,max}$	-	1.25	1.24	-0.010	-0.008	1.1837	-3.1685	5.1
$E_e$	Wh/kg	175	172	-3.000	-0.017	1.1596	-3.1926	3.8
$t_{endure}$	s	10800	10500	-300.00	-0.028	1.3283	-3.0239	-3.7
$\eta_{prop, endure}$	-	0.80	0.79	-0.010	-0.013	1.1845	-3.1677	3.2
$\eta_{EM}$	-	0.85	0.84	-0.010	-0.012	1.1874	-3.1648	3.2
$C_{D,O}$	-	0.036	0.035	-0.001	-0.028	1.3108	-3.0414	-3.1
$W/S$	N/m <sup>2</sup>	90	89	-1.000	-0.011	1.2467	-3.1055	-2.0
$V_{cruise}$	m/s	20.5	20.0	-0.500	-0.024	1.2719	-3.0803	-1.9
$m_{TO}$	kg	13.6	13.5	-0.100	-0.007	1.2110	-3.1412	1.9
$V_{stall} - V_{endure, theo}$	m/s	2.57	2.52	-0.050	-0.019	1.1998	-3.1524	1.3
$V_{endure, act} - V_{stall}$	m/s	2.57	2.52	-0.050	-0.019	1.2428	-3.1094	-0.9
$t_{cruise}$	s	3600	3500	-100.00	-0.028	1.2381	-3.1141	-0.5
$P_{payload}$	W	25	24.5	-0.500	-0.020	1.2343	-3.1179	-0.5
$SFC_{cruise}$	N/Ws	1.658E-06	1.650E-06	0.000	-0.005	1.2269	-3.1253	-0.5
$\eta_{mech}$	-	0.95	0.94	-0.010	-0.011	1.2197	-3.1325	0.5
$P/W_{ICE}$	W/kg	1233	1200	-33.000	-0.027	1.2364	-3.1158	-0.4
$h_{TO}$	m	1500	1475	-25.000	-0.017	1.2310	-3.1212	-0.4
$m_{clutch}$	kg	0.15	0.148	-0.002	-0.013	1.2267	-3.1255	-0.2
$\eta_{gen}$	-	0.75	0.74	-0.010	-0.013	1.2228	-3.1294	0.1
$\eta_{prop, cruise}$	-	0.78	0.77	-0.010	-0.013	1.2258	-3.1264	-0.1
$P/W_{EM}$	W/kg	3288	3200	-88.000	-0.027	1.2234	-3.1288	0.0
$ROC$	m/s	2.032	2.000	-0.032	-0.016	1.2246	-3.1276	0.0
$e$	-	0.85	0.84	-0.010	-0.012	1.2247	-3.1275	0.0

## 5. Advanced Mission Analysis

The results of the sensitivity analysis provided a means to investigate different options for improving the UAS's performance. At this point, the focus remained on the clutch-start, charge-sustaining configuration as the most practical option. The aircraft, as specified by the input parameters designated in Section 2 of this chapter, was able to

carry the required payload of 2.27 kg (or 5 lbf) if the endurance time was reduced to 2 hours and 9 minutes. By slightly improving the maximum lift coefficient from 1.25 to 1.30, the endurance time would extend 8 minutes to 2 hours and 17 minutes. By achieving small gains in a number of areas, the craft might be able to achieve the requested 3 hour endurance time.

Even though the improved lift coefficient was only a 4% increase, the possibility of such a gain is less likely than achieving improvements in battery capacity. By setting the specific energy to 225 Wh/kg as advertised by Amit Industries and LG, the endurance time for a 5 lbf payload capacity improves to 2 hours and 46 minutes. Better still, by using Sion Power's Li-S batteries with an alleged 300 Wh/kg, the UAS would far exceed the requirement by flying on electric power for 3 hours and 42 minutes. The Li-S batteries showed the potential to lengthen the endurance time by a tremendous 93 minutes over the original results. Clearly, the most advantageous improvement area was the battery technology. As a general rule of thumb, each improvement of 25 Wh/kg in battery specific energy elongated the endurance time by 18 minutes for the single propeller charge sustaining designs.

The most immediate application for the lithium-sulfur batteries would be the charge depletion strategy. The largest drawback to the chemistry is relatively poor cycle durability. By eliminating the recharging aspect of the mission, the number of charging cycles applied to the battery pack would drastically decrease. The batteries could be charged on the ground using a dedicated charging system that would likely not be appropriate for mid-air charging. In effect, the aircraft would be designed with primary batteries in mind. The Li-S batteries or actual primary batteries could be rapidly replaced

on the ground by maintenance crews for quick sortie turnaround times. Using Li-S or similar primary batteries with a specific energy of 300 Wh/kg would improve the centerline-thrust, charge depletion model's endurance time by approximately 88 minutes to 3 hours and 10 minutes. Using these batteries definitely strengthened the case for using the centerline-thrust model. Until these improved batteries are available, the segmented charge sustaining model provides the greatest performance per battery mass.

Until this point, the defined ISR mission was to provide three hours of counter-IED surveillance. The segmented strategy would be the ideal candidate if the ISR mission was to provide a series of images rather than continuous video footage. The UAS would be able to travel great distances while charging, and then switch to the stealthy all-electric mode to photograph select targets. For example, one such mission is proposed in Table 20 for the clutch-start hybrid configuration. After a catapult launch from a safe location, the UAS would cruise for three hours to its first target and have about 31 minutes to provide still photography or video surveillance to the home base. Next, the UAS would recharge its battery pack while cruising for an hour to its second target with 22 minutes of battery power available. The process would repeat three more times for five total ISR targets. Finally, the UAS would cruise home for three more hours. The process might also be useful for taking chemical or biological agent readings over a large, contested area. Either way, the UAS would be able to fly for over 12 hours while providing 2.55 kg (5.62 lbf) of payload capacity.

**Table 20: Proposed segmented ISR mission profile**

<i>Number</i>	<i>Segment</i>	<i>Time (min)</i>
1	TO/Climb	2.5
2	Cruise Out	180
3	ISR Loiter #1	31.6
4	Cruise-Charge	60
5	ISR Loiter #2	22.1
6	Cruise-Charge	60
7	ISR Loiter #3	22.1
8	Cruise-Charge	60
9	ISR Loiter #4	22.1
10	Cruise-Charge	60
11	ISR Loiter #5	22.1
12	Return Cruise	180
13	Approach/Land	2.5

The segmented ISR strategy provides unprecedented flexibility to combatant commanders. A single aircraft could be set up for both the segmented and non-segmented charge sustaining missions by over-sizing the engine and motor. Depending on the day's Air Tasking Order (ATO) requirements, the UAS maintenance crew can add and subtract battery cells as needed. Larger battery packs would be needed for sustained ISR surveillance, while smaller packs could be supplemented for segmented missions allowing a greater fuel capacity. Certainly, the charge sustaining strategies enable versatility and flexibility never before seen in the combat theater.

## V. Conclusions and Recommendations

### 1. Conclusions of Research

The United States military needs more efficient, stealthy propulsion technology for its small unmanned aircraft systems fleet. Hybrid-electric technology combining the intrinsic capabilities of gasoline powered internal combustion engines with nearly silent battery powered motors would meet that need. This research effort sought to determine the most appropriate means of combining the two propulsion energy sources for a small UAS.

This effort focused on three variations of a parallel hybrid-electric propulsion system design for a small UAS. Three distinct battery discharge strategies were proposed for each hybrid configuration for a total of nine unique designs. Three objectives were set to analyze that set of propulsion system designs.

The initial goal was to validate and expand an existing UAS hybrid-electric propulsion system design code created by Harmon.<sup>28,44</sup> The original MATLAB code analyzed a clutch-start hybrid design with a charge sustaining battery discharge strategy. The objective was achieved by re-deriving the fundamental equations within the code and broadening their application to the intricacies of the eight other designs. The resulting code remained sufficiently flexible so that it might be easily expanded for future designs or mission requirements. The final product may be viewed in its entirety in Appendix C, while a comprehensive list of the equations is shown in Appendix A.

With the updated design code in hand, the nine unique hybrid-electric system designs were optimized and compared to determine the most suitable design for a typical ISR mission. The proposed mission consisted of a catapult takeoff from an elevation of

1500 m MSL, followed by a 300 m climb, a one-hour cruise, a three-hour endurance loiter and a one-hour return cruise. In all cases, the clutch-start hybrid led the competition in payload capacity. In both charge sustaining strategies, the design also consumed the least amount of fuel. The centerline-thrust design showed a slight fuel consumption advantage during charge depletion missions thanks to its greater propeller efficiency.

The final objective of the effort was to determine which types of missions would be best suited for each design. A summary of the recommended missions is shown below in Table 21. The clutch-start design should be the primary choice for all missions when in-flight battery recharging is required. If the electromagnetic clutch proves to be unreliable during testing, the electric-start design could replace the clutch-start as the primary choice despite a small weight penalty.

**Table 21: Recommended mission summary**

	<i>Hybrid Type</i>	<i>Battery Strategy</i>	<i>Mission Types</i>	<i>Comments</i>
1	Clutch-start	Depletion	Continuous loiter	Primary batteries
2	Electric-start	Depletion	Continuous loiter	Primary batteries
3	Centerline thrust	Depletion	High threat	Least fuel Most survivable
4	Clutch-start	Sustaining	Continuous loiter	Most suitable to proposed mission
5	Electric-start	Sustaining	Continuous loiter	Mechanically simpler option
6	Centerline thrust	Sustaining	Not recommended	Poor charging
7	Clutch-start	Segmented	Geographically separated targets	Largest payload
8	Electric-start	Segmented	Geographically separated targets	Largest payload
9	Centerline thrust	Segmented	Not recommended	Poor charging

The centerline-thrust design proved to have advantages during the charge depletion strategy comparison. None of the designs were able to meet the payload

requirements with the originally assumed battery capabilities. However, when using a primary battery or an advanced Li-S rechargeable battery, all three designs exceeded the payload capacity requirement. Because the centerline-thrust configuration possessed superior survivability and fuel efficiency, it was determined to be the best choice when implementing a charge depletion strategy. The clutch and electric-start designs provided an edge on payload capacity, but when considering all factors, the dual propeller design provided a distinct advantage.

If the mission includes a number of geographically separated ISR targets, the segmented charge sustaining strategy was the obvious choice. The limiting weight of the battery pack radically diminished when sizing the pack for a fraction of the endurance time and allowing it to recharge. The strategy provides a tremendous capability to travel long distances while charging and providing stealthy ISR coverage when and where desired.

Until reliable COTS Li-S batteries are readily available, the aircraft must accept a performance tradeoff. Segmenting the ISR mission to reduce the battery pack mass proved to be a more than capable compromise to meet or exceed all performance requirements. If segmenting the ISR loiter is unacceptable, the UAS will suffer either a reduced all-electric endurance time, payload capacity or a combination of both. The clutch-start, charge sustaining design provides a 90% solution to the requirements sought by the Army and could be built and tested today. The complete solution will arrive with the release of improved battery technology from companies like Sion Power in the near future. By the time the first hybrid-electric UAS prototype is built and flight-tested, the necessary batteries may be readily available to achieve a 100% solution.

## **2. Recommendations for Future Research**

The possibilities for future research in the hybrid-electric UAS arena are seemingly endless. The technology has the potential to revolutionize UAS operations in both the private and defense sectors. There are a number of realistic near-term projects and areas for improvement that could be broached by future students.

First and foremost, a better defined set of key performance parameters is needed to more accurately analyze the problem at hand. The requirements used in this project were from informal conversations with the Army's Maneuver Center of Excellence and observations of similarly sized existing aircraft. By involving organizations like Air Combat Command (ACC) or Air Force Special Operations Command (AFSOC), researchers might discover more appropriate mission profiles and payload requirements.

Using an updated or validated mission profile, dynamic models could better predict the performance of the system as a whole. New tools developed for SIMULINK, recently acquired by AFIT, allow relatively simple dynamic modeling of hybrid powertrains. Modeling performance maps for an engine with battery and motor models would help predict the behavior of a physical prototype. The dynamic models would provide more accurate estimations of fuel and electric power consumption than the static optimization process used in this effort. Additionally, missions including gliding, dynamic soaring and/or windmill descending could be analyzed to extend loiter durations.

Lessons learned from SIMULINK testing would assist in the designs of a controller. There are literally thousands of controllers available on the market for R/C engines and motors. However, the HEUAS requires a customized controller for the

entire hybrid system. The controller must meter fuel flow, shut down and restart the engine when necessary, apply the appropriate current and voltage to the motor and run the motor as a generator. None of the COTS R/C brushless motor controllers offered by the manufacturers surveyed by the author were able to run the motor as a generator.

Along with the mission requirements, many of the component performance specifications could use refinement. Many R/C component manufacturers are known for overinflating or simply estimating their advertised performance data. In order to provide more accurate static or dynamic models, individual component performance tests should be completed with a dynamometer. In addition, AFRL has been conducting experimentation on advanced small engine designs to improve efficiency.<sup>52</sup> These new engine technologies should ultimately be incorporated into the hybrid systems despite not being true COTS products.

Along with the engines, motors and batteries, reliable data on propeller efficiency were not readily available. The propeller models offered with the QPROP software were very limited. In order to achieve more precise performance data on propellers, the XFOIL software program could be used to develop supplementary propeller files to use in QPROP. Alternatively, the propellers could be tested in concert with the aforementioned dynamometer testing by adding a thrust measurement capability.

Several unanswered questions arose when selecting the propeller sizes for the notional baseline mission designs. Typically, R/C engine and motor manufacturers provide recommended propeller sizes for their products. These recommendations may not be applicable to the aircraft size proposed in this project. Aircraft between 30 to 40 lbf generally use propeller diameters in the 17 to 20 inch range. However, the hybrid

system design created a situation in which the final engine and motor sizes are much smaller than that of a conventionally powered UAS. The recommended propeller sizes for the resulting components were only 13 or 14 inches in diameter. Then uncertainties arise when determining whether the propeller should be selected based on the size of the aircraft or the propulsion components. Alternatively, the propeller could be chosen to best match the electric motor rather than the engine or vice versa. By compromising at a median diameter and pitch, the efficiencies of the engine and motor could be reduced. A new optimization formulation should be created to determine the optimum propeller size for a given hybrid-electric system.

Despite some questions about the legitimacy of the input parameters, the recommended components are more than sufficient to begin prototype testing. Each input parameter and hybrid configuration was thoroughly researched by the author, but time constraints prevented physical testing. The author recommends focusing on the clutch-start hybrid as the preferable design for testing as it outperformed its competition in every simulation.

There are several questions about the mechanical configuration that are not likely to be answered by mathematical simulations. First, the clutch-start design proposed by Harmon placed the EM and ICE on a single shaft separated by an electromagnetic clutch.<sup>28,44</sup> Testing may show that a belt drive and secondary clutch separating the EM from the ICE driveshaft may be preferable to simplify torque and speed matching issues. Second, testing will determine whether or not the inertia and friction of a free spinning motor during non-charging operation requires an inordinate amount of ICE power to overcome. If so, the clutch should be placed on a separate belt drive or a trickle charge

should always be pulled from the generator to benefit from the loss of mechanical power. Finally, single cylinder engines suffer from extreme torque ripple effects due to the varying force encountered with piston motion. Multi-cylinder engines are able to mitigate transient torque effects through proper engine timing. Some testing organizations have overcome some of the single cylinder effects by using torsionally flexible spider coupling devices. Studies have shown that adding strategically timed EM torque to the engine driveshaft can balance out the torque through the engine's cycle.<sup>73</sup> This procedure could prove advantageous to the proposed hybrid-electric systems and deserves recognition in the testing and controller design processes.

The dual-propeller centerline-thrust design does provide unique advantages for the charge depletion model. Further testing on the design could be performed in a wind tunnel to determine how effectively folding propellers might work during operation. Perhaps the folding propeller idea only works on paper. Given a fuselage design, the effects on the rear, pusher propeller from the front prop-wash and fuselage boundary layer interactions could also be studied. The performance degradation on the rear propeller might be too great to overcome and eliminate any advantages of the dual propeller design.

Ultimately, there are many avenues of investigation for hybrid-electric aircraft propulsion. The entire effort has focused on small unmanned aircraft systems using electric motors and internal combustion engines. Future battery or fuel cell technologies may completely eliminate the need for hybrid-electric propulsion for both aircraft and automobiles. Nevertheless, hybrid-electric technology provides the best solution to meet the advanced propulsion needs of today.

## Appendix A: MATLAB Code Equations

“HEUASdesign” Function:

$$SFC = \frac{1}{\eta_{ICE} Q_{LHV}}$$

$$h = h_{TO} + h_{AGL}$$

$$t_{climb} = \frac{h_{AGL}}{ROC}$$

$$P_{charge} = \frac{P_{payload}}{\eta_{generator}}$$

$$A = \frac{\pi}{4} (D_{prop}^2 - D_{fuselage}^2)$$

$$P_{windmill} = 1/2 C_p A V_{cruise}^3$$

$$P_{gen} = P_{payload} + P_{fcs} + P_{charge}$$

$$W = mg$$

“OptimizeUAS” Function:

$$P = \frac{P_{SL}}{1.132 \rho / \rho_{SL} - 0.132}$$

$$P_{EM} = \frac{P_{R,end}}{\eta_{prop} \eta_{EM} \eta_{mech}}$$

“SizeConstraint” Function:

$$V_{end} \leq V_{stall} - margin$$

$$V_{stall}^2 = \frac{2 \frac{W}{S}}{\rho C_{L,max}}$$

$$\sqrt{AR} = \frac{2 \frac{W}{S}}{\rho_{\infty} V_{end}^2} \sqrt{\frac{1}{3\pi e C_{D,0}}}$$

$$P_{ICE} = \frac{1}{\eta_{mech}} \left[ \frac{1}{\eta_{prop1}} \left( \frac{1}{2} \rho V_{cruise}^3 W C_{D,0} \frac{1}{W/S} + \frac{2W W/S}{\rho V_{cruise} \pi e AR} + P_{windmill} \right) + \frac{P_{gen}}{\eta_{gen} \eta_{prop1} \eta_{prop2}} \right]$$

“SizeCost” Function:

$$P_{R,end} = W \sqrt{\frac{2W}{\rho_{\infty} S} \frac{4C_{D,0}}{(3\pi e AR)^{3/4}}}$$

“PostProcess” Function:

$$S = \frac{W}{W/S}$$

$$b = \sqrt{S \cdot AR}$$

$$c = \frac{S}{b}$$

$$K = \frac{1}{\pi e AR}$$

$$\frac{C_L^{1.5}}{C_D} = \frac{(C_{D,0}/K)^{0.75}}{4C_{D,0}}$$

$$\frac{C_L}{C_D} = \frac{\sqrt{C_{D,0}/K}}{2C_{D,0}}$$

$$S.F. = V_{end,act} - V_{stall}$$

$$C_L = \frac{2W/S}{\rho V^2}$$

$$C_D = C_{D,0} + KC_L^2$$

$$P_R = \sqrt{\frac{2W^3 C_D^2}{\rho S C_L^3}}$$

$$P_{R,shaft} = \eta_{prop} P_R$$

$$P_{R,climb} = P_{R,S\&L} + ROC \cdot W \cdot C_D$$

$$P_{R,climb elec} = P_{R,climb} - P_{ICE}$$

$$P_{ICE,original} = MAX(P_{R,shaft}) + (P_{payload} + P_{fcs})/\eta_{gen}$$

$$C_{batt} = m_{batt} E$$

$$m_{EM} = \frac{P_{EM}}{g \left( \frac{P}{W} \right)_{EM}}$$

$$WF_{climb,original} = \exp \frac{-SFC \cdot \Delta h_e}{1 - 0.5 \rho V^2 S \frac{C_{D,0} + KC_{L,max}^2}{P_{R,climb}/V}}$$

$$R = Vt$$

$$WF_{cruise,original} = \exp \frac{-r \cdot SFC_{cruise}}{\eta_{prop} C_L/C_D}$$

$$WF_{endure,original} = \exp \frac{-SFC_{endure} V_{endure} t_{endure}}{\eta_{prop} C_L/C_D}$$

$$WF_{cruise} = \exp \frac{-r \cdot SFC_{cruise}}{\eta_{prop} C_L/C_D}$$

$$W_0 = W_{TO}$$

$$WF_{fuel} = 1.06 \left( 1 - \frac{W_x}{W_0} \right)$$

$$W_{pay} = W_0(1 - WF_{fuel} - WF_{empty})$$

$$m_{empty} = m_{TO} - m_{fuel} - m_{payload}$$

$$m_{propulsion} = m_{ICE} + m_{EM} + m_{batt} + m_{prop} + m_{start}$$

$$m_{glider} = m_{empty} - m_{propulsion}$$

### Configuration Unique Equations:

Charge Depletion Strategy:

$$P_{EM} = \frac{P_{R,end}}{\eta_{EM}}$$

$$m_{batt} = \frac{1}{E} \left[ (P_{R,shaft,endure actual} / \eta_{EM}) t_{endure} + (P_{payload} + P_{fcs})(P_{endure} + 2t_{cruise}) \right. \\ \left. + P_{climb,elec} t_{climb} \right]$$

$$WF_{endure} = 1$$

Charge Sustaining Strategy:

$$P_{EM} = \frac{P_{R,end}}{\eta_{EM}}$$

$$m_{batt} = \frac{(P_{R,shaft,endure actual} / \eta_{EM} + P_{payload} + P_{fcs}) t_{endure}}{E}$$

$$WF_{endure} = 1$$

Single Propeller:

$$WF_{cruise} = WF_{cruise,original} \left[ 1 - SFC_{cruise} t_{cruise} (P_{payload} + P_{fcs}) / (\eta_{gen} W_0) \right]$$

Dual Propeller:

$$WF_{cruise} = WF_{cruise,original} [1 - SFC_{cruise} t_{cruise} P_{windmill} / W_0]$$

Charge Sustaining with Segmented ISR Loiter Strategy:

$$t_{endure,seg1} = \frac{t_{endure}}{1 + 0.7n_{segments}}$$

$$t_{endure,segn} = 0.7t_{endure,seg1}$$

$$P_{A,charge} = P_{EM} - P_{payload} - P_{fcs}$$

$$m_{batt} = \frac{(P_{R,shaft,endure\ actual} / \eta_{EM} + P_{payload} + P_{fcs}) t_{endure,seg1}}{E}$$

$$m_{batt,reduction} = \frac{(P_{R,shaft,endure\ actual} / \eta_{EM} + P_{payload} + P_{fcs}) t_{endure}}{E} - m_{batt}$$

$$t_{charge} = C_{batt} / P_{A,charge}$$

$$WF_{endure} = (W_0 - m_{fuel,charge}) / W_0$$

$$m_{fuel,charge} = SFC_{cruise} t_{charge} n_{recharge} (P_{R,shaft,endure\ actual} + P_{EM} / \eta_{gen})$$

Single Propeller:

$$P_{EM} = (C_{batt} / t_{charge} + P_{payload} + P_{fcs})$$

$$WF_{cruise} = WF_{cruise,original} [1 - SFC_{cruise} t_{cruise} (P_{payload} + P_{fcs}) / (\eta_{gen} W_0)]$$

Dual Propeller:

$$P_{EM} = MAX(P_{windmill} \eta_{gen} \eta_{prop2} | P_{R,shaft,endure\ actual})$$

$$WF_{cruise} = WF_{cruise,original} [1 - SFC_{cruise} P_{windmill} (P_{payload} + P_{fcs}) / W_0]$$

## Appendix B: Sample Data

**Table B-1: Market survey results for similar aircraft**

<i>UAS</i>	<i>Manufacturer</i>	<i>Propulsion Type</i>	<i>Gross Weight (kg)</i>	<i>Wing Area (m<sup>2</sup>)</i>	<i>Wing Loading (kg/m<sup>2</sup>)</i>	<i>Aspect Ratio</i>	<i>Empty Weight Fraction</i>
ScanEagle	Insitu (Boeing)	ICE	18.0	0.884	199.8	13.2	0.667
SilverFox	Advanced Ceramics Research (BAE)	ICE	11.4	0.592	188.9	8.4	0.639
Pointer	AeroVironment	Electric	4.54	0.553	80.5	13.5	0.500
Aerosonde Mark 4.4	AAI	ICE	14.0	0.550	249.7	15.2	0.607
Harmon Optimum	-	Hybrid	13.6	1.48	90.0	14.6	0.630

Sources: 28, 44, 55 - 59

**Table B-2: Commercially available internal combustion engine data**

<i>Manufacturer</i>	<i>Model</i>	<i>Cycle</i>	<i>Fuel</i>	<i>Power Rating (HP)</i>	<i>Weight (lbf)</i>	<i>P/W (hp/lb)</i>
3W	28i	2-Stroke	Gasoline	3.4	2.67	1.27
3W	55i	2-Stroke	Gasoline	5.2	4.27	1.22
Cosworth*	AE1	2-Stroke	Diesel	3.5	9.33	0.38
Enya	61CX TN	2-Stroke	Diesel	1.7	0.83	2.04
Enya	R155-4C	4-Stroke	Glow	2.5	2.11	1.18
Enya	41-4CD TN	4-Stroke	Diesel	0.7	0.93	0.75
Fuji-Imvac	BT-24EI	2-Stroke	Gasoline	2.2	2.95	0.75
Fuji-Imvac	BT-34EI	2-Stroke	Gasoline	3.2	3.80	0.84
Fuji-Imvac	BF-25EI	4-Stroke	Gasoline	1.6	4.23	0.38
Fuji-Imvac	BF-34EI	4-Stroke	Gasoline	2.0	5.46	0.37
OS	25FX	2-Stroke	Glow	0.84	0.55	1.53
OS	61FX	2-Stroke	Glow	1.90	1.21	1.57
OS	FS-40S	4-Stroke	Glow	0.65	0.78	0.83
OS	FS-91S II	4-Stroke	Glow	1.6	1.43	1.12
Super Tigre	GS-40	2-Stroke	Glow	1.2	0.82	1.47
Super Tigre	GS-45	2-Stroke	Glow	1.5	0.83	1.82
BME/Super Tigre	0.90ci	2-Stroke	Gasoline	2.5	1.63	1.54
					Avg. P/W =	1.12

Sources: 60 - 65

\* Currently in development for the USN Ultra Endurance UAV program<sup>61</sup>

**Table B-3: Commercially available brushless electric motor data**

<i>Manufacturer</i>	<i>Model</i>	<i>Type</i>	<i>Kv (RPM/V)</i>	<i>Weight (kg)</i>	<i>Surge Power (W)</i>	<i>Continuous Power (W)</i>	<i>P/W (W/kg)</i>	<i>P/W (hp/lbf)</i>	<i>Overtorque</i>	<i>Efficiency</i>
AXI	5325/16 Gold	Outrunner	350	0.58	1806	1506	2619	1.59	1.20	0.85-0.90
AXI	4130/16 Gold	Outrunner	385	0.41	1187	831	2032	1.24	1.43	0.84-0.88
Flyware	LRK 350/10-12.5W	Outrunner	2300	0.12	300	150	1250	0.76	2.00	0.84
Flyware	LRK 350/20-12.5W	Outrunner	1220	0.20	650	400	2051	1.25	1.63	0.85
Flyware	LRK 350/25-12.5W	Outrunner	990	0.24	750	500	2128	1.29	1.50	0.84
Hacker	A30-22S	Outrunner	1440	0.07	250	144	2028	1.23	1.74	0.85-0.95
Hacker	A30-12M	Outrunner	1370	0.10	350	227	2163	1.32	1.54	0.85-0.95
Hacker	A30-10XL	Outrunner	900	0.18	650	373	2089	1.27	1.74	0.85-0.95
Hacker	A30-8XL	Outrunner	1100	0.18	650	434	2429	1.48	1.50	0.85-0.95
Hacker	A40-10L	Outrunner	500	0.35	1100	706	2024	1.23	1.56	0.85-0.95
NEU	1210	Outrunner	1850	0.01	125	75	5398	3.28	1.67	0.93
NEU	1215	Outrunner	1675	0.02	225	125	6123	3.72	1.80	0.93
NEU	1220	Outrunner	1625	0.03	250	150	5569	3.39	1.67	0.93
NEU	1230	Outrunner	1675	0.03	375	200	6003	3.65	1.88	0.93
NEU	1240	Outrunner	1625	0.04	550	300	7558	4.60	1.83	0.93
NEU	1105	Inrunner	6660	0.07	400	200	3067	1.87	2.00	0.80-0.85
NEU	1107	Inrunner	3850	0.10	600	300	2860	1.74	2.00	0.80-0.85
NEU	1110	Inrunner	8400	0.11	1000	400	3527	2.15	2.50	0.80-0.85
NEU	1112	Inrunner	6500	0.13	1200	600	4503	2.74	2.00	0.80-0.85
NEU	1115	Inrunner	5200	0.16	1400	700	4257	2.59	2.00	0.80-0.85
NEU	1706	Inrunner	1900	0.16	1200	600	3779	2.30	2.00	0.90
Average =							4786	2.13	1.77	0.86-0.90

Sources: 66 - 69

Note: Highlighted cell indicates estimated power specifications based on Eq. 9

**Table B-4: Sample QPROP results**

<i>Motor</i>	<i>Condition</i>	<i>Est <math>\eta_{Prop}</math></i>	<i>P<sub>R</sub> (W)</i>	<i>V (m/s)</i>	<i>T (N)</i>	<i>APC 16x10e</i>			<i>APC 14x10e</i>			<i>APC 7x4</i>		
						$\eta_{EM}$	$\eta_{Prop}$	$\eta_{Total}$	$\eta_{EM}$	$\eta_{Prop}$	$\eta_{Total}$	$\eta_{EM}$	$\eta_{Prop}$	$\eta_{Total}$
Hacker A30-10XL	Climb	0.50	378	14.4	26.3	0.74	0.66	0.49	0.79	0.59	0.47	0.92	0.38	0.35
	Cruise	0.60	295	20.5	14.4	0.78	0.80	0.62	0.82	0.77	0.63	0.89	0.57	0.51
	Endure	0.75	138	14.4	9.6	0.79	0.77	0.61	0.82	0.74	0.61	0.85	0.52	0.44

<i>Motor</i>	<i>Condition</i>	<i>Est <math>\eta_{Prop}</math></i>	<i>P<sub>R</sub> (W)</i>	<i>V (m/s)</i>	<i>T (N)</i>	<i>APC 16x10e</i>			<i>APC 14x10e</i>			<i>APC 7x4</i>		
						$\eta_{EM}$	$\eta_{Prop}$	$\eta_{Total}$	$\eta_{EM}$	$\eta_{Prop}$	$\eta_{Total}$	$\eta_{EM}$	$\eta_{Prop}$	$\eta_{Total}$
Hacker A30-8XL	Climb	0.50	378	14.4	26.3	0.75	0.66	0.50	0.80	0.59	0.47	0.91	0.38	0.35
	Cruise	0.60	295	20.5	14.4	0.79	0.79	0.62	0.82	0.78	0.64	0.87	0.57	0.50
	Endure	0.75	138	14.4	9.6	0.79	0.77	0.61	0.82	0.74	0.61	0.82	0.52	0.43

<i>Motor</i>	<i>Condition</i>	<i>Est <math>\eta_{Prop}</math></i>	<i>P<sub>R</sub> (W)</i>	<i>V (m/s)</i>	<i>T (N)</i>	<i>APC 14x10e</i>			<i>APC 16x10e</i>			<i>APC 8x6</i>		
						$\eta_{EM}$	$\eta_{Prop}$	$\eta_{Total}$	$\eta_{EM}$	$\eta_{Prop}$	$\eta_{Total}$	$\eta_{EM}$	$\eta_{Prop}$	$\eta_{Total}$
NEU 1210-1850	Climb	0.60	368	14.4	25.6	0.54	0.60	0.33	0.50	0.67	0.33	0.84	0.42	0.35
	Cruise	0.78	266	20.5	13.0	0.72	0.83	0.60	0.55	0.80	0.44	0.83	0.54	0.45
	Endure	0.80	124	14.4	8.6	0.66	0.75	0.50	0.60	0.78	0.46	0.89	0.59	0.52

<i>Motor</i>	<i>Condition</i>	<i>Est <math>\eta_{Prop}</math></i>	<i>P<sub>R</sub> (W)</i>	<i>V (m/s)</i>	<i>T (N)</i>	<i>APC 14x10e</i>			<i>APC 16x10e</i>			<i>APC 8x6</i>		
						$\eta_{EM}$	$\eta_{Prop}$	$\eta_{Total}$	$\eta_{EM}$	$\eta_{Prop}$	$\eta_{Total}$	$\eta_{EM}$	$\eta_{Prop}$	$\eta_{Total}$
Hacker A30-10XL	Climb	0.60	368	14.4	25.6	0.79	0.60	0.48	0.75	0.67	0.50	0.91	0.42	0.38
	Cruise	0.78	266	20.5	13.0	0.82	0.79	0.64	0.79	0.80	0.63	0.87	0.59	0.51
	Endure	0.80	124	14.4	8.6	0.82	0.75	0.62	0.80	0.78	0.62	0.89	0.64	0.57

## Appendix C: MATLAB Code

```

function []=HEUASdesign()
% Algorithm for Sizing Hybrid-Electric UAS
% Capt Ryan Hiserote (USAF)
% Air Force Institute Technology
% Master's Thesis: 'Analysis of Hybrid-Electric Propulsion Systems Designs
%                               for Small Unmanned Aircraft Systems (UAS)'
%
%
% Last Updated: 17 Feb 2010
%
% Original code written by LtCol Fred Harmon (USAF)
% University of California-Davis
% References:
% Anderson, Intro to Flight, 4th Edition
% Anderson, Aircraft Performance and Design
% Raymer, Aircraft Design: A Conceptual Approach, 2nd Edition

% Clear Workspace
close all; clear all; clc;

% Title and Date-Time Stamp
timestamp = clock;
disp('Hybrid-Electric UAS Sizing Program');
disp(['Date: ',date,'      Time: ',num2str(timestamp(4)),':', num2str(timestamp(5))]);
disp(' ');

% Declare Global Variables
global uas_Cdo uas_e prop_m prop_n bat_ED EM_eff EM_eff_gen EM_overtrq EM_PW_ratio...
ICE_PW_ratio start_m SFC_cruise SFC_endure des_uas_m des_pay_m des_pay_P...
des_fcs_P des_uas_S des_uas_AR WF_empty perf_tendure perf_tcruise perf_ROC...
perf_Vcruise perf_Vmax sadmin safetyfactor g msec2kts kts2msec W2hp hp2W uas_W...
prop_W start_W h h_TO h_AGL rho rho_TO tclimb generator_P_W prop_drag_P_W...
chargetype hybridtype n_recharge prop_eff_x

% User Specified Inputs
% Aerodynamic Parameters
uas_Cdo=0.036; % Zero-lift drag coefficient
uas_e=0.85; % Oswald efficiency factor

% Propulsion Component Specifications
% Electric Motor (EM):
EM_eff=0.85; % Typical outrunner EM efficiency
EM_eff_gen=0.75; % Typical EM efficiency as a generator
EM_overtrq=1.75; % EM over-torque Factor
% Note: Max Power = Continuous Power * Over-torque Factor
% Allows motor to provide surge power for approximately 30 seconds
EM_PW_ratio=3288; % Typical EM power-to-weight (3288 W/kg=2 hp/lb)

% Internal Combustion Engine (ICE):
ICE_PW_ratio=1233; % Typical ICE power-to-weight (1233 W/kg=.75 hp/lb)
% Specific Fuel Consumption (converted from lb/hp/hr to N/Ws)
SFC_cruise = 1.0*1.6576E-6; % SFC @ cruise speed power
SFC_endure = 1.5*1.6576E-6; % SFC @ endurance speed power

% Section provides capability to use engine efficiency values and vary
% fuel type instead of specifying SFC:
%LHV = 42.358/3600; % Lower heating value converted to kWh/g
% Reformulated gasoline = 42.358 MJ/kg
% Conventional diesel = 42.791 MJ/kg
% JP-8 = 43.147 MJ/kg
% Fischer-Tropsch diesel = 43.247 MJ/kg
%cruise_eff=0.091; % Engine efficiency during cruise
%endure_eff=0.068; % Engine efficiency during endurance
%SFC_cruise=1/(cruise_eff*LHV)*2.725E-9; % SFC (N/Ws)
%SFC_endure=1/(endure_eff*LHV)*2.725E-9; % SFC (N/Ws)
% Note: 2.725E-9 converts from kWh/g to N/Ws

% Starting Mechanism:
start_m_case1=0.15; % Clutch mass (kg)
start_m_case2=0.30; % Electric starter mass (kg)
start_m_case3=0.30; % Electric starter mass (kg)

```

```

mech_eff_case1 = 0.95; % Mechanical efficiency for clutch-start
mech_eff_case2 = 0.97; % Mechanical efficiency for electric-start
mech_eff_case3 = 1.0; % Mechanical efficiency for centerline-thrust

% Propeller:
prop_n_case1 = 1; % Single prop design
prop_n_case2 = 1; % Single prop design
prop_n_case3 = 2; % Dual prop design
% Propeller efficiency variable form:
% [climb prop 1, cruise prop 1, endure prop 1;
%  climb prop 2, cruise prop 2, endure prop 2]
prop_eff_case1 = [0.6, 0.78, 0.80; 1, 1, 1];% Clutch-start
prop_eff_case2 = [0.6, 0.78, 0.80; 1, 1, 1];% Electric-start
prop_eff_case3 = [0.6, 0.80, 0.78; 0.6, 0.78, 0.80];%Centerline-thrust
% Note: Propeller #1 sized for cruise. Propeller #2 sized for endurance
prop_m=0.17; % Prop mass(kg) same propeller size (20x8) for all cases

% UAS Design Parameters
des_uas_m=13.6; % UAS mass (kg), 13.6 kg=>30 lbf
des_pay_m=2.27; % Payload mass (kg), 2.27 kg=>5 lbf
des_pay_P=25; % Payload Power (W)
des_fcs_P=10; % Flight control system (servos & avionics) power (W)
des_uas_S=1.48; % Wing area of original design (m^2)
des_uas_AR=14.6; % AR of original Design
WF_empty=0.63; % Weight fraction for the empty weight of original UAS
% Empty weight fraction for HEUAS will be calculated
% Reference: Anderson-P&D, pg 400

% Performance Parameters
perf_tendure=3*3600; % Time for endurance (s)
perf_tcruise=3600; % Time for cruise, one-way (s)
perf_ROC=2.032; % Rate-of-Climb (m/s), 2m/s=>120m/min=>400 ft/min
% Note: ScanEagle UAS max climb rate = 150 m/min
perf_Vcruise = 20.5; % Cruise Velocity (m/s) 20.5 m/s = 40 kts
perf_Vmax=30.9; % Max Velocity (m/s), 30.9 m/s=>60 kts
sdmin=2.57; % Minimum speed delta between stall and endurance speeds(2.57 m/s=>5 kts)
% Note: Parameter is for optimization constraint to ensure the stall
% speed remains within a reasonable range of the theoretical endurance
% speed. Preliminary results show stall will always exceed theoretical
% endurance speed
safetyfactor = 2.57;
% Safety factor for actual endurance speed (2.57 m/s=>5 kts)
% Note: Ensures the actual endurance speed will be a factor of safety
% greater than the calculated stall speed
% Actual Vendure=Theoretical Vendure +sdmin + safetyfactor

% Select Altitude for the Calculations
h_TO=input('Enter takeoff altitude (meters AMSL): ');
%Note: Bagram Airfield, Afghanistan = 1492m
% Kandahar International Airport, Afghanistan = 1017m
% Joint Base Balad, Iraq = 49m
% Wright-Patterson AFB, OH = 251m
% Source: WorldAeroData.com
h_AGL=input('Enter mission altitude (meters AGL): ');
disp(' ');
h = h_TO + h_AGL;
[T_TO, a_TO, P_TO, rho_TO] = atmosisa(h_TO);
[T, a, P, rho] = atmosisa(h);
disp(['Mission Altitude Density (kg/m^3) = ', num2str(rho)]);
disp(' ');

% Constants and Preliminary Calculations
g=9.81; % Acceleration due to gravity (m/s^2)
msec2kts=1.944; % Unit conversion (m/s->kts)
kts2msec=0.5144; % Unit conversion (kts->m/s)
W2hp=1.34/1000; % Unit conversion (W->hp)
hp2W=0.75*1000; % Unit conversion (hp->W)
uas_W=des_uas_m*g; % Weight of UAS (N)
prop_W=prop_m*g; % Prop weight (N)

```

```

start_W=start_m*g; % Starter weight (N)
tclimb = h_AGL/perf_ROC; % Time to climb (s)

% Determine Power to Overcome Windmilling Propeller Drag During Cruise
prop_D=0.508; % Propeller diameter (m), 20in=.508m
fuselage_D=0.1524; % Fuselage diameter (m), 6in=.15m
prop_A = pi*(prop_D^2-fuselage_D^2)/4; % Cross sectional area
prop_Cp = 0.35; % Typical coefficient of performance

prop_drag_P_W_case1=0; % Zero rear prop drag
prop_drag_P_W_case2=0; % Zero rear prop drag
prop_drag_P_W_case3=0.5*prop_A*prop_Cp*perf_Vcruise^3;
% Power (W) to overcome drag induced by rear propeller (windmill)

% Select Battery Type
disp('Select Battery Type:');
disp(' 1: Lithium-ion Polymer (175 Wh/kg)');
disp(' 2: Lithium-Sulfur (300 Wh/kg)');
disp(' ');
batterytype=input('Enter your selection: ');
disp(' ');
switch batterytype
case 1
    bat_ED=175; %Lithium-ion polymer battery specific energy (Wh/kg)
case 2
    bat_ED=300; %Lithium-sulfur battery specific energy (Wh/kg)
end

% Select Battery Discharge Method
disp('Select Battery Discharge Method:');
disp(' 1: Charge Depletion');
disp(' 2: Charge Sustaining');
disp(' 3: Charge Sustaining with Segmented ISR Loiter');
disp(' ');
chargetype=input('Enter your selection: ');
disp(' ');
switch chargetype
case 1
    % Battery pack state of charge (SOC) = 100% at takeoff/launch
    % and will not recharge during mission
    disp('Note: Battery Pack Will Not Recharge During Mission');
    charge_P_W=0; % Eliminate recharging power
    generator_P_W=0; % Generator output power (W) required
case 2
    % Battery recharges during cruise to SOC=100% for endurance leg
    disp('Note: Battery Pack Charges to 100% for Endurance Leg');
    charge_P_W=50; % Excess ICE power for charging (W)
    generator_P_W=des_pay_P+des_fcs_P+charge_P_W; % Generator output power (W)
case 3
    % Same as Case 2 with segmented loiter to recharge battery pack
    disp(['Note: Aircraft Will Perform Complete ISR Loiter with'...
        ', Periodic Interruption for ICE Powered Recharging']);
    disp(' ');
    n_recharge=input(['Enter Number of Recharging Cycles for ',...
        num2str(perf_tendure/3600), ' hour loiter: ']);
    charge_P_W=50; % Excess ICE power for charging (W)
    generator_P_W=des_pay_P+des_fcs_P+charge_P_W; % Generator output power (W)
end

% Select Hybrid Design to Optimize
disp(' ');
disp('Select Hybrid Configuration for Optimization:');
disp(' 1: Clutch-Start Parallel Hybrid');
disp(' 2: Electric-Start Parallel Hybrid');
disp(' 3: Centerline Thrust Hybrid');
disp(' 4: Compare all of the Above');

```

```

disp(' ');
profile=input('Enter your selection: ');
disp(' ');
disp('%%%%%%%%%%%%%%%%%%%%%%%%%%%%%%%%%%%%%%%%%%%%%%%%%%%%%%%%%%%%%%%%%%%%%%%%');

switch profile
case 1
    hybridtype = 'Clutch-Start';
    disp('Begin Calculations for: Clutch-Start Parallel Hybrid');
    prop_eff = prop_eff_case1; % Prop efficiency
    mech_eff = mech_eff_case1; % Mechanical efficiency
    prop_n=prop_n_case1; % Number of propellers
    prop_eff_x = 2; % Trigger to eliminate propeller efficiency during charging
    prop_drag_P_W = prop_drag_P_W_case1; % Drag from prop windmill
    start_m=start_m_case1; % Starting mechanism mass

    [x,EM_P_W]=optimizeUAS(prop_eff, mech_eff);
    [WF_component_org, WF_mission_org, WF_propulsion_org, WF_component,...
     WF_mission, WF_propulsion, EM_P_W_act]= ...
    postprocess(x,EM_P_W,prop_eff,mech_eff);
    WFplot(WF_component_org, WF_mission_org, WF_propulsion_org, WF_component,...
     WF_mission, WF_propulsion);
    disp('%%%%%%%%%%%%%%%%%%%%%%%%%%%%%%%%%%%%%%%%%%%%%%%%%%%%%%%%%%%%%%%%%%%%%%%%');

case 2
    hybridtype = 'Electric-Start';
    disp('Begin Calculations for: Electric-Start Parallel Hybrid');
    prop_eff = prop_eff_case2; % Prop efficiency
    mech_eff = mech_eff_case2; % Mechanical efficiency
    prop_n=prop_n_case2; % Number of propellers
    prop_eff_x = 2; % Trigger to eliminate propeller efficiency during charging
    prop_drag_P_W = prop_drag_P_W_case2; % Drag from windmilling prop
    start_m=start_m_case2; % Starting mechanism mass

    [x,EM_P_W]=optimizeUAS(prop_eff, mech_eff);
    [WF_component_org, WF_mission_org, WF_propulsion_org, WF_component,...
     WF_mission, WF_propulsion, EM_P_W_act]= ...
    postprocess(x,EM_P_W,prop_eff,mech_eff);
    WFplot(WF_component_org, WF_mission_org, WF_propulsion_org, WF_component,...
     WF_mission, WF_propulsion);
    disp('%%%%%%%%%%%%%%%%%%%%%%%%%%%%%%%%%%%%%%%%%%%%%%%%%%%%%%%%%%%%%%%%%%%%%%%%');

case 3
    hybridtype = 'Centerline-Thrust';
    disp('Begin Calculations for: Centerline-Thrust Hybrid');
    prop_eff = prop_eff_case3; % Prop efficiency
    mech_eff = mech_eff_case3; % Mechanical efficiency
    prop_n=prop_n_case3; % Number of propellers
    prop_eff_x = 1; % Trigger to add propeller efficiency during charging
    if (chargetype==1) % Generator power either 0 or compensated by windmill
        prop_drag_P_W = 0; % Drag from windmilling prop
    else
        prop_drag_P_W = prop_drag_P_W_case3; % Drag from windmilling prop
        generator_P_W=0;
    end
    start_m=start_m_case3; % Starting mechanism mass

    [x,EM_P_W]=optimizeUAS(prop_eff, mech_eff);
    [WF_component_org, WF_mission_org, WF_propulsion_org, WF_component,...
     WF_mission, WF_propulsion, EM_P_W_act]= ...
    postprocess(x,EM_P_W,prop_eff,mech_eff);
    WFplot(WF_component_org, WF_mission_org, WF_propulsion_org, WF_component,...
     WF_mission, WF_propulsion);
    disp('%%%%%%%%%%%%%%%%%%%%%%%%%%%%%%%%%%%%%%%%%%%%%%%%%%%%%%%%%%%%%%%%%%%%%%%%');

case 4
    % Case runs three previous cases and utilizes a different plotting function
    % to visually compare results

    % Clutch-start design

```

```

hybridtype = 'Clutch-Start';
disp(' ');
disp('Begin Calculations for: Clutch-Start Parallel Hybrid');
prop_eff = prop_eff_case1; % Prop efficiency
mech_eff = mech_eff_case1; % Mechanical efficiency
prop_n=prop_n_case1; % Number of propellers
prop_eff_x = 2; % Trigger to eliminate propeller efficiency during charging
prop_drag_P_W = prop_drag_P_W_case1; % Drag from windmilling prop
start_m=start_m_case1; % Starting mechanism mass

[x1,EM_P_W1]=optimizeUAS(prop_eff, mech_eff);
[WF_component_org1, WF_mission_org1, WF_propulsion_org1, WF_component1,...
 WF_mission1, WF_propulsion1, EM_P_W_act1]=...
 postprocess(x1,EM_P_W1,prop_eff,mech_eff);
disp('%%%%%%%%%%%%%%%%%%%%%%%%%%%%%%%%%%%%%%%%%%%%%%%%%%%%%%%%%%%%%%%%%%%%%%%%');

% Electric-start design
hybridtype = 'Electric-Start';
disp(' ');
disp('Begin Calculations for: Electric-Start Parallel Hybrid');
prop_eff = prop_eff_case2; % Prop efficiency
mech_eff = mech_eff_case2; % Mechanical efficiency
prop_n=prop_n_case2; % Number of propellers
prop_eff_x = 2; % Trigger to eliminate propeller efficiency during charging
prop_drag_P_W = prop_drag_P_W_case2; % Drag from windmilling prop
start_m=start_m_case2; % Starting mechanism mass

[x2,EM_P_W2]=optimizeUAS(prop_eff, mech_eff);
[WF_component_org2, WF_mission_org2, WF_propulsion_org2, WF_component2,...
 WF_mission2, WF_propulsion2, EM_P_W_act2]=...
 postprocess(x2,EM_P_W2,prop_eff,mech_eff);
disp('%%%%%%%%%%%%%%%%%%%%%%%%%%%%%%%%%%%%%%%%%%%%%%%%%%%%%%%%%%%%%%%%%%%%%%%%');

% Center-line thrust design
hybridtype = 'Centerline-Thrust';
disp(' ');
disp('Begin Calculations for: Centerline-Thrust Hybrid');
prop_eff = prop_eff_case3; % Prop efficiency
mech_eff = mech_eff_case3; % Mechanical efficiency
prop_n=prop_n_case3; % Number of propellers
prop_eff_x = 1; % Trigger to add propeller efficiency during charging
if (chargetype==1)
    prop_drag_P_W = 0; % Drag from windmilling prop
else
    prop_drag_P_W = prop_drag_P_W_case3; % Drag from windmilling prop
    generator_P_W=0;
end
start_m=start_m_case3; % Starting mechanism mass

[x3,EM_P_W3]=optimizeUAS(prop_eff, mech_eff);
[WF_component_org3, WF_mission_org3, WF_propulsion_org3, WF_component3...
 , WF_mission3, WF_propulsion3, EM_P_W_act3]=...
 postprocess(x3,EM_P_W3,prop_eff,mech_eff);
disp('%%%%%%%%%%%%%%%%%%%%%%%%%%%%%%%%%%%%%%%%%%%%%%%%%%%%%%%%%%%%%%%%%%%%%%%%');

% Combine results into matrix form:
x = [x1, x2, x3];
EM_P_W_act = [EM_P_W_act1, EM_P_W_act2, EM_P_W_act3];
WF_component = [WF_component1, WF_component2, WF_component3];
WF_mission = [WF_mission1, WF_mission2, WF_mission3];
WF_propulsion = [WF_propulsion1, WF_propulsion2, WF_propulsion3];

% Plot weight fractions
Comparisonplot(WF_component, WF_mission, WF_propulsion, x, EM_P_W_act);

disp(' ');
disp('%%%%%%%%%%%%%%%%%%%%%%%%%%%%%%%%%%%%%%%%%%%%%%%%%%%%%%%%%%%%%%%%%%%%%%%%');
disp(' ');

```

end

```

end

% Function Performs Constrained Optimization Using FMINCON
function [x,EM_P_W]=optimizeUAS(prop_eff, mech_eff)
global uas_Cdo uas_e prop_m prop_n bat_ED EM_eff EM_eff_gen EM_overtrq EM_PW_ratio...
    ICE_PW_ratio start_m SFC_cruise SFC_endure des_uas_m des_pay_m des_pay_P...
    des_fcs_P des_uas_S des_uas_AR WF_empty perf_tendure perf_tcruise perf_ROC...
    perf_Vcruise perf_Vmax sadmin safetyfactor g msec2kts kts2msec W2hp hp2W uas_W...
    prop_W start_W h h_TO h_AGL rho rho_TO tclimb generator_P_W prop_drag_P_W...
    chargetype hybridtype n_recharge prop_eff_x

% Intial guesses and variable bounds:
% [W/S, AR, CLmax, Vstall, Vendure, ICE power]
x0=[100; 15; 1.2; 10; 8; 1000]; % Initial values for x
lb=[90; 8; 1.0; 5; 5; 300]; % Lower Bound for variables
ub=[200; 20; 1.25; 20; 20; 3000]; % Upper Bound for variables

disp(' ');
disp('Minimizing EM Power, Optimizing W/S, AR, Clmax, Vstall, Vendure, ICE Power');
disp(' ');
options=optimset('LargeScale','off','Display','final','MaxIter',15000,...
    'MaxFunEvals',75000);

[x,fval,exitflag,output]=fmincon(@SizeCost,x0,[],[],[],[],lb,ub,@SizeConstraint,options,
uas_W,uas_Cdo,uas_e,prop_eff,perf_Vcruise,perf_Vmax,rho,sadmin,generator_P_W,prop_eff_x);

% Adjust ICE power(W) for density at altitude, Anderson P&D, Eqn 3.12:
x(6)=x(6)/(1.132*rho/1.225-0.132);
% EM Power(W) for Theoretical Endurance Speed
EM_P_W=fval/(prop_eff(1,3)*EM_eff*mech_eff);
disp(' ');
disp('Optimization Completed:');
disp(['Exitflag (>0 if Converged, =0 if Max Iterations, <0 if No Convergence): ',...
    num2str(exitflag)])
output
output.algorithm
disp(' ');
disp('Solution Computed from Optimization:');
disp(['W/S (N/m^2): ', num2str(x(1))]);
disp(['Aspect Ratio: ', num2str(x(2))]);
disp(['Clmax: ', num2str(x(3))]);
disp(['Vstall (m/s): ',num2str(x(4))]);
%disp(['Vstall (kts): ', num2str(msec2kts*x(4))]);
disp(['Theoretical Vendure (m/s): ',num2str(x(5))]);
%disp(['Vendure (kts): ',num2str(msec2kts*x(5))]);
disp(['ICE Power for Cruise (W): ', num2str(x(6))]);
% Note: Cruise power includes power for electric generation
disp(['Power Required for Theoretical Endurance (W): ', num2str(fval)]);
disp(['EM Power for Theoretical Endurance (W): ', num2str(EM_P_W)]);
disp(' ');

% Function Provides Constraint Equations for Optimization
function [c,ceq]=SizeConstraint(x,uas_W,uas_Cdo,uas_e,prop_eff,perf_Vcruise,perf_Vmax,rho,sadmin,
generator_P_W,prop_eff_x)

% Constraints for Minimized Nonlinear Equation

% Variables
% x(1): Wing Loading, W/S (N/m^2)
% x(2): Aspect Ratio, AR
% x(3): Clmax
% x(4): Vstall (m/s)
% x(5): Vendure (m/s)
% x(6): Internal Combustion Engine Power (W)

% Nonequality Constraint

```

```

c=[x(4)-sdmin-x(5)]; % Note: Constraint keeps stall within specified margin of
                    % theoretical endurance speed. This is NOT a safety margin.
                    % Authors recognize that the stall must be greater than the
                    % theoretical endurance speed based on preliminary results

% Equality Constraints
ceq=[2*x(1)/(rho*x(3))-x(4)^2;
     2*x(1)/(rho*sqrt(3*uas_Cdo*pi*uas_e)*x(5)^2)-sqrt(x(2))];

(0.5*rho*perf_Vcruise^3*uas_W*uas_Cdo/x(1)+2*uas_W*x(1)/(rho*perf_Vcruise*pi*uas_e*x(2))+
prop_drag_P_W)/prop_eff(1,2)+generator_P_W/(EM_eff_gen*prop_eff(prop_eff_x,2)*prop_eff(2,
2))-mech_eff*x(6)];

end

% Function Provides Cost Function for Minimizing
function f=SizeCost(x,uas_W,uas_Cdo,uas_e,prop_eff,perf_Vcruise,perf_Vmax,rho,sdmin,
generator_P_W,prop_eff_x)

    % Nonlinear Equation to Minimize (Power Required for Endurance)

    % Variables
    % x(1): Wing Loading, W/S (N/m^2)
    % x(2): Aspect Ratio, AR
    % x(3): Clmax
    % x(4): Vstall (m/s)
    % x(5): Vendure (m/s)
    % x(6): Internal Combustion Engine Power (W)

    % Function to Minimize=Power Required for Endurance
    % (Anderson, P&D, Eqns 5.38 & 5.56)
    f=(uas_W*sqrt(2*x(1)/rho)*4*uas_Cdo/(3*uas_Cdo*pi*uas_e*x(2))^0.75);

end

end

% Function performs postprocessing to calculate size of propulsion components
function
[WF_component_org,WF_mission_org,WF_propulsion_org,WF_component,WF_mission,WF_propulsion,
EM_P_W_act]=postprocess(x,EM_P_W,prop_eff,mech_eff)

global uas_Cdo uas_e prop_m prop_n bat_ED EM_eff EM_eff_gen EM_overtrq EM_PW_ratio...
ICE_PW_ratio start_m SFC_cruise SFC_endure des_uas_m des_pay_m des_pay_P...
des_fcs_P des_uas_S des_uas_AR WF_empty perf_tendure perf_tcruise perf_ROC...
perf_Vcruise perf_Vmax sdmin safetyfactor g msec2kts kts2msec W2hp hp2W uas_W...
prop_W start_W h h_TO h_AGL rho rho_TO tclimb generator_P_W prop_drag_P_W...
chargetype hybridtype n_recharge prop_eff_x

% Assign Variables
WLstall=x(1); % Wing Loading for Stall (N/m^2), Anderson-P&D, Eqn 8.26
uas_WL=WLstall; % Wing Loading (N/m^2)
uas_AR=x(2); % Aspect Ratio
uas_Clmax=x(3); % Max Cl during Cruise
Vstall=x(4); % Stall Velocity (m/s)
Vendure=x(5); % Theoretical Endurance Velocity (m/s)
ICE_P_W=x(6); % ICE Power (W)

% Aerodynamic Calculation Section
% Determine Wing Area and Wing Loading
% Calculated Wing Area of UAS based on Wing Loading for Stall (m^2):
uas_S=uas_W/WLstall;
if (uas_S>des_uas_S)
    disp(' ');
    disp(['S is larger than desired due to Wing Loading for Stall->',...
         'Increase CLmax, Vstall, or S']);
    disp(['Desired S (m^2): ', num2str(des_uas_S)]);
    disp(['Calculated S (m^2): ', num2str(uas_S)]);
end

```

```

% Wing Geometry Calculations
% Assumes rectangular wing
uas_wing_span=sqrt(uas_S*uas_AR); % Wing Span (m)
uas_wing_chord=uas_S/uas_wing_span; % Wing Chord (m)

% Calculate Endurance Parameter and L/D Ratio
uas_K=1/(pi*uas_e*uas_AR); % Drag Polar Constant
% Endurance Parameter (Cl^1.5/Cd), Anderson-Flight, Eqn 6.87
uas_Cl_15_Cd=(3*uas_Cdo/uas_K).^0.75/(4*uas_Cdo);
% Lift-to-Drag Ratio (Cl/Cd), Anderson-Flight, Eqn 6.85
uas_Cl_Cd=sqrt(uas_Cdo/uas_K)/(2*uas_Cdo);

% Check Margin Between Theoretical Vendure and Vstall, Sets Actual Vendure
stallmargin = Vendure-Vstall; % Should equal 'sadmin' from optimization
disp(' ');
disp(['Difference Between Endurance Velocity and Stall Velocity (kts): ',...
num2str(msec2kts*(stallmargin))]);

if (stallmargin<0) % Note: Checking stall margin -- should always be < 0
    Vendure_act=Vstall+safetyfactor; % Calculates Actual Vendure
    disp(['Actual Endurance Velocity (m/s) = ', num2str(Vendure_act)]);
    disp(['Actual Endurance Velocity (kts) = ', num2str(msec2kts*(Vendure_act))]);
else
    Vendure_act=Vendure; % Sets Actual Vendure to Theoretical Vendure
end

% Power Required Calculation Section
% Note: PR=Power Required (Aerodynamic)
%       PS=Shaft Power Required
%       PR=PS/prop_efficiency

% Determine Power Required for Theoretical Endurance
Cl=uas_WL/(0.5*rho*Vendure^2); % Lift Coefficient for Endurance, Anderson-P&D Eq 5.11
Cd=uas_Cdo+uas_K*Cl^2; % Drag Coefficient for Endurance, Anderson-P&D Eq 5.10
uas_PR_Vendure=sqrt(2*uas_W^3*Cd^2/(rho*uas_S*Cl^3)); % Power for Vendure (W)
% Anderson-Flight, Eq 6.27
uas_PS_Vendure=uas_PR_Vendure/prop_eff(prop_n,3); % Shaft Power for Vendure (W)
% Anderson Eq 3.13

% Determine Power Required for Actual Endurance Speed
Cl=uas_WL/(0.5*rho*(Vendure_act)^2); % Lift Coefficient for Endurance
Cd=uas_Cdo+uas_K*Cl^2; % Drag Coefficient for Endurance
uas_PR_Vendure_act=sqrt(2*uas_W^3*Cd^2/(rho*uas_S*Cl^3)); % Power for Vendure(W)
% Anderson-Flight, Eq 6.27
uas_PS_Vendure_act=uas_PR_Vendure_act/prop_eff(prop_n,3); % Shaft Power for
Vendure(W)
% Anderson Eq 3.13

% Determine Size and Mass of EM for HEUAS
if (chargetype==1) % Charge Depletion
    % EM Size (Power Output) based on actual endurance power (W)
    EM_P_W_act = uas_PS_Vendure_act;
else
    if (chargetype==2) % Charge Sustaining
        % EM Size (Power Output) based on actual endurance power (W)
        EM_P_W_act = uas_PS_Vendure_act; % Actual EM Size (Power Output) (W)
        % Mass of batteries (kg) includes payload power endurance only:
        bat_m=(uas_PS_Vendure_act/EM_eff+des_pay_P+des_fcs_P)*...
            perf_tendure/(bat_ED*3600);
        bat_Wh = bat_m*bat_ED; % Battery storage (Wh)
    else
        % (chargetype==3) Charge Sustaining w/ Segmented ISR
        % EM is sized for recharging not actual endurance power
        if (prop_n==1) % Single Propeller Configurations

            charge_t = 3600; % Time(s) to recharge batteries to 70% SOC (1C Rate)
            % Endurance flight time for 1st segment
            perf_tendure_segment_1 = perf_tendure/(1+0.7*(n_recharge));
            % Endurance flight time for other segments

```

```

perf_tendure_segment_n = perf_tendure_segment_1*0.70;

% Battery mass (kg) sized for 1st segment
bat_m=(uas_PS_Vendure_act/EM_eff+des_pay_P+des_fcs_P)*...
perf_tendure_segment_1/(bat_ED*3600);

% Reduction in battery mass (kg):
bat_reduction_m=(uas_PS_Vendure_act/EM_eff+des_pay_P+des_fcs_P)*...
perf_tendure/(bat_ED*3600)-bat_m;

bat_Wh = bat_m*bat_ED; % Battery storage (Wh)

% EM is sized to charge battery pack to 70% SOC in 1 hour (1C Rate)
EM_P_W_act=(bat_Wh/charge_t*3600+des_pay_P+des_fcs_P);

% Power available for charging (W) while
% maintaining payload operation and endurance flight:
charge_PA = EM_P_W_act-des_pay_P-des_fcs_P;

else % (prop_n==2) Dual Propeller Configurations
% EM sized for maximum of power available from rear propeller
% through windmilling or power required for endurance
EM_P_W_act=max(prop_drag_P_W*EM_eff_gen*prop_eff(2,2),...
uas_PS_Vendure_act);

% Power available for charging (W) while
% maintaining payload operation and endurance flight:
charge_PA = EM_P_W_act-des_pay_P-des_fcs_P;

% Endurance flight time for 1st segment
perf_tendure_segment_1 = perf_tendure/(1+0.7*(n_recharge));
% Endurance flight time for other segments
perf_tendure_segment_n = perf_tendure_segment_1*0.70;

% Battery mass (kg) sized for 1st segment
bat_m=(uas_PS_Vendure_act/EM_eff+des_pay_P+des_fcs_P)*...
perf_tendure_segment_1/(bat_ED*3600);

bat_Wh = bat_m*bat_ED; % Battery storage (Wh)

charge_t=bat_Wh/charge_PA*3600; % Charge time

% Reduction in battery mass (kg):
bat_reduction_m=(uas_PS_Vendure_act/EM_eff+des_pay_P+des_fcs_P)*...
perf_tendure/(bat_ED*3600)-bat_m;

end
end
end
EM_m=EM_P_W_act/EM_PW_ratio; % Mass of EM (kg)
EM_W=EM_m*g; % Weight of EM (N)

% Determine Power Required to Meet ROC Requirement
V=[Vstall:0.5:perf_Vmax]; % Range of Velocities (m/s)
Cl=uas_WL./((0.5*rho*V.^2)); % Lift Coefficient, Anderson-Flight, Eq 6.26
Cd=uas_Cdo+uas_K*Cl.^2; % Drag Coefficient, Anderson-Flight, pg 359
PR_SL=sqrt(2*uas_W^3*Cd./((rho*uas_S*Cl.^3))); % PR(W) for steady level flight (S&L)
% Anderson-Flight, Eq 5.56
PR_climb=perf_ROC*uas_W*ones(size(Cd))+PR_SL; % PR for Climb (W),
% Anderson-Flight, Eq 6.50
uas_PRmin_climb=min(PR_climb); % PR min in PR_climb vector (W)
uas_PSmin_climb=uas_PRmin_climb/prop_eff(1,1); % Shaft Power Required for climb (W)

% Determine if Electric Power Needed for Climb
% Note: This approach assumes that using the ICE for climb alone is
% more efficient (lighter) than using the EM and batteries
disp(' ');
disp(['Shaft Power Required for Min ROC (W): ',num2str(uas_PSmin_climb)]);
if (uas_PSmin_climb>ICE_P_W)

```

```

% Calculate additional power (W) needed for climb:
uas_climb_add=uas_PSmin_climb-ICE_P_W;
disp('ICE Alone Not Sufficient for Climb');
disp(['Additional Power Needed (W): ',num2str(uas_climb_add)]);

if (uas_climb_add>EM_P_W_act*EM_overtrq)
    % EM provides maximum amount of power
    uas_climb_elec=EM_P_W_act*EM_overtrq;
    disp(['HEUAS Unable to Meet Min ROC Requirement by (W): ',...
        num2str(uas_climb_add-uas_climb_elec)]);
    % Calculate actual ROC based on max power:
    ROC_act = (ICE_P_W+uas_climb_elec-PR_SL)/(uas_W*ones(size(Cd)));
    disp(['ROC Reduced to (ft/min): ',num2str(196.9*ROC_act)]);
else
    % Calculate additional power needed from EM (W)
    uas_climb_elec=uas_climb_add;
    disp(['Min ROC Requirement Met by Adding Electric Power (W): ',...
        num2str(uas_climb_elec)]);
end
else
    uas_climb_elec=0; % ICE power sufficient for climb
    disp(['ICE Alone Exceeds Power for Climb by (W): ',...
        num2str(ICE_P_W-uas_PSmin_climb)]);
end

% Determine Power Required to Meet Max Velocity Requirement
Cl=uas_WL/(0.5*rho*perf_Vmax^2); % Lift Coefficient for Cruise, Anderson-P&D Eq 5.11
Cd=uas_Cdo+uas_K*Cl^2; % Drag Coefficient for Cruise, Anderson-P&D, Eq 5.10
uas_PR_Vmax=sqrt(2*uas_W^3*Cd^2/(rho*uas_S*Cl^3)); % Power Required for Vmax (W)
% Anderson-Flight, Eq 6.27
uas_PS_Vmax=uas_PR_Vmax/prop_eff(1,2); % Shaft Power Required for Vcruise (W)

% Determine Power Required to Meet Cruise Requirement

Cl=uas_WL/(0.5*rho*perf_Vcruise^2);%Lift Coefficient for Cruise, Anderson-P&D Eq 5.11
Cd=uas_Cdo+uas_K*Cl^2; % Drag Coefficient for Cruise, Anderson-P&D, Eq 5.10
uas_PR_Vcruise=sqrt(2*uas_W^3*Cd^2/(rho*uas_S*Cl^3));% Power Required for Vcruise (W)
% Anderson-Flight, Eq 6.27
uas_PS_Vcruise=uas_PR_Vcruise/prop_eff(1,2); % Shaft Power Required for Vcruise (W)

% Determine Power Required at Stall Conditions
Cl=uas_WL/(0.5*rho*Vstall^2); % Lift Coefficient for Stall
Cd=uas_Cdo+uas_K*Cl^2; % Drag Coefficient for Cruise
uas_PR_Vstall=sqrt(2*uas_W^3*Cd^2/(rho*uas_S*Cl^3)); % Power Required for Vstall (W)
% Anderson-Flight, Eq 6.27
uas_PS_Vstall=uas_PR_Vstall/prop_eff(prop_n,3); % Shaft Power Required for Vstall (W)

% Place Power Requirements into a Vector
% Shaft Power Required for the Mission Segments (W):
PS=[uas_PSmin_climb, uas_PS_Vcruise, uas_PS_Vendure, uas_PS_Vmax];
% Size of ICE to meet PR (W), includes payload power and generator efficiency:
ICE_P_W_org=max(PS)+ (des_pay_P+des_fcs_P)/EM_eff_gen;
ICE_P_hp_org=W2hp*ICE_P_W_org; % Size of ICE to meet PR (hp)
ICE_Size_in3_org=ICE_P_hp_org; % Size of ICE (in^3), assume 1 hp=1 in^3

% Plot Power Required Curve
V=[Vstall-2.57:0.5:perf_Vmax]; % Range of Velocities (m/s)
Cl=uas_WL./(0.5*rho*V.^2); % Lift Coefficient, Anderson-Flight, Eq 6.26
Cd=uas_Cdo+uas_K*Cl.^2; % Drag Coefficient, Anderson-Flight, pg 359
PR = sqrt(2*uas_W^3*Cd.^2/(rho*uas_S*Cl.^3));
figure;
plot(msec2kts*V,PR,'k--'); hold on;
plot(msec2kts*Vendure,uas_PR_Vendure,'bo'); hold on;
plot(msec2kts*Vstall,uas_PR_Vstall,'ro'); hold on;
plot(msec2kts*(Vstall+sdmin),uas_PR_Vendure_act,'go'); hold on;
plot(msec2kts*perf_Vcruise,uas_PR_Vcruise,'mo'); hold on;
xlabel('Velocity (kts)','fontsize',10); ylabel('Power (W)','fontsize',10);
legend_PR=legend('Power Required','Theoretical Endurance','Stall',...
    'Actual Endurance','Cruise','Location','NW');
set(legend_PR,'fontsize',8);

```

```

grid on
%title('Power Required to Meet Velocity Requirements');

% Section for Original UAS (non-hybrid)
% Mission Segment Weight Fractions for the Original Configuration
Wo=uas_W; % Desired UAS Weight (N)
WF_TO_org=0.999; % Weight Fraction for Warm up and TO
    % Assume catapult takeoff with no TO distance requirement
% Weight Fraction for Climb, Raymer-A/C Design Eq 17.97
    % Assumes endurance speed, min climb power, density at highest altitude
WF_climb_org = exp(-SFC_endure*h_AGL/(1-(0.5*rho*Vendure_act^2*uas_S)*...
    (uas_Cdo+uas_K*uas_Clmax^2)/(uas_PSmin_climb/Vendure_act)));
R=perf_Vcruise*perf_ttcruise; % Range of UAS during one-way cruise (m)
% Lift coefficient for cruise, Anderson-P&D, Eq 5.11
Cl_cruise=uas_WL/(0.5*rho*perf_Vcruise^2);
% Drag coefficient for cruise, Anderson-P&D, Eq 5.10
Cd_cruise=uas_Cdo+uas_K*Cl_cruise^2;
% Weight Fraction for Cruise, Derived from Breguet Formula:
WF_cruise_org=exp(-R*SFC_cruise/(prop_eff(1,2)*(Cl_cruise/Cd_cruise)));
% Lift Coefficient for Endurance, Anderson-P&D, Eq 5.11:
Cl_endure=uas_WL/(0.5*rho*Vendure_act^2);
% Drag Coefficient for Endurance, Anderson-P&D, Eq 5.10:
Cd_endure=uas_Cdo+uas_K*Cl_endure^2;
% Weight Fraction for Endurance, Raymer, Section 3.4:
WF_endure_org=exp(-Vendure_act*perf_tendure*SFC_endure/(prop_eff(1,3)*...
    (Cl_endure/Cd_endure)));
WF_landing_org=0.9975; % Weight Fraction for Landing, Raymer, Section 3.4
% Weight Fraction for Fuel, Raymer, Section 3.4
WF_fuel_org=1.06*(1-WF_TO_org*WF_climb_org*WF_cruise_org*WF_endure_org*...
    WF_cruise_org*WF_landing_org);
pay_W_org=Wo*(1-WF_fuel_org-WF_empty); % Calculate Payload Weight (N)
pay_m_org=pay_W_org/g; % Payload Mass of Original UAS (kg)
WF_pay_org=pay_W_org/Wo; % Weight Fraction for the Payload
ICE_m_org=ICE_P_W_org/ICE_PW_ratio; % Engine Mass of Original UAS (kg)
fuel_m_org=WF_fuel_org*Wo/g; % Fuel mass of Original UAS (kg)
ess_m_org=0.25; % Mass of original Generator (or Battery Pack) (kg)
uas_empty_m_org=des_uas_m-fuel_m_org-pay_m_org; % Empty Mass of Original UAS (kg)
uas_glider_m=uas_empty_m_org-ICE_m_org-ess_m_org-prop_m;% Glider Mass of Original(kg)
propulsion_m_org=ICE_m_org+ess_m_org+prop_m;% Propulsion System Mass of Original(kg)
% Weight Fraction for Entire Propulsion System for Original UAS:
WF_propulsion_tot_org=propulsion_m_org*g/Wo;
% Create vector for mission weight fractions:
WF_mission_org = [WF_TO_org; WF_climb_org; WF_cruise_org;...
    WF_endure_org; WF_landing_org];
% Create vector for propulsion system component weight fractions:
WF_propulsion_org = [WF_fuel_org; ICE_m_org/des_uas_m; ess_m_org/des_uas_m/2;...
    ess_m_org/des_uas_m/2; prop_m/des_uas_m];
% Create vector for aircraft component weight fractions:
WF_component_org = [uas_glider_m/des_uas_m; propulsion_m_org/des_uas_m;...
    uas_empty_m_org/des_uas_m; fuel_m_org/des_uas_m; pay_m_org/des_uas_m];

% Section for Hybrid-Electric UAS (HEUAS)
% Determine Mass and Storage Capacity of Batteries for HEUAS for Charge Depletion
if (chargetype==1)

    % Mass of batteries (kg) includes payload/avionics power for entire mission
    % Also includes electric power required for climbing
    bat_m=(uas_PS_Vendure_act/EM_eff*perf_tendure+(des_pay_P+des_fcs_P)*...
        (perf_tendure+perf_ttcruise^2)+uas_climb_elec*tclimb)/(bat_ED*3600);

    bat_Wh = bat_m*bat_ED; % Battery storage (Wh)

end

bat_W=bat_m*g; % Weight of Batteries (N)

% Determine Physical Size of ICE
ICE_P_hp=W2hp*ICE_P_W; % Size of ICE to meet PR (hp)
ICE_Size_in3=ICE_P_hp; % Size of ICE (in^3), assume 1 hp=1 in^3

```

```

% Mission Segment Weight Fractions for HEUAS Configuration
Wo=uas_W; % Desired UAS Weight (N)
WF_EM=EM_W/Wo; % Weight Fraction of EM
WF_bat=bat_W/Wo; % Weight Fraction of batteries
WF_TO=WF_TO_org; % Weight Fraction for Warm up and TO
% Assume catapult takeoff with no TO distance requirement
WF_climb=WF_climb_org; % Weight Fraction for Climb
if (chargetype==1) % Charge Depletion
    WF_cruise=WF_cruise_org;
    WF_endure=1; % Weight Fraction for Endurance, All-Electric (No Recharging)
else % Charge Sustaining (includes Segmented)
    if (prop_n==1) % Single Prop
        % Weight fraction for cruise = fuel required for cruise speed +
        % excess fuel required to power generator
        WF_cruise=WF_cruise_org*(1-SFC_cruise*(des_pay_P+des_fcs_P)/...
            EM_eff_gen*perf_tcruise/Wo);
    else % Dual Prop
        % Weight fraction for cruise = fuel required for cruise speed +
        % excess fuel required to power generator
        WF_cruise=WF_cruise_org*(1-SFC_cruise*prop_drag_P_W*perf_tcruise/Wo);
    end
end

if (chargetype==2) % Charge Sustaining Only
    WF_endure=1; % Weight Fraction for Endurance, All-Electric (No Recharging)

else % (chargetype==3) Segmented Loiter
    charge_fuel = SFC_cruise*(uas_PS_Vendure_act+EM_P_W_act/EM_eff_gen)*...
        charge_t*(n_recharge);
    % Fuel weight (N) required to recharge batteries (assume cruise SFC)
    WF_endure = (Wo-charge_fuel)/Wo;
    % Endurance weight fraction including fuel for recharging cycles
end
end

WF_landing=WF_landing_org; % Weight Fraction for Landing
% Weight Fraction for Fuel, Raymer, Section 3.4:
WF_fuel=1.06*(1-WF_TO*WF_climb*WF_cruise*WF_endure*WF_cruise*WF_landing);
ICE_m=ICE_P_W/ICE_PW_ratio; % Engine Mass of HEUAS (kg)
ICE_W=ICE_m*g; % ICE Weight (N)
WF_ICE=ICE_W/Wo; % Weight Fraction of ICE
WF_prop=prop_m*prop_n*g/Wo; % Weight Fraction of propeller(s)
fuel_m=WF_fuel*Wo/g; % Fuel mass of HEUAS (kg)
fuel_W=fuel_m*g; % Fuel Weight (N)
% Payload Mass of HEUAS (kg):
pay_m=des_uas_m-uas_glider_m-ICE_m-fuel_m-start_m-bat_m-EM_m-prop_m*prop_n;
pay_W=pay_m*g; % Payload Weight of HEUAS (N)
WF_pay=pay_W/Wo; % Weight Fraction for the Payload
uas_empty_m=des_uas_m-fuel_m-pay_m; % Empty Mass of HEUAS (kg)
propulsion_m=ICE_m+start_m+bat_m+EM_m+prop_m*prop_n;% Propulsion System for HEUAS(kg)
WF_propulsion_tot=propulsion_m*g/Wo; % Weight Fraction for Entire Propulsion System
% Create vector for mission weight fractions:
WF_mission = [WF_TO; WF_climb; WF_cruise; WF_endure; WF_landing];
% Create vector for propulsion system component weight fractions:
WF_propulsion = [WF_fuel; ICE_m/des_uas_m; WF_bat; WF_EM;...
    (prop_m*prop_n+start_m)*g/Wo];
% Create vector for aircraft component weight fractions:
WF_component = [uas_glider_m/des_uas_m; propulsion_m/des_uas_m;...
    uas_empty_m/des_uas_m; fuel_m/des_uas_m; pay_m/des_uas_m];

% Check Performance Requirements
% Check the ROC Requirement Requirement
% Max ROC (m/s), Anderson-P&D, Eqs 5.117 and 5.118
ROCmax=(ICE_P_W*prop_eff(1,1)-uas_PR_Vendure_act)/uas_W;
if (ROCmax>perf_ROC)
    disp(['HEUAS ICE Alone Exceeds ROC Requirement by (ft/min): ',...
        num2str(196.9*(ROCmax-perf_ROC))]);
else
    disp(['HEUAS ICE Alone Does Not Meet ROC Requirement by (ft/min): ',...
        num2str(196.9*(perf_ROC-ROCmax))]);
end

```

```

end

% Check Max Speed Requirement
disp(' ')
if (ICE_P_W+EM_overtrq*EM_P_W_act)>(uas_PS_Vmax)
    % Over-Torque EM for short periods of time (approx 30 seconds)
    disp(['HE Propulsion System Meets Vmax Requirement by (W): ',...
        num2str((ICE_P_W+EM_overtrq*EM_P_W_act)-(uas_PS_Vmax))]);
else
    disp(['HE Propulsion System Does not Meet Vmax Requirement by (W): ',...
        num2str((uas_PS_Vmax)-(ICE_P_W+EM_overtrq*EM_P_W))]);
end
%disp(['Actual Max Velocity for HEUAS (kts): ']);
disp(' ');

% Display Data
disp(' ');
disp('Aerodynamic Parameters:');
disp([' UAS Oswald Efficiency Factor: ', num2str(uas_e)]);
disp([' UAS Zero-Lift Drag Coefficient (Cdo): ', num2str(uas_Cdo)]);
disp([' Max Lift Coefficient (Clmax): ', num2str(uas_Clmax)]);
disp(' ');
disp('Performance Parameters:');
disp([' Endurance Time (hr): ', num2str(perf_tendure/3600)]);
disp([' Rate-of-Climb (ft/min): ', num2str(perf_ROC*60*3.28)]);
disp([' Cruise Velocity (kts): ', num2str(msec2kts*perf_Vcruise)]);
disp([' Endurance Velocity-Theoretical (kts): ', num2str(msec2kts*Vendure)]);
disp([' Endurance Velocity-Actual (kts): ', num2str(msec2kts*Vendure_act)]);
disp([' Endurance Parameter-Actual (Cl^1.5/Cd): ', num2str(uas_Cl_15_Cd)]);
disp([' Stall Velocity-Actual (kts): ', num2str(msec2kts*Vstall)]);
disp([' Max Velocity (kts): ', num2str(msec2kts*perf_Vmax)]);
disp([' Payload + Avionics Power (W): ', num2str(des_pay_P+des_fcs_P)]);
disp(' ');
disp('Aerodynamic Power Requirements: ');
disp([' Power Required for Climb (W): ', num2str(uas_PRmin_climb)]);
disp([' Power Required for Cruise (W): ', num2str(uas_PR_Vcruise)]);
disp([' Power Required for Theoretical Endurance (W): ', num2str(uas_PR_Vendure)]);
disp([' Power Required for Stall (W): ', num2str(uas_PR_Vstall)]);
disp([' Power Required for Actual Endurance (W): ', num2str(uas_PR_Vendure_act)]);
disp([' Power Required for Max Velocity (W): ', num2str(uas_PR_Vmax)]);
disp(' ');
disp('UAS Design Results:');
disp([' UAS Total Mass-Desired (kg): ', num2str(des_uas_m)]);
disp([' UAS Total Mass-Actual (kg): ', num2str(Wo/g)]);
disp([' Payload Mass-Desired (kg): ', num2str(des_pay_m)]);
disp([' Payload Mass-Actual for Original (kg): ', num2str(pay_m_org)]);
disp([' Payload Mass-Actual for HEUAS (kg): ', num2str(pay_m)]);
disp([' Original UAS Empty Mass (kg): ', num2str(uas_empty_m_org)]);
disp([' HEUAS Empty Mass (kg): ', num2str(uas_empty_m)]);
disp([' Wing Area-Desired (m^2): ', num2str(des_uas_S)]);
disp([' Wing Area-Actual (m^2): ', num2str(uas_S)]);
disp([' Aspect Ratio-Desired: ', num2str(des_uas_AR)]);
disp([' Aspect Ratio-Actual: ', num2str(uas_AR)]);
disp([' Wing Span (m): ', num2str(uas_wing_span)]);
disp([' Wing Chord (m): ', num2str(uas_wing_chord)]);
disp(' ');
disp('Weight Fractions for Original Configuration:');
disp([' WF for Warm Up/Takeoff: ', num2str(WF_TO_org)]);
disp([' WF for Climb: ', num2str(WF_climb_org)]);
disp([' WF for Cruise: ', num2str(WF_cruise_org)]);
disp([' WF for Endure: ', num2str(WF_endure_org)]);
disp([' WF for Landing: ', num2str(WF_landing_org)]);
disp([' WF-Empty: ', num2str(WF_empty)]);
disp([' WF-Fuel: ', num2str(WF_fuel_org)]);
disp([' WF-Payload: ', num2str(WF_pay_org)]);
disp([' WF-Propulsion (ICE, Gen, Prop): ', num2str(WF_propulsion_tot_org)]);
disp(' ');
disp('Propulsion Requirements for Original UAS');
disp([' ICE Size (W): ', num2str(ICE_P_W_org)]);
disp([' ICE Size (hp): ', num2str(ICE_P_hp_org)]);

```

```

disp([' ICE Size (in^3): ', num2str(ICE_Size_in3_org)]);
disp(' ');
disp('Weight Fractions for HEUAS:');
disp([' WF for Warm Up/Takeoff: ', num2str(WF_TO)]);
disp([' WF for Climb: ', num2str(WF_climb)]);
disp([' WF for Cruise: ', num2str(WF_cruise)]);
disp([' WF for Endure: ', num2str(WF_endure)]);
disp([' WF for Landing: ', num2str(WF_landing)]);
disp([' WF-Empty: ', num2str(uas_empty_m/des_uas_m)]);
disp([' WF-Fuel: ', num2str(WF_fuel)]);
disp([' WF-Payload: ', num2str(WF_pay)]);
disp([' WF-Propulsion (ICE, Starter, Batteries, EM, Prop): ',...
num2str(WF_propulsion_tot)]);
disp(' ');
disp('Propulsion Requirements for HEUAS:');
disp([' ICE Size (W): ', num2str(ICE_P_W)]);
disp([' ICE Size (hp): ', num2str(ICE_P_hp)]);
disp([' ICE Size (in^3): ', num2str(ICE_Size_in3)]);
disp([' ICE Cruise SFC (lb/hp/hr): ', num2str(SFC_cruise/1.6576E-6)]);
disp([' Fuel Mass Required (kg): ', num2str(fuel_m)]);
disp([' EM Size (W): ', num2str(EM_P_W_act)]);
disp([' EM Size (kg): ', num2str(EM_m)]);
disp([' EM Efficiency (%): ', num2str(100*EM_eff)]);
disp([' EM Over-Torque Factor: ', num2str(EM_overtrq)]);
disp([' Battery Mass (kg): ', num2str(bat_m)]);
disp([' Battery Storage (Wh): ', num2str(bat_Wh)]);
disp(' ');
if (chargetype==3)
disp('Recharging Requirements:');
disp([' Electric Power Available to Recharge Batteries (W): ',...
num2str(charge_PA)]);
disp([' Endurance Time on Initial Charge (min): ',...
num2str(perf_tendure_segment_1/60)]);
disp([' Endurance Time after Recharge (min): ',...
num2str(perf_tendure_segment_n/60)]);
disp([' Time to Recharge Batteries (min): ',num2str(charge_t/60)]);
disp([' # Recharging Cycles: ',num2str(n_recharge)]);
disp([' New Mission Length (hrs): ',...
num2str((perf_tendure_segment_1+perf_tendure_segment_n*n_recharge+...
perf_tcruise*2+charge_t*n_recharge)/3600)]);

disp([' Total Fuel Required to Recharge Batteries (kg): ',...
num2str(charge_fuel/g)]);
disp([' Fuel Increase to Recharge Batteries (%): ',...
num2str(fuel_m/(fuel_m-charge_fuel/g)*100-100)]);

disp([' Battery Mass Reduction (kg): ', num2str(bat_reduction_m)]);
disp([' Battery Mass Reduction (%): ', ...
num2str(bat_reduction_m/(bat_reduction_m+bat_m)*100)]);
disp(' ');
end

if (prop_n==2)
disp(['Cruise Power Required to Overcome Propeller Windmilling (W): ',...
num2str(prop_drag_P_W)]);
disp(' ');
end

%% Create tab-delimited output file for results
% FID=fopen('heuasresults', 'a');
% fprintf(FID,'%s \t %g \t %g...
% \t %g \t %g...
% \t %g \t %g...
% \t %g \t %g \t %g \t %g \n',...
% hybridtype, chargetype, h, h_AGL, bat_ED, uas_Cdo, uas_e, EM_eff, EM_eff_gen,...
% des_uas_m, des_pay_m, des_pay_P, des_fcs_P, perf_tendure, perf_tcruise,...
% perf_ROC, perf_Vcruise, perf_Vmax, uas_WL, uas_AR, uas_Clmax, Vstall,...
% Vendure, Vendure_act, uas_PRmin_climb, uas_PR_Vcruise, uas_PR_Vendure,...
% uas_PR_Vendure_act, uas_PR_Vmax, pay_m, uas_empty_m, uas_S, uas_wing_span,...
% uas_wing_chord, ICE_P_W, fuel_m, EM_P_W_act, bat_m, bat_Wh);

```

```

% fclose('all');

end

% Function plots weight fraction results
function []=WFplot(WF_component_org, WF_mission_org, WF_propulsion_org, WF_component,
WF_mission, WF_propulsion)

figure; colormap('bone');
bar1=bar([WF_component_org(1) WF_component(1); WF_component_org(2) WF_component(2);...
        WF_component_org(3) WF_component(3); WF_component_org(4) WF_component(4);...
        WF_component_org(5) WF_component(5)], 'group');
set(gca, 'YGrid', 'on', 'XTickLabel', {'Glider'; 'Propulsion'; 'Empty'; 'Fuel'; 'Payload'},...
      'fontsize',10);
xlabel('Aircraft Component', 'fontsize',10); ylabel('Weight Fraction', 'fontsize',10);
set(bar1(1), 'FaceColor', [0.1098 0.1804 0.3098]);
set(bar1(2), 'FaceColor', [0.8706 0.9294 1]);
legend1=legend('Original', 'Hybrid');
set(legend1, 'fontsize',8);
%title('Weight Fractions, Normalized to UAS Weight');

figure; colormap('bone');
bar2=bar([1-WF_mission_org(1) 1-WF_mission(1); 1-WF_mission_org(2) 1-WF_mission(2);...
        1-WF_mission_org(3)^2 1-WF_mission(3)^2; 1-WF_mission_org(4) 1-WF_mission(4);...
        1-WF_mission_org(5) 1-WF_mission(5)], 'group');
set(gca, 'YGrid', 'on', 'XTickLabel', {'Warm-
up/TO'; 'Climb'; 'Cruise'; 'Endurance'; 'Landing'},...
      'fontsize',10);
xlabel('Mission Segment', 'fontsize',10); ylabel('Weight Fraction', 'fontsize',10);
set(bar2(1), 'FaceColor', [0.1098 0.1804 0.3098]);
set(bar2(2), 'FaceColor', [0.8706 0.9294 1]);
legend2=legend('Original', 'Hybrid');
set(legend2, 'fontsize',8);
%title('Fuel Weight Fractions');

figure; colormap('bone');
bar3=bar([WF_propulsion_org(1) WF_propulsion(1); WF_propulsion_org(2)
WF_propulsion(2);...
        WF_propulsion_org(3) WF_propulsion(3); WF_propulsion_org(4) WF_propulsion(4);...
        WF_propulsion_org(5) WF_propulsion(5)], 'group');
set(gca, 'YGrid', 'on', 'XTickLabel', {'Fuel'; 'ICE'; 'Batteries'; 'EM'; 'Other'}, 'fontsize',10);
xlabel('Propulsion Component', 'fontsize',10); ylabel('Weight Fraction', 'fontsize',10);
set(bar3(1), 'FaceColor', [0.1098 0.1804 0.3098]);
set(bar3(2), 'FaceColor', [0.8706 0.9294 1]);
legend3=legend('Original', 'Hybrid');
set(legend3, 'fontsize',8);
%title('Propulsion System Weight Fraction Comparison');

end

% Function plots comparison results
function []=Comparisonplot(WF_component, WF_mission, WF_propulsion, x, EM_P_W)

global bat_ED des_uas_m

figure; colormap('bone');
bar1=bar([WF_component(1,1) WF_component(1,2) WF_component(1,3);...
        WF_component(2,1) WF_component(2,2) WF_component(2,3);...
        WF_component(3,1) WF_component(3,2) WF_component(3,3);...
        WF_component(4,1) WF_component(4,2) WF_component(4,3);...
        WF_component(5,1) WF_component(5,2) WF_component(5,3)], 'group');
set(gca, 'YGrid', 'on', 'XTickLabel', {'Glider'; 'Propulsion'; 'Empty'; 'Fuel'; 'Payload'},...
      'fontsize',10);
xlabel('Aircraft Component', 'fontsize',10); ylabel('Weight Fraction', 'fontsize',10);
set(bar1(1), 'FaceColor', [0.1098 0.1804 0.3098]);
set(bar1(2), 'FaceColor', [0.3569 0.5961 0.9647]);
set(bar1(3), 'FaceColor', [0.8706 0.9294 1]);
legend1 = legend('Clutch-Start', 'Electric-Start', 'Centerline-Thrust');

```

```

set(legend1,'fontsize',8);
%title(['Weight Fractions, Normalized to UAS Weight (' ,num2str(des_uas_m),' kg)']);

figure; colormap('bone');
bar2=bar([WF_propulsion(1,1) WF_propulsion(1,2) WF_propulsion(1,3);...
         WF_propulsion(2,1) WF_propulsion(2,2) WF_propulsion(2,3);...
         WF_propulsion(3,1) WF_propulsion(3,2) WF_propulsion(3,3);...
         WF_propulsion(4,1) WF_propulsion(4,2) WF_propulsion(4,3);...
         WF_propulsion(5,1) WF_propulsion(5,2) WF_propulsion(5,3)], 'group');
set(gca, 'YGrid', 'on', 'XTickLabel', {'Fuel'; 'ICE'; 'Batteries'; 'EM'; 'Other'}, 'fontsize', 10);
xlabel('Propulsion Component', 'fontsize', 10); ylabel('Weight Fraction', 'fontsize', 10);
set(bar2(1), 'FaceColor', [0.1098 0.1804 0.3098]);
set(bar2(2), 'FaceColor', [0.3569 0.5961 0.9647]);
set(bar2(3), 'FaceColor', [0.8706 0.9294 1]);
set(legend, 'fontsize', 8);
legend2 = legend('Clutch-Start', 'Electric-Start', 'Centerline-Thrust');
set(legend2, 'fontsize', 8);
%title(['Propulsion System Weight Fraction Comparison for ' ,num2str(des_uas_m),...
% ' kg UAS']);

disp(' ');
disp('Hybrid Component Comparison:');
disp(' ');
disp('Hybrid Type          ICE(W)    Fuel(kg)    EM(W)    Battery(Wh)    Payload(kg)');
disp('-----');
disp(['Clutch-Start      ', num2str(x(6,1)), ' ', num2str(WF_propulsion(1,1))*...
des_uas_m, ' ', num2str(EM_P_W(1)), ' ', num2str(WF_propulsion(3,1))*...
des_uas_m*bat_ED), ' ', num2str(WF_component(5,1)*des_uas_m)];

disp(['Electric-Start    ', num2str(x(6,2)), ' ', num2str(WF_propulsion(1,2))*...
des_uas_m, ' ', num2str(EM_P_W(2)), ' ', num2str(WF_propulsion(3,2))*...
des_uas_m*bat_ED), ' ', num2str(WF_component(5,2)*des_uas_m)];

disp(['Centerline-Thrust ', num2str(x(6,3)), ' ', num2str(WF_propulsion(1,3))*...
des_uas_m, ' ', num2str(EM_P_W(3)), ' ', num2str(WF_propulsion(3,3))*...
des_uas_m*bat_ED), ' ', num2str(WF_component(5,3)*des_uas_m)];

end

```

## Bibliography

- <sup>1</sup>Newcome, L. R., *Unmanned Aviation: A Brief History of Unmanned Aerial Vehicles*, AIAA, Reston, VA, 2004.
- <sup>2</sup>Zaloga, S., *Unmanned Aerial Vehicles: Robotic Air Warfare 1917-2007*, Osprey Publishing Ltd., Westminster, MD, 2008.
- <sup>3</sup>Kaplan, F. "Attack of the Drones," *Newsweek*, 28 September 2009.
- <sup>4</sup>"Predator Passes 600,000 Flight Hours," *Air Force News Service*, 30 September 2009. URL: <http://www.af.mil/news/story.asp?id=123170356> [cited 7 October 2009]
- <sup>5</sup>Office of the Secretary of Defense, "Unmanned Systems Roadmap (2007-2032)," 10 December 2007.
- <sup>6</sup>Headquarters United States Air Force, "USAF Unmanned Aircraft Systems Flight Plan (2009-2047)," 18 May 2009.
- <sup>7</sup>Scarborough, R., "Taliban Makes IEDs Deadlier," *Washington Times*, 15 September 2009, p. 1.
- <sup>8</sup>Joint Improvised Explosive Device Defeat Organization. URL: <https://www.jieddo.dod.mil/about.aspx> [cited 24 August 2009]
- <sup>9</sup>Lefkow, C. "US General Pushes for Unmanned Vehicles", Google News (AFP), 12 August 2009.
- <sup>10</sup>Office of the Secretary of Defense, "Unmanned Aircraft Systems Roadmap (2005-2030)," 4 August 2005.
- <sup>11</sup>Warwick, G., "Hybrid-Electric UAVs Under Development," *Aviation Week & Space Technology*, 20 July 2009, p 38.
- <sup>12</sup>Van den Bossche, P. "Structure of a series hybrid-electric vehicle with peak power unit," *Wikipedia*, URL: <http://en.wikipedia.org/wiki/File:Hybridpeak.png> [cited 24 September 2009]
- <sup>13</sup>Miller, J. M., *Propulsion Systems for Hybrid Vehicles*, IEE Power & Energy Series, IEE, London, UK, 2004, Chaps. 1, 2.
- <sup>14</sup>Van den Bossche, P. "Structure of a parallel hybrid vehicle," *Wikipedia*, URL: <http://en.wikipedia.org/wiki/File:Hybridpar.png> [cited 24 September 2009]
- <sup>15</sup>Van den Bossche, P. "Structure of a combined hybrid vehicle," *Wikipedia*, URL: <http://en.wikipedia.org/wiki/File:Hybridcombined.png> [cited 25 September 2009]

- <sup>16</sup>Honda, Inc., “Insight Heritage,” URL: <http://automobiles.honda.com/insight-hybrid/heritage.aspx> [cited 23 September 2009]
- <sup>17</sup>Garrett, J. “Toyota and Ford Reach Hybrid Milestones,” *New York Times*, 11 March 2009.
- <sup>18</sup>Paur, J., “Hybrid Power Comes to Aviation,” *Wired.com*, 28 July 2009, URL: <http://www.wired.com/autopia/2009/07/hybrid-aviation/> [cited 2 October 2009]
- <sup>19</sup>Warwick, G., “Aurora Working on New Hybrid Engine for UAVs,” *Aerospace Daily & Defense Report*, 10 April 2009, p 4.
- <sup>20</sup>Wall, R., “New Engine Concepts Emerge for UAVs and UCAVs,” *Aviation Week & Space Technology*, 3 March 2008, p 24.
- <sup>21</sup>Gitlin, S. and Boyer, M., “AeroVironment Puma Small UAS Achieves Record Flight of Over Nine Hours Using Fuel Cell Battery Hybrid System,” *AeroVironment*, Monrovia, CA, 6 March 2008.
- <sup>22</sup>Mecham, Michael. “Boeing Fuel Cell Points to UAVS,” *AviationWeek.com*, 3 April 2008, URL: <http://www.aviationweek.com/aw/generic/story.jsp?id=news/CELL04038.xml&headline=Boeing%20Fuel%20Cell%20Flights%20Point%20To%20UAVs&channel=defense#> [cited 17 September 2009]
- <sup>23</sup>Toensmier, P., “The Cutting Edge: Fuel Cell Powers Manned Flight,” *Defense Technology International*, Vol. 3, No. 8, September 2009.
- <sup>24</sup>National Aeronautics and Space Administration, “Helios Prototype: The forerunner of 21<sup>st</sup> century solar-powered ‘atmospheric satellites,’” URL: <http://www.nasa.gov/centers/dryden/news/FactSheets/FS-068-DFRC.html> [cited 6 October 2009]
- <sup>25</sup>Bradley, T. H., Moffitt, B. A., Parekh, D. E., Fuller, T. F., and Mavris, D. N., “Energy Management for Fuel Cell Powered Hybrid-Electric Aircraft,” presented at *AIAA 7<sup>th</sup> International Energy Conversion Engineering Conference*, AIAA Paper 2009-4950, Denver, CO, August 2009.
- <sup>26</sup>Becker, T. J., “Flying on Hydrogen: Georgia Tech Researchers Use Fuel Cells to Power Unmanned Aerial Vehicle,” *Georgia Tech Research News*, Atlanta, GA, 28 August 2006.
- <sup>27</sup>Anderson, M., “At a Glance: Ion Tiger,” Office of Naval Research Program Code 332, March 2009.
- <sup>28</sup>Harmon, F. G., Frank, A. A., and Chattot J. J., “Conceptual Design and Simulation of a Small Hybrid-Electric Unmanned Aerial Vehicle,” *Journal of Aircraft*, Vol. 43, No. 5, Sept-Oct 2006, pp 1490-1498.

- <sup>29</sup>Hrad, P. M., “Conceptual Design Tool for Fuel-Cell Powered Micro Air Vehicles,” Master’s Thesis, Dept. of Aeronautics and Astronautics, Air Force Institute of Technology, Wright-Patterson AFB, OH, March 2010.
- <sup>30</sup>Harmats, M. and Weihs, D., “Hybrid-Propulsion High Altitude Long-Endurance Remotely Piloted Vehicle,” *Journal of Aircraft*, Vol. 36, No. 2, 1999, pp 321-331.
- <sup>31</sup>Heywood, J. B., *Internal Combustion Engine Fundamentals*, McGraw-Hill, New York, NY, 1988, Chaps. 1, 2, 15.
- <sup>32</sup>Turns, S. R., *An Introduction to Combustions: Concepts and Applications*, 2<sup>nd</sup> ed., McGraw-Hill, Boston, MA, 2000, Chap. 2.
- <sup>33</sup>Anderson, J. D., Jr., *Aircraft Performance and Design*, McGraw-Hill, Boston, MA, 1999, Chaps. 2, 3, 5.
- <sup>34</sup>USD(AT&L). *DoD Management Policy for Energy Commodities and Related Services (DOD4140.25)*. U.S. Department of Defense, April 2004.
- <sup>35</sup>Drela, M., “*QPROP* Documents: First-Order DC Electric Motor Model,” *QPROP*, Version 1.21, Massachusetts Institute of Technology, February 2007.
- <sup>36</sup>Drela, M., “*QPROP* Documents: DC Motor/Propeller Matching,” *QPROP*, Version 1.21, Massachusetts Institute of Technology, 3 March 2005.
- <sup>37</sup>Stux, A. M. and Swider-Lyons, K., “Survey of Commercial Small Lithium Polymer Batteries,” *Naval Research Laboratory*, NRL/MR/6110--07-0973, Washington, DC, 19 September 2007.
- <sup>38</sup>Buchmann, I., “What’s the best battery?” *BatteryUniversity.com*, November 2006. URL: <http://www.batteryuniversity.com/partone-3.htm> [cited 15 October 2008]
- <sup>39</sup>Mikhaylik, Y., “Fundamental Chemistry of Sion Power Li/S Battery,” presented at *IBA-HBC 2006*, Waikoloa, HI, 9-12 January 2006.
- <sup>40</sup>Gur, O. and Rosen, A., “Comparison Between Blade-Element Models of Propellers,” *Technion Israel Institute of Technology*, Haifa 32000, Israel.
- <sup>41</sup>Department of the Air Force, Department of the Navy, and Department of Commerce, *ANC-9 Bulletin: Aircraft Propeller Handbook*, 1<sup>st</sup> ed., U.S. Government Printing Office, September 1956.
- <sup>42</sup>Ol, M., Zeune, C., and Logan, M., “Analytical-Experimental Comparison for Small Electric Unmanned Air Vehicle Propellers,” presented at *26<sup>th</sup> AIAA Applied Aerodynamics Conference*, AIAA Paper 2008-7345, Honolulu, HI, 18-21 August 2008.

<sup>43</sup>Drela, M., “QPROP User Guide,” *QPROP*, Version 1.21, Massachusetts Institute of Technology, 6 July 2007.

<sup>44</sup>Harmon, F. G., “Neural Network control of a Parallel Hybrid-Electric Propulsion System for a Small Unmanned Aerial Vehicle,” Ph.D. Dissertation, Dept. of Mechanical and Aeronautical Engineering, University of California-Davis, Davis, CA, 2005.

<sup>45</sup>Hiserote, R. M., Hrad, P. M., Sabat, J. W., and Wilson, C. W., “AERO 685: Aircraft Design Final Report,” Dept. of Aeronautics and Astronautics, Air Force Institute of Technology, Wright-Patterson AFB, OH, 2009.

<sup>46</sup>Raymer, D. P., *Aircraft Design: A Conceptual Approach*, 4<sup>th</sup> ed., AIAA Education Series, Reston, VA, 2006. Chaps. 3, 6, 17.

<sup>47</sup>Arora, J. S. *Introduction to Optimum Design*, 2<sup>nd</sup> ed., Elsevier Academic Press, New York, NY, 2004, Chaps. 4, 11.

<sup>48</sup>Mattingly, J. D., Heiser, W. H. and Pratt, D. T., *Aircraft Engine Design*, 2<sup>nd</sup> ed., AIAA Education Series, Reston, VA, 2002. Chap. 3.

<sup>49</sup>World Aeronautical Database, URL: <http://worldaerodata.com/> [cited 18 January 2010]

<sup>50</sup>Lim, H. L., “Network Payload Integration for the Scan-Eagle UAV,” Master’s Thesis, Dept. of Mechanical and Aeronautical Engineering, Naval Postgraduate School, Monterey, CA, December 2007.

<sup>51</sup>Procerus Technologies, *Kestrel Autopilot*. URL: <http://www.procerusuav.com/productsKestrelAutopilot.php> [cited 25 January 2010]

<sup>52</sup>Wilson, C. W., King, P. I., Hoke, J. L., and Schauer, F. R., “The Effects of Varied Octane Rating on a Small Spark Ignition Internal Combustion Engine,” presented at 48<sup>th</sup> AIAA Aerospace Sciences Meeting, AIAA paper 2010-482, Orlando, FL, 4-7 January 2010.

<sup>53</sup>Hobby Lobby International, Inc., “On-Board Starter for 90-120 RC Engine,” URL: <http://www.hobby-lobby.com/fema.htm> [cited 26 January 2010]

<sup>54</sup>Sion Power, “Unmanned Systems,” URL: <http://www.sionpower.com/unmanned.html> [cited 26 January 2010]

<sup>55</sup>Insitu, Inc. URL: <http://www.insitu.com/scaneagle> [cited 4 June 09]

<sup>56</sup>Aerosonde, Inc. URL: <http://www.aerosonde.com/products/gallery.html> [cited 25 Aug 09]

<sup>57</sup>Manson, K., *Jane's Unmanned Aerial Vehicles and Targets*, Issue 29-2007, pp 242-245.

<sup>58</sup>Advanced Ceramics Research, Inc. URL: <http://www.acrtucson.com/UAV/silverfox/index.htm> [cited 25 Jul 09]

<sup>59</sup>AeroVironment, Inc. URL: <http://www.avinc.com/uas/adc/pointer/> [cited 25 Jul 09]

<sup>60</sup>3W Modellmotoren GmbH, Rödermark, Germany, URL: <http://www.3w-modellmotoren.com/katalog/motoren-3.html> [cited 12 January 2010]

<sup>61</sup>Cosworth, Torrance, CA, URL: <http://www.cosworth.com/Default.aspx?id=1095228> [cited 12 January 2010]

<sup>62</sup>Enya Metal Products Co., Miyoshi-Machi, Saitama Prefecture, Japan, URL: [http://www.enya-engine.com/catalogueE\\_top.html](http://www.enya-engine.com/catalogueE_top.html) [cited 13 January 2010]

<sup>63</sup>Hobbico, Inc., *Fuji-Imvac*, Champaign, IL, URL: <http://www.fuji-imvac.com/> [cited 12 January 2010]

<sup>64</sup>Hobbico, Inc., *OS Engines*, Champaign, IL, URL: <http://osengines.com/engines/airplane.html> [cited 12 January 2010]

<sup>65</sup>Hobbico, Inc., *Super Tigre*, Champaign, IL, URL: <http://www.supertigre.com/engines/index.html> [cited 12 January 2010]

<sup>66</sup>Model Motors, Ltd., *AXI Gold Line*, Pardubice, Czech Republic, URL: <http://www.modelmotors.cz/> [cited 12 January 2010]

<sup>67</sup>A2Tech, *FlyWARE*, Peschiera, Italy, URL: <http://www.flyware.it/eng/FlyWare-Products001.html> [cited 13 January 2010]

<sup>68</sup>Hacker Motor GmbH, Ergolding, Germany, URL: <http://www.hacker-motor.com/> [cited 12 January 2010]

<sup>69</sup>Castle Creations, Inc., *NEU Motors*, Olathe, KS, URL: <http://neumotors.com/Site/Motors.html> [cited 12 January 2010]

<sup>70</sup>Amit Industries Ltd., “Unmanned Systems Battery Packs, Smart Chargers”, Conference Brochure, Ashdod, Israel.

<sup>71</sup>BME Engines, *BME .90ci*, South Hutchinson, KS, URL: <http://www.bmeengine.com/engines.htm> [cited 7 February 2010]

<sup>72</sup>RM Hoffman Company, Sunnyvale, CA, URL: <http://www.rmhoffman.com/contact.html> [cited 8 February 2010]

<sup>73</sup>Davis, R. I. and Lorenz, R. D., “Engine torque ripple cancellation with an integrated starter alternator in a hybrid-electric vehicle: implementation and control,” *IEEE Transactions on Industry Applications*, Vol. 39, Issue 6, Nov. – Dec. 2003, pp. 1765-1774.

## **Vita**

Captain Ryan M. Hiserote graduated from Cherokee High School in Marlton, NJ in 2000. He completed his Bachelor of Science in Mechanical Engineering (B.S.E.) degree at Messiah College, Grantham, PA, in 2004. He received his United States Air Force commission on August 12, 2005 after completing Officer Training School at Maxwell AFB, AL.

His first Air Force assignment was at the Theater Battle Management Core Systems (TBMCS) Unit Level System Program Office (SPO) at Hanscom AFB, MA, where he served as the Chief of Fielding. Starting in July 2007, he served as the TBMCS International Programs Chief, where he managed foreign military sales cases with Australia, Canada and the United Kingdom, while also serving as the focal point for the program's interoperability efforts with NATO. In September 2008, he entered the Graduate School of Engineering and Management at the Air Force Institute of Technology. Upon completion of a Master's degree in Aeronautical Engineering in March 2010, he will be assigned to the Air Force Research Laboratory's Propulsion Directorate, Power Generation Branch at Wright-Patterson AFB, OH.

<b>REPORT DOCUMENTATION PAGE</b>			<i>Form Approved</i> <i>OMB No. 074-0188</i>	
<p>The public reporting burden for this collection of information is estimated to average 1 hour per response, including the time for reviewing instructions, searching existing data sources, gathering and maintaining the data needed, and completing and reviewing the collection of information. Send comments regarding this burden estimate or any other aspect of the collection of information, including suggestions for reducing this burden to Department of Defense, Washington Headquarters Services, Directorate for Information Operations and Reports (0704-0188), 1215 Jefferson Davis Highway, Suite 1204, Arlington, VA 22202-4302. Respondents should be aware that notwithstanding any other provision of law, no person shall be subject to a penalty for failing to comply with a collection of information if it does not display a currently valid OMB control number.</p> <p><b>PLEASE DO NOT RETURN YOUR FORM TO THE ABOVE ADDRESS.</b></p>				
<b>1. REPORT DATE (DD-MM-YYYY)</b> 25-03-2010		<b>2. REPORT TYPE</b> Master's Thesis		<b>3. DATES COVERED (From - To)</b> Sept 2008 - Mar 2010
<b>4. TITLE AND SUBTITLE</b> Analysis of Hybrid-Electric Propulsion System Designs for Small Unmanned Aircraft Systems			<b>5a. CONTRACT NUMBER</b>	
			<b>5b. GRANT NUMBER</b>	
			<b>5c. PROGRAM ELEMENT NUMBER</b>	
<b>6. AUTHOR(S)</b> Hiserote, Ryan M., Captain, USAF			<b>5d. PROJECT NUMBER</b> 09ENY259	
			<b>5e. TASK NUMBER</b>	
			<b>5f. WORK UNIT NUMBER</b>	
<b>7. PERFORMING ORGANIZATION NAMES(S) AND ADDRESS(S)</b> Air Force Institute of Technology Graduate School of Engineering and Management (AFIT/ENY) 2950 Hobson Way, Building 640 WPAFB, OH 45433-8865			<b>8. PERFORMING ORGANIZATION REPORT NUMBER</b>  AFIT/GAE/ENY/10-M11	
<b>9. SPONSORING/MONITORING AGENCY NAME(S) AND ADDRESS(ES)</b> Dr. Fred Schauer (frederick.schauer@wpafb.af.mil) Air Force Research Laboratory 1950 Fifth Street WPAFB, OH 45433-7251			<b>10. SPONSOR/MONITOR'S ACRONYM(S)</b> AFRL/RZTC	
			<b>11. SPONSOR/MONITOR'S REPORT NUMBER(S)</b>	
<b>12. DISTRIBUTION/AVAILABILITY STATEMENT</b>  APPROVED FOR PUBLIC RELEASE; DISTRIBUTION UNLIMITED				
<b>13. SUPPLEMENTARY NOTES</b>				
<b>14. ABSTRACT</b>  Currently fielded electric-powered small unmanned aircraft systems (UAS) lack the endurance desired by warfighters, while their internal combustion engine driven counterparts generate mission compromising acoustic and thermal signatures. Parallel hybrid-electric propulsion systems would meet the military's needs by combining the advantages of hydrocarbon and electric power systems. Three distinct parallel hybrid-electric system designs, each with three unique battery discharging profiles, were analyzed and compared using a constrained static optimization formulation based upon traditional aircraft design equations. Each system combined an internal combustion engine sized for cruise speed with an electric motor sized for endurance speed. The nine variations were compared using a typical intelligence, surveillance and reconnaissance (ISR) mission profile. The analysis determined the most suitable design for the baseline ISR mission and provided recommended missions for the remaining designs.				
<b>15. SUBJECT TERMS</b> Hybrid-electric, Propulsion, Unmanned, Optimization, Power				
<b>16. SECURITY CLASSIFICATION OF:</b>			<b>17. LIMITATION OF ABSTRACT</b>  UU	<b>18. NUMBER OF PAGES</b>  148
<b>a. REPORT</b>  U	<b>b. ABSTRACT</b>  U	<b>c. THIS PAGE</b>  U		
			<b>19a. NAME OF RESPONSIBLE PERSON</b> Frederick G. Harmon, Lt Col, USAF	
			<b>19b. TELEPHONE NUMBER (Include area code)</b> DSN 786-3636 x7478 (frederick.harmon@afit.edu)	